TESE DE DOUTORAMENTO

SIMULATION OF CLINICAL PET STUDIES FOR THE ASSESSMENT OF QUANTIFICATION METHODS

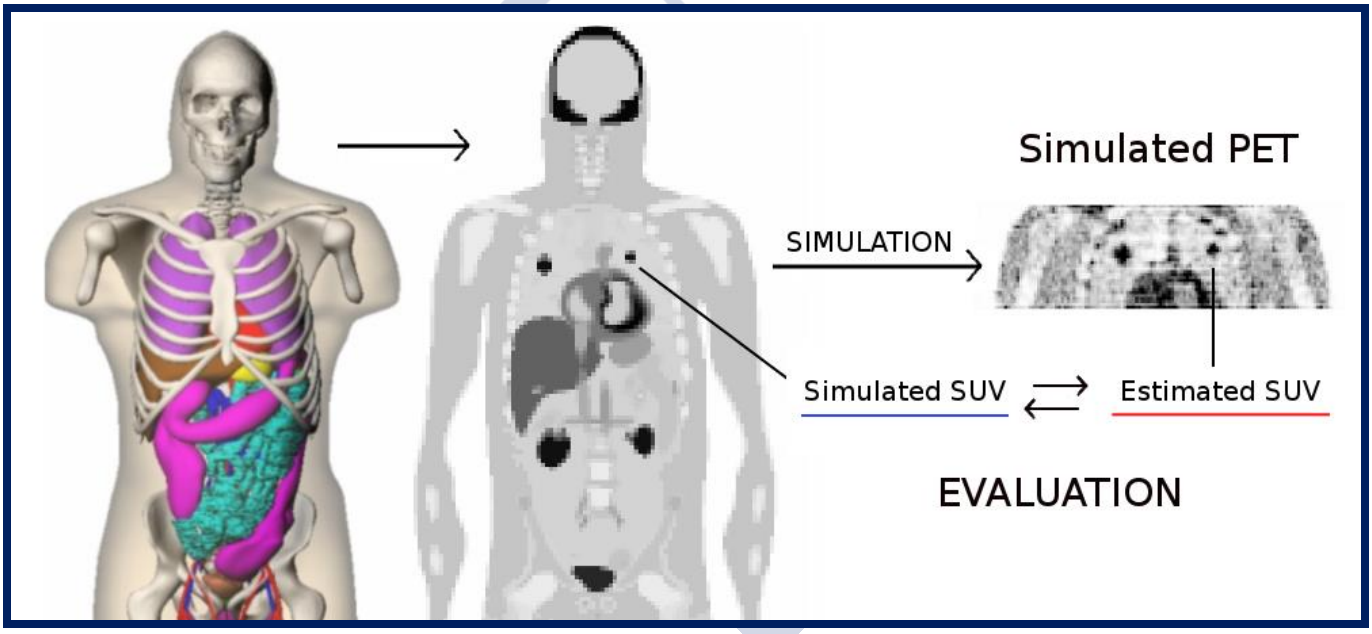

Jesús Silva Rodríguez

DEPARTAMENTO DE PSIQUIATRÍA, RADIOLOXÍA, SAÚDE PÚBLICA, ENFERMARÍA E MEDICINA

PROGRAMA DE DOUTORAMENTO EN INVESTIGACIÓN CLÍNICA EN MEDICINA

FACULTADE DE MEDICINA E ODONTOLOXÍA

SANTIAGO DE COMPOSTELA 2017

TESE DE DOUTORAMENTO

SIMULATION OF CLINICAL PET STUDIES FOR THE ASSESSMENT OF QUANTIFICATION METHODS

Asdo. .....

Jesús Silva Rodríguez

DEPARTAMENTO DE PSIQUIATRÍA, RADIOLOXÍA, SAÚDE PÚBLICA, ENFERMARÍA E MEDICINA

PROGRAMA DE DOUTORAMENTO EN INVESTIGACIÓN CLÍNICA EN MEDICINA

FACULTADE DE MEDICINA E ODONTOLOXÍA

SANTIAGO DE COMPOSTELA 2017

USC
UNIVERSIDADE
DE SANTIAGO
DE COMPOSTELA

USC UNIVERSIDADE DE SANTIAGO DE COMPOSTELA
DEPARTAMENTO DE PSIQUIATRÍA, RADIOLOGÍA Y SALUD PÚBLICA

Álvaro Ruibal Morell, catedrático do Departamento de Psiquiatría, Radioloxía e Saúde Pública da Universidade de Santiago de Compostela, e Pablo Aguiar Fernández, investigador Ramón y Cajal do Grupo de Imaxe Molecular e Física Médica, adscrito a dito departamento.

CERTIFICAN:

Que a presente memoria, titulada "Simulation of clinical PET studies for the assessment of quantification methods", presentada polo licenciado en Física Jesús Silva Rodríguez para optar ao grao de Doutor en Medicina, ten sido realizada baixo a nosa dirección no Departamento de Psiquiatría, Radioloxía e Saúde Pública da Universidade de Santiago de Compostela e, considerándoa rematada, autorizamos a súa presentación para que poida ser xulgada polo tribunal correspondente.

Ademáis, tratándose dunha tese por compendio de artigos, certificamos tamén que o doutorando é o autor principal de todos os traballos presentados e que a memoria presentada cumple todos os requisitos para ser presentada baixo esta modalidade, incluída a aprobación necesaria de todos os autores para incluir ditos traballos na presente memoria.

Fdo. Álvaro Ruibal Morell

Fdo. Pablo Aguiar Fernández

Fdo. Jesús Silva Rodríguez

Santiago de Compostela, 23 de marzo de 2017

USC
UNIVERSIDADE
DE SANTIAGO
DE COMPOSTELA

Abstract

Positron emission tomography (PET) is a non-invasive imaging technique that visualizes the distribution of different molecules within the body, providing functional and molecular information on different tissues. PET is routinely used for staging and treatment response evaluation in oncology, with ^{18}F-fluorodeoxyglucose (FDG) as the most common radiotracer of choice. Despite the fact that traditional evaluation is usually performed by visual inspection of the images, the current potential of PET relies on its capability to provide quantitative information, usually provided by a semi-quantitative parameter known as Standard Uptake Value (SUV) that is routinely measured in most centers (90%). This parameter provides relatively objective tumour characterization, reliable differential diagnosis and earlier evaluation and monitoring of treatment response. Nevertheless, SUV robustness has been questioned by the scientific community, since SUV can be affected by many different error sources, such as physiological changes between different studies from the same patient, patient management issues or technical issues related to acquisition, reconstruction and quantification protocols. Many authors have pointed to the need for further methodology standardization in order to minimize the impact of these effects, which lead to the publication of different PET acquisition and processing guidelines by both the European Association of Nuclear Medicine (EANM) and the Society of Nuclear Medicine and Molecular Imaging (SNMMI). These guidelines include recommendations for patient preparation, acquisition protocols, tomographic reconstruction, and quantification procedures. Regarding the physiological variations, high blood glucose level, patient motion and high uptake in brown fat due to patient stress have been related to lower SUV values, while increasing uptake period has been related to higher SUV values. Regarding acquisition and reconstruction protocols, image noise significantly bias SUV, and low spatial resolution or insufficient convergence can lead to lower SUV values, particularly for small lesions. Finally, regarding the quantification procedure, SUV outcome depends on the region of interest (ROI) volume and type and SUV normalization. Most of these studies are carried out by using anthropomorphic physical phantoms. These phantoms are ideal for investigating the impact of changing technical factors on the output images, enabling us for applications where patients cannot serve or should not serve. The limitations of the physical phantoms are reduced flexibility for changing shapes and volumes of the internal structures, high cost and cumbersome to use. An alternative is the use of digital phantoms, so that simulated PET studies are generated from the projection of phantoms by using analytical or Monte Carlo (MC) simulation techniques. The use of MC simulation methods instead of real acquisitions for evaluating these factors offers several advantages, such as a controlled framework were all the parameters are known a priori, with low cost and with no need of using ionizing radiation.

On this PhD thesis we developed a methodology for evaluating the robustness of SUV measurements based on MC simulations and the generation of novel databases of simulated studies based on digital anthropomorphic phantoms. This methodology has been applied to different problems related to quantification that were not previously addressed.

In a first study, we evaluated the extravasation of the injected dose as an uncertainty source for SUV quantification. Current guidelines for whole body PET state that studies with visible dose extravasations should be rejected for quantification protocols. Nevertheless, taking into account the ratio of extravasations, this solution is suboptimal, and a correction that allows the quantification of these patients would be useful. We evaluated 1367 patient studies, revealing that extravasation is a relatively frequent effect (18%), but only with a small fraction of patients (9.5%) presenting quantitatively remarkable extravasations ranging from 1% to a maximum of 22% of the injected dose. Two methods for estimating the extravasated dose were proposed and validated in different scenarios using MC simulations. A criterion based on the extravasated volume and maximum concentration was established in order to identify the patients that might be corrected. The proposed correction methodology compensated the impact of extravasations on SUV values with an error below 5%, allowing a precise quantification of these patients.

On a second work, we studied the impact of noise and low counting in the accuracy and repeatability of three commonly used SUV metrics (SUV_{max}, SUV_{mean} and SUV_{50}). This study is useful for dose optimization, especially in follow-up studies. Our results showed that tumour activity was overestimated using SUV_{max} for low doses and clearly underestimated using SUV_{mean}. Instead, the quantification of SUV_{50} showed great agreement with the simulated tumour activities and only slight underestimation was found for very small lesions. On the other hand, SUV_{mean} showed better performance than SUV_{50} in terms of repeatability, providing variability below 5% for all tumour sizes and for injected doses as low as 111 MBq.

The same model was used to study the effect of physiological muscular uptake variations on the quantification of FDG-PET studies. Previous works reported that undesirably increased physiologic muscular uptake is frequently encountered on FDG-PET scans (12.5%). This increased muscular uptake can create problems in visually differentiating between normal and pathologic FDG uptake and it has been described as a potential cause of false positives on image visual analysis. However, the effect of this increased values on image quantification remained to be studied. We simulated FDG-PET acquisitions from anthropomorphic phantoms that included different muscular uptake levels and three spherical lung lesions with diameters of 31, 21 and 9 mm for assessing this variability. A distribution of muscular uptake levels was obtained from 136 patients remitted to our centre for whole-body FDG-PET. Different SUV metrics were calculated for different noise realizations, lung lesions and muscular uptake values. Our analysis showed that muscular uptake variations are one of the dominant error sources for FDG-PET for doses in the clinical range.

Finally, our MC models were applied to simulate ^{18}F-fluorocholine (FCH) studies. The aim was to study the effect of spill-in counts from neighbouring regions on the quantification of small regions close to high activity extended sources. This effect can be a drawback for ^{18}F-based radiotracers when quantifying SUV near high-activity regions like the bladder. In this work, MC simulations of anthropomorphic phantoms with FCH biodistributions, variable bladder uptake and inserted prostatic tumours were used in order to obtain simulated realistic FCH data. We evaluated possible variations of the SUV with bladder uptake and we proposed a novel correction by appropriately adapting image reconstruction methodology. We showed that while the SUVs measured under these conditions are not reliable, images corrected using the proposed methodology provide better repeatability of SUVs, with biases around 5%. Results also showed remarkable improvements on visual detectability.

Resumo

A tomografía por emisión de positróns (TEP) é unha técnica de imaxe non invasiva que permite visualizar a biodistribución de diferentes moléculas no corpo humano, proporcionando información funcional sobre os distintos tecidos. A TEP utilízase rutineiramente para a diagnose, a estadiaxe e avaliación da resposta ao tratamento en oncoloxía, sendo a ^{18}F-fluorodeoxyglucosa (FDG) o radiofármaco máis utilizado hoxe en día. Aínda que a avaliación se realiza tradicionalmente a través da inspección visual das imaxes, o verdadeiro potencial da TEP está na posibilidade de ofrecer valores cuantitativos, que son normalmente obtidos mediante o cálculo do valor de absorción estándar (SUV), un parámetro semi-cuantitativo que se mide rutineiramente no 90% dos centros de todo o mundo. Este parámetro dános unha caracterización obxectiva do tumor, criterios de malignidade/benignidade e valores cuantizables para a monitorización e avaliación da terapia. Con todo, a robustez dos valores de SUV ten sido cuestionada en numerosas ocasións pola comunidade científica, xa que estes valores poden estar afectados por diversas fontes de incerteza debidos a cambios fisiolóxicos entre diferentes estudos do mesmo doente, cambios no manexo do doente ou cuestións técnicas relacionadas cos protocolos de adquisición, reconstrución e cuantización. Moitos autores apuntaron á necesidade de estandarización dos protocolos de cara a minimizar esta variabilidade, o que se reflectiu na publicación de distintas guías por parte da Sociedade Europea de Mediciña Nuclear (EANM) e da American Mediciña nuclear e Imaxe Molecular (SNMMI). Estas directrices inclúen recomendacións para a preparación do paciente e para os protocolos de adquisición, reconstrución e cuantización. En canto aos factores fisiolóxicos, está demostrado que altos niveis de glicosa, movementos involuntarios durante o estudo ou a activación de graxa parda debido ao estrés ou ao están relacionados con valores inferiores do SUV, mentres que os tempos de captación prolongados poderían causar un aumento nestes valores. En canto aos protocolos de adquisición e reconstrución, demostrouse que niveis elevados de ruído poden causar variacións nos valores de SUV, e que os límites de resolución espacial ou un número insuficiente de iteracións nos algoritmos da reconstrución poden levar a diminucións no SUV. Finalmente, os valores de SUV son altamente dependentes do volume da rexión de interese utilizadas para a medición e do tipo de normalización escollida. A maioría destes resultados foron obtidos mediante a adquisición de manequíns físicos en escáneres clínicos. Estes manequíns son ideais para investigar o impacto destes cambios nos parámetros técnicos sobre a imaxe final, permitindo facer probas que non sería posibles con pacientes. Con todo, estes manequíns están limitados pola súa pouca flexibilidade para probar diferentes formas e volumes, o seu custo e o complexo do seu manexo. Unha alternativa a estes manequíns é a utilización de técnicas de simulación e de manequíns virtuais, que permiten a obtención de imaxes simuladas analiticamente ou mediante métodos máis complexos, como a simulación Monte Carlo (MC). O uso destas técnicas permítenos avaliar un gran número de factores nun ambiente totalmente controlado onde todos os parámetros son coñecidos, cun custo moi baixo e sen necesidade de manipular fontes de radiación ionizante.

Nesta tese desenrolamos unha metodoloxía para a avaliación de diferentes métodos de cuantización baseados en valores de SUV utilizando a simulación MC e para a xeración de bases de datos de estudos simulados de TEP-FDG, utilizando manequíns antropomórficos dixitais. Esta metodoloxía foi aplicada a varios problemas relacionados coa cuantización que non foran avaliados previamente.

Nun primeiro traballo estudamos os efectos da extravasación da dose inxectada como fonte de incerteza para a cuantización baseada en SUV. As directrices actuais para PET de corpo enteiro recomendan non realizar a cuantización cando se observa extravasación, unha solución pouco eficaz pola alta incidencia deste fenómeno, polo que se propuxo o desenvolvemento dun método de corrección. 1367 imaxes clínicas foron avaliadas, mostrando que a extravasación é relativamente común (18%). Nembargantes, só na metade dos casos (9,5%) se observou que a extravasación representara máis do 1% da dose inxectada (cun máximo do 22% da dose). Dous métodos para corrixir este efecto foron propostos e validados mediante simulación MC, e extraéronse criterios para determinar a aplicación da corrección baseándose no volume e na intensidade do punto de

extravasación. Despois da corrección, o impacto no SUV foi sempre menor do 5%, permitindo a correcta cuantización destas imaxes.

Nun segundo estudo decidimos avaliar o impacto do ruído debido á inxección de doses máis baixas na precisión e repetibilidade dos valores de SUV calculados con tres métricas distintas (SUV_{max}, SUV_{medio} e SUV_{50}). Este tipo de estudo é útil para o axuste de dose, especialmente para estudos de seguimento. Os resultados demostraron que os valores de SUV_{max} sobreestiman sistematicamente os valores de actividade, mentres que o SUV_{medio} os subestima. Os valores SUV_{50} foron os máis precisos representando o valor real de actividade, xa que só se observou unha lixeira subestimación da actividade en lesións moi pequenas. Por outra banda, o SUV_{medio} mostrou a mellor repetibilidade, proporcionando unha variabilidade menor do 5% para todos os tamaños de tumor e para todas as doses superiores a 111 MBq.

A mesma metodoloxía foi utilizada para avaliar o impacto de cambios fisiolóxicas na captación do tecido muscular no SUV. Estudos anteriores informaron que os niveis altos de captación muscular pode crear problemas na diferenciación visual de tecido normal e patolóxico, causando a aparición de falsos positivos. Sen embargo, a influenza deste efecto sobre a cuantización non fora avaliado previamente. Simuláronse adquisicións PET-FDG dunha base de datos de manequíns antropomórficos con diferentes niveis de absorción muscular e nódulos pulmonares con diámetros 31, 21 e 9 mm. Realizáronse varias repeticións para avaliar a variabilidade. Unha distribución realista dos valores musculares obtívose a partir de 136 doentes aos que se realizaron probas no noso Servizo de Mediciña Nuclear. Os valores de SUV en base a diferentes métricas calculáronse para diferentes repeticións, lesións pulmonares e niveis de captación muscular. Concluíuse que as variacións musculares teñen un grande impacto sobre os valores de SUV, sendo un factor dominante na incerteza para os valores de dose utilizados na práctica clínica.

Finalmente, os nosos modelos MC aplicáronse a outro radiomarcador, a 18F-colina (FCH), dando lugar á primeira base de datos de manequíns dixitais coa biodistribución deste marcador. O obxectivo do estudo foi o de estudar a influenza das contas entre rexións adxacentes polo efecto de volume parcial, o que pode afectar a cuantización de pequenas lesións que están preto de grandes áreas de alta captación. Este efecto pode causar problemas na cuantización de SUV en rexións próximas a áreas tales como o da vexiga en marcadores baseados en ^{18}F. Simuláronse manequíns con biodistribución de FCH con distintas absorcións na vexiga, e valorou-se o efecto desas variacións nos valores de SUV de tumores de próstata. Observouse que estas variacións poden invalidar os valores cuantitativos, e propúxose unha corrección baseada na modificación dos métodos de reconstrución. Esta corrección elimina calquera rastro da vexiga na imaxe, mostrando unha reproducibilidade adecuada nos valores de SUV, con variacións por debaixo do 5%. Tamén se demostrou que a eliminación da vexiga por esta técnica mellora notablemente a detección das lesións na inspección visual.

Resumen

La tomografía por emisión de positrones (TEP) es una técnica de imagen no invasiva que visualiza la distribución de diferentes moléculas en el cuerpo humano, proporcionando información funcional sobre los diferentes tejidos. La TEP se usa rutinariamente para el diagnóstico, el estadiaje y la evaluación de la respuesta al tratamiento en oncología, siendo la 18F- fluorodesoxiglucosa (FDG) el radiotrazador más utilizado en la actualidad. A pesar de que evaluación de las imágenes se ha realizado tradicionalmente mediante inspección visual, el verdadero potencial de la TEP reside en la posibilidad de proporcionar valores cuantitativos, los cuales se obtienen normalmente mediante el cálculo del valor de captación estándar (SUV, por sus siglas en inglés), un parámetro semi-cuantitativo que se mide rutinariamente en el 90% de los centros a nivel mundial. Este parámetro nos proporciona una caracterización relativamente objetiva del tumor, criterios de malignidad/benignidad y valores cuantificables para el seguimiento y evaluación de la terapia. Sin embargo, la robustez de los valores de SUV ha sido cuestionada en numerosas ocasiones por la comunidad científica, ya que estos valores pueden estar afectados por múltiples fuentes de incertidumbre, ya sean cambios fisiológicos entre diferentes estudios del mismo paciente, cambios en el manejo del mismo o problemas técnicos relacionados con los protocolos de adquisición, reconstrucción y cuantificación. Muchos autores han apuntado a la necesidad de estandarización de los protocolos para minimizar el impacto de estos factores, esfuerzos que se han visto reflejados en la publicación de diferentes guías por parte de la Sociedad Europea de Medicina Nuclear (EANM) y de la Sociedad Americana de Medicina Nuclear e Imagen Molecular (SNMMI). Estas guías incluyen recomendaciones para la preparación previa del paciente y la adquisición, reconstrucción y cuantificación de los estudios. Sobre las fuentes de error relacionadas con factores fisiológicos, se ha demostrado que altos niveles de glucosa, los movimientos involuntarios durante el estudio o la captación en grasa parda debida al estrés o al frío se relacionan con valores de SUV más bajos, mientras que la prolongación del tiempo de captación puede provocar un incremento de estos valores. En cuanto a los protocolos de adquisición y reconstrucción, se ha demostrado que los niveles altos de ruido pueden provocar variaciones de los valores de SUV, y que los límites de resolución espacial o un número insuficiente de iteraciones en los algoritmos de reconstrucción pueden llevar a disminuciones en el SUV. Finalmente, los valores de SUV son altamente dependientes del volumen de la región de interés utilizada para su medición y del tipo de normalización que se realice. La mayoría de estos resultados se han obtenido utilizando maniquíes físicos en escáneres clínicos. Estos maniquíes son ideales para investigar el impacto de las variaciones de parámetros técnicos sobre la imagen final, permitiéndonos hacer pruebas que no serían posibles con pacientes. Sin embargo, están limitados por su limitada flexibilidad a la hora de probar distintas formas y volúmenes, tienen un coste elevado y su uso es técnicamente delicado. Una alternativa a estos maniquíes es el uso de técnicas de simulación y de maniquíes virtuales, que nos permiten obtener imágenes simuladas, ya sea analíticamente, o por métodos más complejos como el de simulación de Monte Carlo (MC). El uso de estas técnicas en lugar de adquisiciones reales nos permite evaluar numerosos factores en un entorno totalmente controlado donde todos los parámetros son conocidos a priori, con un coste muy bajo y sin la necesidad de manipular fuentes de radiación ionizante.

En esta tesis doctoral hemos desarrollado una metodología para la evaluación de diferentes métodos de cuantificación por SUV basada en la simulación por MC y en la generación de bases de datos de estudios simulados mediante el uso de maniquíes antropomórficos digitales. Esta metodología se ha aplicado a diferentes problemas relacionados con la cuantificación que no habían sido evaluados previamente.

En un primer estudio hemos evaluado los efectos de la extravasación de la dosis inyectada como una fuente de incertidumbre para la cuantificación por SUV. Las guías actuales para PET de cuerpo entero recomiendan descartar la cuantificación cuando se observe este fenómeno, lo cual es poco óptimo debido a alta incidencia de este fenómeno, lo que hace necesario el desarrollo de un método de corrección. Se evaluaron 1367 pacientes, mostrando que la extravasación es un fenómeno

relativamente frecuente (18%), pero que solo en la mitad de los casos (9.5%) esta representa más del 1% de la dosis inyectada (máximo de 22% de la dosis). Dos métodos para hacer una estimación de la dosis extravasada fueron propuestos y validados utilizando simulación MC. Se propuso un criterio para aplicar la corrección basado en el volumen e intensidad de la corrección, que nos permite asegurarnos que el impacto de la extravasación sobre el SUV será siempre menor del 5%, permitiendo la cuantificación de estos pacientes.

En un segundo estudio decidimos estudiar el impacto del ruido, debido a la inyección de dosis bajas, en la precisión y repetitividad de los valores de SUV para tres métricas distintas (SUV_{max}, SUV_{medio} y SUV_{50}). Este tipo de estudios es útil para la optimización de la dosis, especialmente para estudios de seguimiento. Los estudios mostraron que los valores de SUV_{max} sobreestiman sistemáticamente los valores de actividad, mientras que el SUV_{medio} los sobreestiman. Los valores de SUV_{50} fueron los más preciosos a la hora de representar el valor real de la actividad, ya que solo mostraron una ligera subestimación de la actividad para lesiones muy pequeñas. Por otro lado, el SUV_{medio} mostró la mejor repetitividad, proporcionando una variabilidad menor del 5% para todos los tamaños de tumor y para todas las dosis por encima de 111 MBq.

La misma metodología se usó para evaluar el impacto de las variaciones fisiológicas en la captación del tejido muscular sobre la cuantificación basada en SUV. Estudios previos habían reportado que valores altos de captación muscular podrían crear problemas en la diferenciación visual de tejido normal y patológico, propiciando la aparición de falsos positivos. Sin embargo, la influencia de este efecto sobre la cuantificación no se había evaluado previamente. Se simularon adquisiciones de TEP-FDG de una base de datos de maniquíes antropomórficos que incluían diferentes niveles de captación muscular y nódulos pulmonares de diámetros 31, 21 y 9 mm. Múltiples repeticiones se realizaron para evaluar la variabilidad. La distribución realista de los valores musculares se obtuvo del análisis de 136 pacientes remitidos a nuestro Servicio. Se evaluaron diferentes métricas basadas en SUV para las diferentes repeticiones, lesiones pulmonares y captaciones muscular. El análisis estadístico demostró que las variaciones musculares tienen un gran impacto en los valores de SUV, siendo uno de los factores dominantes en la incertidumbre para los valores de dosis utilizados en la práctica clínica.

Finalmente, nuestros modelos de MC se aplicaron a un nuevo trazador, la ^{18}F-colina (FCH), creando la primera base de datos de maniquíes digitales con la biodistribución de este trazador. El objetivo del estudio era estudiar la translocación de cuentas entre regiones adyacentes debido al efecto de volumen parcial, que puede afectar a la cuantificación de lesiones pequeñas que están cerca de zonas extensas de alta captación. Este efecto puede provocar problemas en la cuantificación de SUV en regiones cercanas a zonas como la vejiga en los trazadores basado en ^{18}F. Los maniquíes con biodistribución de FCH se simularon con captaciones de trazador en vejiga de distintas intensidades, y se evaluó el efecto de estas variaciones en los valores de SUV de tumores insertados en la próstata. Se observó que estás variaciones podían invalidar los valores medidos, y se propuso una corrección basada en la adaptación de la metodología de reconstrucción. Los valores medidos utilizando dicha corrección, que elimina toda contribución de la vejiga de la imagen, mostraron una reproducibilidad adecuada, con desviaciones menores al 5%. También se demostró que la eliminación de la vejiga mediante esta técnica mejoraba sensiblemente la detectabilidad de las lesiones en la inspección visual.

Agradecimientos

Después de años de lectura, experimentos y simulaciones, cuando al final de todo comienzo a escribir estos agradecimientos, me resultan una de las partes más difíciles. He caído en la tentación buscar de ejemplos, pero parece no ser apropiado citar otros trabajos en los agradecimientos, lo cual me deja con la ardua tarea de sincerarme en estas líneas. A pesar de ello, no he podido evitar inspirarme en un buen amigo para dar formato a estas páginas.

En primer lugar, debo agradecer de la manera más especial y sincera al Profesor Álvaro Ruibal por aceptarme para realizar esta tesis doctoral bajo su dirección. Su apoyo, su confianza en mi trabajo, su ayuda y sus comentarios han sido un aporte imprescindible.

"La conducta que genera más credibilidad e inspira más confianza es actuar por el bien de los demás"

Stephen Covey Jr.

A mi director, el doctor Pablo Aguiar, por haberme dado una oportunidad de trabajar con él, por su inestimable ayuda, paciencia y conocimientos, y por el trato que me brindo desde el primer día. Pero por encima de todo, por la complicidad, el aprecio mutuo y la amistad, que tienen para mi muchísimo más valor que cualquier logro académico, y que son lo más valioso que me llevo de estos años de tesis doctoral.

"El ejemplo no es lo que más influencia a las personas. Es lo único"

Albert Schweitzer

Al Profesor Faustino Gómez, por haberme ayudado en mis comienzos en la investigación. Sus lecciones y su confianza han sido determinantes para que hoy esté escribiendo estas líneas.

"Elige un empleo que te guste y no tendrás que trabajar ni un día más en la vida"

Confucio

A todos los investigadores que han pasado por nuestro grupo de investigación con los que he tenido la suerte de compartir estos años. También a los miembros del GIR de la USC, a los que también considero compañeros. Juan, Lara, Noemí, Anxo, Martín, Alexis, Diego, Aurelio, Araceli. Gracias por la ayuda, la colaboración, el compañerismo, los cafés, las cenas, las risas...

"El talento gana partidos, pero el trabajo en equipo y la inteligencia ganan campeonatos"

Michael Jordan

A todo el personal del Servicio de Medicina Nuclear del CHUS, por haberme tratado con tanto cariño y aprecio desde el primer día. Me gustaría agradecer de manera especial a la Dra. Inés Domínguez y al Dr. Manuel Sánchez por su colaboración en esta tesis.

"Se necesitan dos piedras para hacer fuego"

Louisa May Alcott

A la Dra. Julia Cortés, a la que tengo un aprecio que sería difícil de plasmar en estas líneas. Muchísimas gracias por todo, Julia.

"Si yo hago lo que tú no puedes, y tú haces lo que yo no puedo, juntos podemos hacer grandes cosas"

Madre Teresa de Calcuta.

To all my colleagues in the University of Leeds (very especially to Demetra and Nikos), thank you so much for making me feel like being home even so far away. Of course, to Professor Harry Tsoumpas, for giving me the opportunity of having one of the most enriching experiences in my life, and for our discussions about image reconstruction, which I remembered so often while writing this dissertation.

"If you only do what you can do, you will never be better than what you are now"

Master Shifu (Kung Fu Panda 3)

A Alex, David, Jacob, Pablo, Haxel Lionel, Miguel, Brais y Chain. Y a todas las personas que me dejo en el tintero y que han compartido estos años conmigo. Dicen que la vida es lo que te pasa mientras te empeñas en hacer otros planes. Gracias por haberme pasado.

"La amistad no puede ir muy lejos cuando ni unos ni otros están dispuestos a perdonarse los pequeños defectos"

Jean de la Bruyere

A Manu, Toti, Belén, Kike, Chus, Gloria y a toda la gente de la familia Sonar. Gracias por contradecir eso de que la gente que conoces de noche en un bar en realidad no son tus amigos.

"Mientras quede un plato de lentejas pa´la cena, gente buena y ganas de reír,
Puede que valga la pena luchar pa sobrevivir."

Rafa Pons. Letra de "Filatélico"

A Franchu, Yuru y Juan. No necesito deciros demasiado. Los amigos son la familia que escogemos, y vosotros me escogisteis a mí. Gracias por aceptar la difícil misión de tratarme y soportarme. Gracias por estar siempre ahí.

"Chuckie no es tu amigo, es tu familia. Él se tiraría en pleno tráfico por ti"

Sean (El indomable Will Hunting)

A Carol, por haberme arañado la primera sonrisa de cada día. Por un fin de semana en Camposancos, por un paseo en la playa del Silencio. Por tantas noches enteras hablando en el coche. Por un "no te beso, que fumaste" ... Por congelarse en Heidelberg. Por un atardecer en Mallorca. Por una canción de Cifuentes…

"... y asi es como empiezo a soñarte en la casa, vestida de domingo en zapatillas y pijama…"

Paco Cifuentes. Letra de "Vestida de domingo"

Y por supuesto y por encima de todo a las dos personas más importantes de mi vida, mis padres. Soy muy feliz y muy afortunado. Gracias, no solo por criarme como la habéis hecho, sino por apoyarme siempre en todo. También a mis abuelas, que sin saber realmente lo que significa leer una tesis doctoral, se sentirán igualmente orgullosas de mí.

"Por los libros que sostuve me mantengo.
Llevo con la voz un acento de sal.
He llorado con un beso no robado.
Por remar junto a mis padres soy verdad.
En esta vida vi salir del agua mil delfines,
rezar a dioses que no existen pero matan a gente.
Fui con la guitarra hasta Madrid.
Eché de menos a mis padres, eché de más algunos bares...
viví feliz."

Andrés Suárez. Letra de "Tengo 26"

Contents

1 INTRODUCTION TO MEDICAL IMAGING 3
1.1 COMPUTED TOMOGRAPHY 4
1.2 MAGNETIC RESONANCE IMAGING 5
1.3 ULTRASOUND 5
1.4 NUCLEAR MEDICINE 6
1.4.1 SPECT 7
1.4.2 PET 8
2 POSITRON EMISSION TOMOGRAPHY 13
2.1 PET PHYSICS 13
2.1.1 Positron and beta decay *13*
2.1.2 Radiation-matter interaction *14*
2.1.2.1 Atomic level *14*
2.1.2.2 Macroscopic level *15*
2.2 PET DATA ACQUISITION 17
2.2.1 PET Detectors 17
2.2.1.1 Scintillators *17*
2.2.1.2 Photodetectors *19*
2.2.1.3 Detector arrangements *20*
2.2.1.4 Electronics *21*
2.2.1.5 *PET detector characterization* *22*
2.2.2 PET scanners 22
2.2.2.1 Event detection in PET *23*
2.2.2.2 The sinogram *24*
2.2.2.3 Axial Sampling *25*
2.2.2.4 List mode acquisition *27*
2.3 PET DATA CORRECTIONS 28
2.3.1 Attenuation Correction 28
2.3.1.1 Positron-emitting transmission sources *29*
2.3.1.2 CT-based attenuation correction *29*
2.3.2 Scatter Correction 29
2.3.2.1 Multiple Energy Windows 30
2.3.2.2 Monte Carlo Simulations *31*
2.3.2.3 Single Scatter Simulation (SSS) *31*
2.3.3 Randoms Corrections 31
2.3.3.1 Tail Fitting *31*
2.3.3.2 Estimation from singles *32*
2.3.3.3 Delayed Coincidence Channel *32*
2.3.4 Data Normalization 32
2.3.5 Dead time correction 33
2.4 PET PERFORMANCE MEASUREMENTS 35
2.4.1 Sensitivity 35
2.4.2 Spatial Resolution 36
2.4.3 Noise and scatter fraction 37
2.4.4 Image quality 38
3 IMAGE RECONSTRUCTION 41
3.1 ANALYTICAL RECONSTRUCTION METHODS 41
3.1.1 Filtered back-projection (FBP) 41
3.1.2 3DRP and Rebinning Algorithms 43
3.2 ITERATIVE RECONSTRUCTION 44
3.2.1 Maximum Likelihood Expectation-Maximization 45
3.2.2 Ordered Subsets Expectation-Maximization (OSEM) 46

3.2.3 New developments on iterative reconstruction 46
3.2.3.1 Including physical effects into the SRM 46
3.2.3.2 Reducing noise 47
3.2.3.3 Time of Flight (TOF) 48
3.3 THE STIR LIBRARY 48
4 CLINICAL PET 51
4.1 FDG-PET IN ONCOLOGY 51
4.2 PET IN NEUROLOGY 55
4.3 PET IN CARDIOLOGY 56
4.4 FUTURE DEVELOPMENT 56
4 PET QUANTIFICATION 61
5.1 SUV 62
5.1.1 Applications of SUV in the clinical practice 63
5.1.2 Limitations of the SUV 63
5.2 BEYOND SUV 63
5.2.1 Metabolic Tumor Volume (MTV) and total lesion glycolysis (TLG) 63
5.2.2 Heterogeneity and textural analysis 64
6 MONTE CARLO SIMULATION 69
6.1 MC METHODS IN NUCLEAR MEDICINE 69
6.1.1 MC methods for assessing quantification methods *69*
6.1.1.1 SimSET 2.9.2 71
6.2 ANTRHOPOMORPHIC PHANTOMS 72
6.2.1 The XCAT phantom 73
7 AIMS OF THIS THESIS 77
7.1 STATEMENT OF THE PROBLEM 77
7.2 GENERAL AIM 78
7.3 SPECIFIC AIMS 78
8 COHESION OF THIS THESIS 81
9 CORRECTION FOR FDG PET DOSE EXTRAVASATIONS: MONTE CARLO VALIDATION AND QUANTITATIVE EVALUATION OF PATIENT STUDIES 85
10 SIMULATED FDG-PET STUDIES FOR THE ASSESSMENT OF SUV QUANTIFICATION METHODS 95
11 IMPACT OF MUSCULAR UPTAKE AND STATISTICAL NOISE ON TUMOR QUANTIFICATION BASED ON SIMULATED FDG-PET STUDIES 103
12 IMPACT AND CORRECTION OF THE BLADDER UPTAKE ON ^{18}F-FCH- PET QUANTIFICATION: A SIMULATION STUDY USING THE XCAT2 PHANTOM 113
13 DISCUSSION 131
13 CONCLUSIONS 137
References 139

1

Introduction to medical imaging

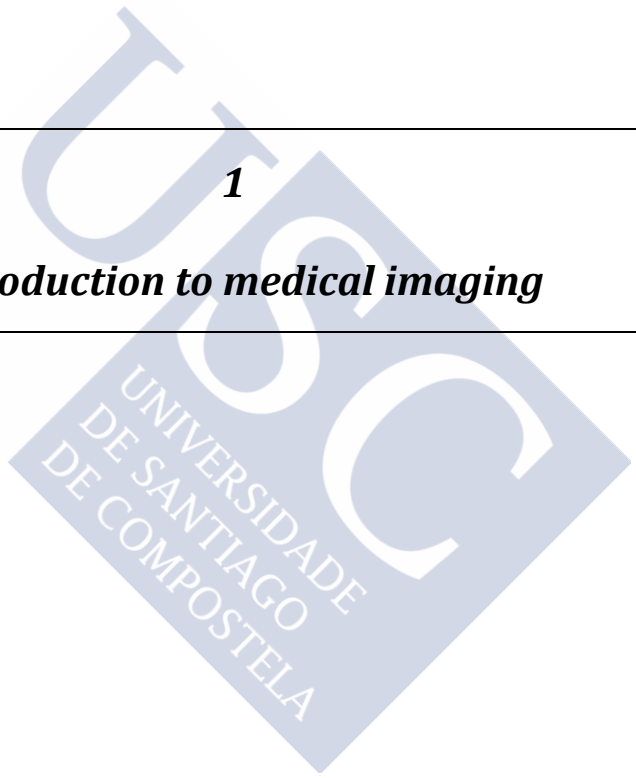

USC
UNIVERSIDADE
DE SANTIAGO
DE COMPOSTELA

1 INTRODUCTION TO MEDICAL IMAGING

In 1895, German physicist Wilhelm Conrad Roentgen (*Figure 1.1*) discovered X-rays while he was carrying out experiments with cathode ray tubes. Roentgen quickly understood that this new radiation could penetrate matter, and he named it as "X" due to its mysterious nature. Upon the following years, he took hundreds of images, and in 1901, he received the Nobel Prize in Physics for the discovery and study of X-rays. The image of his wife's hand wearing her wedding ring (*Figure 1.2*) is nowadays a symbol of the start of medical imaging. Unfortunately, Wilhelm Roentgen was unaware of the dangers of the systematic exposure to ionizing radiation, and both he and his wife died from cancer. Physicians quickly perceived X-rays as a new way of exploring the body and a revolutionary method for detecting skeletal lesions, and few years after Roentgen's discovery, X-ray radiographs became an essential part of the medical equipment on World War I. Radiographs also became popular as a method for the assessment of tuberculosis and other lung diseases (Scatliff & Morris, 2014).

Figure 1.1: Wilhelm Conrad Röntgen (1845-1923)

A few years later (1925), Binz and Rath introduced iodine as a contrast agent for X-ray imaging (Quader et al., 2000). Due to the small density differences between different soft tissues, distinguishing the borders of different organs was very challenging, reducing the application of X-ray imaging to bone imaging. Nevertheless, the administration of compounds with high electron density and atomic number facilitated the visualization of certain tissues and achieved enhanced contrast of certain organs. Materials as iodine and barium (Z = 53 for iodine, Z = 56 for barium) were administered in order to obtain better visualization of the digestive track and for the diagnosis of lung diseases (Lusic & Grinstaff, 2013). Despite being a minor discovery compared with X-rays, the use of contrasts in early radiographic imaging was a precursor of the administration of contrast agents in modern imaging modalities, and a previous step for the development of emission tomography by using radioactive tracers, which is the fundament of Nuclear Medicine.

Figure 1.2: One of the first radiographies, taken by Wilhelm Roentgen in 1895.

1.1 COMPUTED TOMOGRAPHY

One of the main limitations of X-ray images is that they represent a three-dimensional object as a two-dimensional image. Thus, some parts of the body cannot be imaged since they are hidden behind high-density tissues. In 1956, while he was working on astrophysics, Ronald N. Bracewell postulated the central slice theorem, the central milestone of modern medical imaging. The theorem states that a three-dimensional distribution can be reconstructed from two-dimensional projections of the object at different angles. Using this property, Godfrey Hounsfield developed the first X-ray Computed Tomography (CT) machine in 1979 (Herman, 2009). This advancement granted him the Novel Prize in 1979, which he shared with Allan Cormack. The usage of CT has dramatically increased since then (97 million scans were performed in the United States in 2015), and nowadays it has applications for lung cancer screening, neurology, virtual colonoscopy or cardiac imaging. (Brenner & Hall, 2007). *Figure 1.3* shows a coronal slice of a whole-body tomographic image acquired on a modern CT scanner.

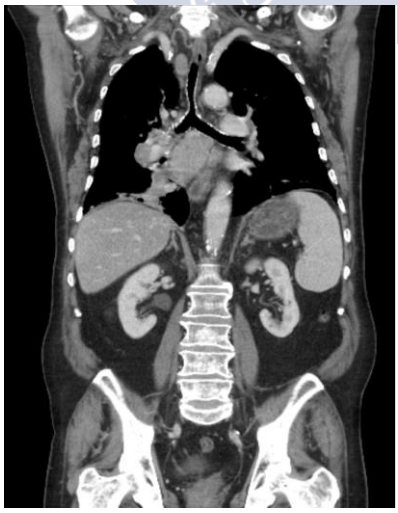

Figure 1.3: CT image of the human body, granted by the Department of Radiology, University Hospital, Santiago de Compostela. The image corresponds to a patient with lung carcinoma. High-density tissues (i.e. bone) appear bright due to high attenuation of the X-ray beams, while low-density tissues (i.e. lung) appear dark.

1.2 MAGNETIC RESONANCE IMAGING

Parallel to the development of CT, in 1973 Paul Lauterbur introduced Magnetic Resonance Imaging (MRI) and published the first images exploiting the magnetic resonance phenomena discovered by Felix Bloch and Edward Purcell thirty-one years earlier. When any material is placed in a strong magnetic field, the spins of the protons of its hydrogen atoms align according to the field direction. Then, a radiofrequency causes the hydrogen nuclei spins to rotate around the magnetic field direction. When the radiofrequency source is switched off, the spins return to their rest state emitting different radiofrequency signals depending in the type of tissue. These signals can be measured and reconstructed into an image (Berger, 2002). Nevertheless, first MRI scanners had very bad sensitivity and needed extended acquisition times, making it impractical for the clinical practice. On 1977, Peter Mansfield developed echo-planar imaging, which made possible to acquire medical images in a few minutes and the application of MRI in the clinical routine. In 2003, both Mansfield and Lauterbur received the Nobel Prize for their revolutionary contributions to medicine. The main practical advantage of MRI compared to CT relies on its ability to obtain high-contrast images of soft tissue. Furthermore, MRI spread quickly thanks to the fact that, in contrast with X-ray based techniques, there is no radiation exposure associated with the image acquisition. In *Figure 1.4*, we show an example of a T1 MRI image. T1 is the simplest MRI sequence, and it is based on the measurement of the relaxation times of the hydrogen nuclei once the radiofrequency pulse is switched off. This time varies with the molecular structure, being higher in liquids than in solids, and higher in small molecules such as water than in big molecules like fat lipids.

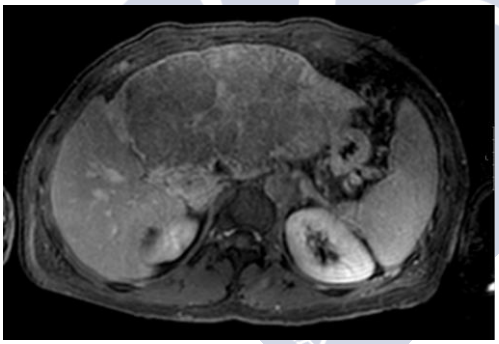

Figure 1.4: Axial slice from an MRI image of a hepatic carcinoma, granted by the Department of Radiology, University Hospital, Santiago de Compostela.

1.3 ULTRASOUND

In 1880, Jacques and Pierre Curie reported that ultrasound waves could create electricity on a quartz crystal, which was named as inverse piezoelectric effect (Manbachi & Cobbold, 2011). In 1929, soviet scientist Sergei Sokolov exploited this effect to propose the theory of sound transmission, which was used a few years later, during the World War II, it was used for the development of sonar. Few years after the war, in 1956, Ian Donald introduced ultrasound in diagnostic medicine. The ultrasound waves were transmitted into the body, and the return wave vibrations are converted into electrical pulses that are transformed into an image *(Figure 1.5)*. Since then, ultrasound has become a very popular imaging modality due to the lack of secondary effects from the ultrasound waves (Hangiandreou, 2003).

Figure 1.5: Ultrasound image of a fetus in the womb, viewed at 12 weeks of pregnancy. Image is granted by Dr. Wolfgang Moroder (Centro Medicina Prenatale Aurora, Bolzano, Italy).

1.4 NUCLEAR MEDICINE

Despite the huge advances provided by X-ray imaging techniques, ultrasound and MRI, these techniques are unable to give information about the biochemistry of cells, which is essential in the era of personalized medicine for the planning and monitoring of any specific treatment. On this regards, Nuclear Medicine uses different endogenous molecules, named as radiotracers, to monitor targeted biological processes. The target molecule is labelled with a radioactive isotope and administered to the patient in order to obtain biochemical and physiological information in vivo. While conventional modalities show only anatomical structures, Nuclear Medicine techniques can image different biological processes using a variety of imaging techniques, such as Single Photon Emission Computed Tomography (SPECT) and Positron Emission Tomography (PET), which can be combined with different labelled radiotracers to provide an extent range of different tests (Vallabhajosula, 2009).

Nuclear medicine is considered to start in 1946, when this term was first used by Sam Seidin in the "Journal of the American Medical Association", where he described the usage of ^{131}I for the treatment of thyroid tumours. Later, the applications of ^{131}I in thyroid cancer extended to imaging and quantification of thyroid function. In these early days of nuclear medicine, measurements were performed by placing a Geiger counter directly above the organ of interest (Jaszczak, 2006), until 1958, when Hal Anger developed the Anger camera (Anger, 1958), allowing the two-dimensional visualization of gamma ray emission. In 1963, Kuhl and Edwards made the first steps of three-dimensional emission imaging (Kuhl & Edwards, 1963), and in 1971, Gerd Muehllehner developed the first SPECT system, consisting on a rotating chair placed in front of a stationary Anger camera (Muellehner, 1971). The same year, the American Medical Association recognized nuclear medicine as a medical specialty. The subsequent development of technology and radiotracers for SPECT was very fast, and in a few years, most cancers, such as liver, spleen or brain tumours could be visualized using nuclear techniques. Parallel to the development of SPECT, the development of PET started in 1952, a long process that culminated in 1989 when the FDA approved ^{82}Rb as the first positron based radiopharmaceutical to evaluate myocardial perfusion. Nevertheless, PET continued to be most of a research tool until 1999, when glucose analogue 2-deoxy-2-(^{18}F)-fluoro-D-

glucose (^{18}F-FDG) received the approval for cancer diagnostic purposes (Wagner, 2007). The advancements of the following decade were focused on improving the resolution and sensitivity of PET cameras and in the development of new radiopharmaceuticals used for carrying the radioactive isotopes directly to specific organs and cancer cells. Nowadays, nuclear medicine, and most importantly ^{18}F-FDG PET, has become an essential tool for personalized medicine in specialties such as oncology, cardiology and neurology.

Besides imaging, Nuclear Medicine continues to provide solutions for therapy. Using the same philosophy, radiopharmaceuticals emitting electrons (β^- emitters), the particles used for radiotherapy, can be attached to adequate molecules that will deliver them to tumours. These electrons will be emitted locally nearby, destroying cancerous cells and providing an efficient treatment while avoiding surrounding healthy tissue. Most common therapy isotope is ^{131}I, which has been used for the treatment of well-differentiated thyroid cancer for over 50 years. More recently, new treatments are being developed for more complex carcinomas. A good example is the use of ^{90}Y microspheres (TheraSphere; MDS Nordion; Ottawa, ON, Canada), which are placed within a hepatocarcinoma vasculature, delivering high doses of radiation and providing lethal insult to cancerous cells, destroying essential tumour vascular flow, and resulting in cell death and tumour necrosis (Salem et al., 2005)

1.4.1 SPECT

Analogous to CT, SPECT images are obtained from obtaining different 2-dimensional projections by rotating an Anger gamma camera around a patient injected with a suitable radiotracer. In SPECT, tracers are labelled with isotopes emitting gamma rays. The gamma cameras need to be attached to collimators, so that only those emitted photons travelling in a specified direction are accepted into the projection. As in CT, tomographic images are obtained acquiring multiple 2D projections around the patient every 2-5 degrees. The 3D distribution can be reconstructed from these projections by using different analytical or iterative reconstruction methods (Bruyant, 2002).

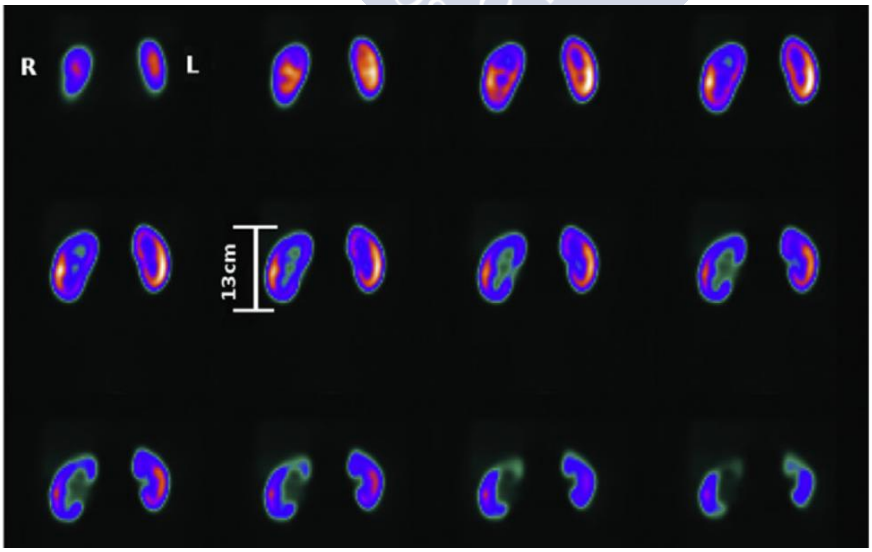

Figure 1.6: Coronal slices of a ^{99m}Tc-DMSA SPECT image showing the radiotracer uptake on the renal cortex. Image reproduced from Silva-Rodríguez et al. (2015).

SPECT radiotracers are labelled with gamma-emitting isotopes such as ^{99m}Tc, ^{111}In or ^{123}I, with energies typically in the range between 100 keV and 300 keV. The labelling of different molecules with those isotopes allows assessing different biological functions, such as myocardial perfusion (99mTc-Sestamibi, 99mTc-Tetrasfosfin), brain perfusion (99mTc-HMPAO, 99mTc-ECD), bone metastases (99mTc-HDP) or renal function (99mTc-DMSA). *Figure 1.6* shows an example of SPECT image using ^{99m}Tc-DMSA for evaluating renal function.

1.4.2 PET

The fast development of SPECT encouraged scientists to develop new tools for emission tomography. From the beginning, it was well known that the use of annihilation radiation could solve the main problems of SPECT, which were related with the low sensitivity derived from the use of collimators. In contrast with the gamma emitting isotopes used in SPECT, PET imaging relies on the nature of the positron and positron decay. When the radioactively labelled radiotracer is injected into the body, the radioisotope atoms will decay emitting positrons (Turkington, 2001). These positrons will quickly annihilate with matter electrons, generating two 511 keV photons travelling in opposite directions, which are detected in coincidence by the PET scanner. The positions of detection of the two photons can be used to reconstruct the line where the positron annihilated or line of response (LOR) (van der Veldt et al., 2013). The lines defined by each gamma pair can be used to perform electronic collimation, removing the need for a physical collimator, making PET much more sensitive than SPECT. The annihilation and detection process is illustrated in *Figure 1.7*.

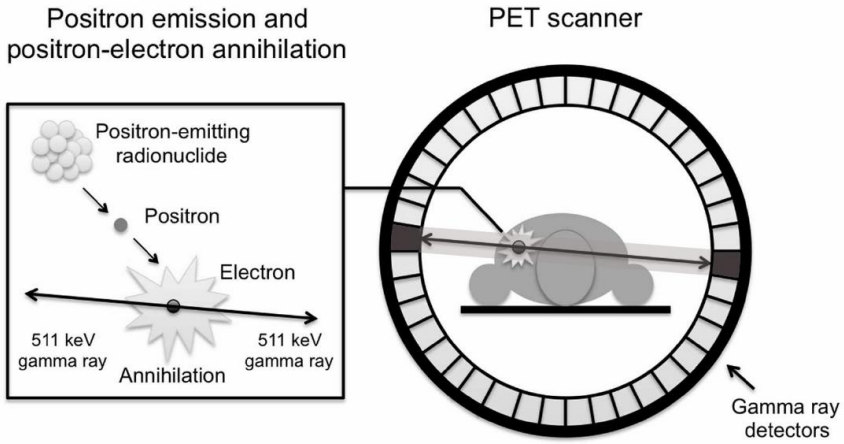

Figure 1.7: Basic principles of PET. Modified from (van der Veldt et al., 2013).

The first prototypes for positron imaging, with two opposed small sodium iodine (NaI) detectors, were developed by Gordon L. Brownell at the Physics Research Laboratory (PRL) in the Massachusetts General Hospital in 1952. Several versions of the two-detector scanner were build, but a step further was needed to significantly increase the sensitivity. The logical evolution was using two 2-dimensional arrays, and the result was the PC-I scanner (*Figure 1.8*) (Brownell et al., 1970), which could produce tomographic images on planes within the object. In 1974, Brownell had a meeting with

nuclear physicist Michael Ter-Pogossian, where they discussed the possibility of a hexagonal arrangement of detectors surrounding the patient. This meeting was crucial for the later development of nuclear medicine, and only one year later, Michael Phelps and Edward Hoffman, working in Ter-Pogossian laboratory, introduced an improved PET scanner with hexagonal detectors (Phelps et al., 1975). Afterwards, Brownell developed at Massachusetts ring and cylindrical shaped detectors (PCR-I (1985) and PCR-II (1988)) providing even better resolution and sensitivity (Portnow et al., 2013). *Figure 1.9* shows the evolution of the resolution and the sensitivity of the positron imaging systems in the Massachusetts General Hospital (Brownell, 1999).

Figure 1.8: PC-I, the first tomographic imaging device. Image reproduced from (Brownell, 1999).

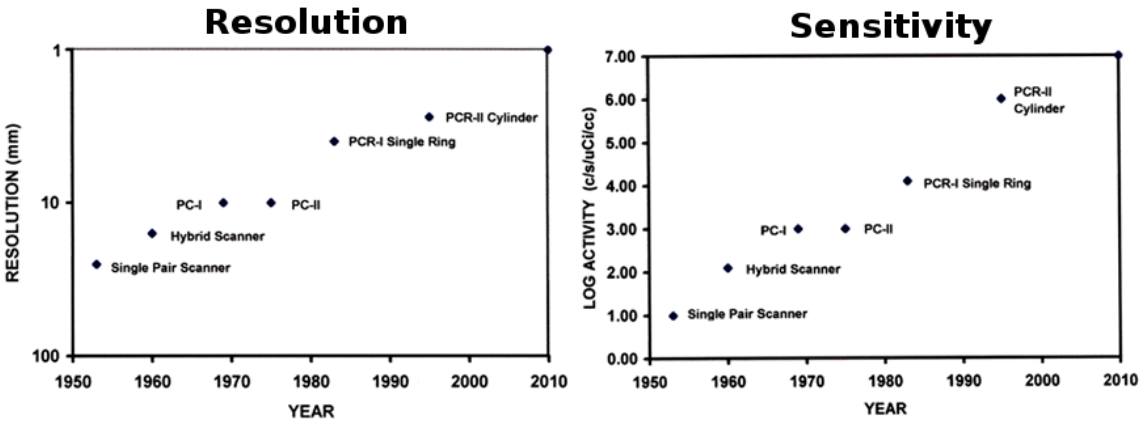

Figure 1.9: Improvement in resolution and sensitivity of MGH PET systems. Reproduced from (Brownell, 1999).

USC
UNIVERSIDADE
DE SANTIAGO
DE COMPOSTELA

2

Positron Emission Tomography

USC
UNIVERSIDADE
DE SANTIAGO
DE COMPOSTELA

2 POSITRON EMISSION TOMOGRAPHY

2.1 PET PHYSICS

2.1.1 Positron and beta decay

In 1928, Paul Dirac predicted the existence of a particle that he called anti-electron, a particle with the mass and spin of the electron but with positive charge. Dmitri Skobeltsyn first observed these particles in 1929 while he was using a cloud chamber to study gamma radiation in cosmic rays. When a particle passes through the chamber, it interacts with the contained gas creating a trail, which is characteristic of each type of particle. In 1932, Carl David Anderson observed the same phenomena, which he described as "particles that acted like electrons but were curved in the opposite direction by a magnetic field". He published a detailed study in the P*hysical Review* journal, where he used the term "positron" for the first time (Anderson, 1933). In 1936, he was awarded with the Nobel Prize in Physics for his experiments, which opened the era of antimatter in experimental physics.

The positron is the most common antimatter particle due to its low mass, and it is naturally produced by the decay of β^+emitters. These are atoms that need to convert protons into neutrons to reach a more stable state with a more optimal proton/neutron ratio (Turkington, 2001). In β^+ decay, a proton decays into a neutron, and a positron and an electron neutrino are emitted. The emission of the positron and the neutrino occurs in order to fulfil physics conservation laws. Thus, the general equation for positron decay is:

$$ {}^{A}_{Z}X \rightarrow {}_{Z-1}{}^{A}Y + \beta^+ + \nu_e + Q $$

where A is the mass number (number of protons and neutrons), Z is the atomic number (number of protons), X is a proton–rich atom that needs to convert a proton to a neutron, Y is the resulting daughter atom, ν_e is the neutrino and β^+ is the emitted positron . As the resulting atom is in a more stable state, the remaining energy *Q* appears as the kinetic energy of the resulting particles. The energy of an emitted beta particle from a particular decay can take on a range of values up to a maximum, since the energy can be shared in many ways among the three particles while still obeying energy and momentum conservation.

Natural positron emitters are rare because most nucleus are neutron rich rather than proton rich, and electron emission is energetically favoured over positron emission because neutrons are more massive than protons. Nowadays, positron-emitting radioisotopes are artificially produced in particle accelerators by proton bombarding or by using column-based generator for their usage in science and medicine. Most popular β^+emitters are, among others, ^{11}C, ^{13}N, ^{15}O,^{18}F, ^{68}Ga and ^{82}Rb. *Table 2.1* shows some of the relevant physical properties of these isotopes.

After emission, the positron loses its initial kinetic energy by interacting with surrounding matter by different elastic and inelastic interactions, deflecting the positron's

path through matter (Bailey et al., 2005). When the positron energy is low, the positron will annihilate with a matter electron. The positron range is the distance travelled by positron from the site of emission to the point of the annihilation. This distance depends both on the initial kinetic energy and on the density of the surrounding material. The mass of the two particles is converted to energy, emitting two 511 keV photons. This reaction is the basis of PET, since they will be these two photons that will be detected by the PET camera.

Isotope	Half-life (min)	Maximum Positron Energy (KeV)	Positron range in water (mm)	Production Method
^{18}F	109.80	640	1.0	Cyclotron
^{11}C	20.30	960	1.1	Cyclotron
^{13}N	9.97	1190	1.4	Cyclotron
^{15}O	2.03	1700	1.5	Cyclotron
^{68}Ga	67.80	1890	1.7	Generator
^{82}Rb	1.26	3150	1.7	Generator

Table 2.1: Most relevant artificial radioisotopes and some of their properties.

2.1.2 Radiation-matter interaction

2.1.2.1 Atomic level

The 511 keV photons emitted in the annihilation will travel through matter in opposite directions, interacting with it by different mechanisms, losing energy and deflecting their path as it previously happened to the positron. Two interaction mechanisms are relevant for the range of energies of interest for nuclear medicine: photoelectric effect and Compton scattering (Bailey et al., 2005).

In the ***photoelectric effect***, the travelling photon is completely absorbed by an atom and the photon energy is transferred to an electron, which is ejected from the atom. We call this a photoelectron. Part of the incident energy is used to unbind the electron, and the rest of the energy is carried out by the electron in the form of kinetic energy. If the ejected electron is in an inner shell, an outer shell electron will replace it, emitting the excess energy as an X-ray photon. The photoelectric effect dominates in human tissue at energies below 100 keV, and while it is relevant for SPECT, it is of little importance for 511 keV photons in PET.

Compton scattering is a more complex interaction usually between a photon and an outer bound electron. An illustration of the Compton Effect process is shown in *Figure 2.1*. As the electron is poorly bounded, it can be considered as a free particle. In Compton scattering, the photon (λ) transfers part of its energy to the electron (e^-). After the interaction, the electron is ejected from the atom and the photon is deflected from its original path. The energy lost by the atom is used to unbind the electron and as kinetic energy of the ejected electron. Since almost all of it is given to the electron as kinetic energy, the photon is deflected as a consequence of the conservation of momentum, resulting in a photon with different direction and energy (λ'). In contrast with

photoelectric effect, the photon will continue travelling through matter. Not all the deflecting angles have the same probability, being small angles the most probable. Compton Effect is the dominant interaction between 100 keV and 2 MeV, and it is of paramount importance for PET.

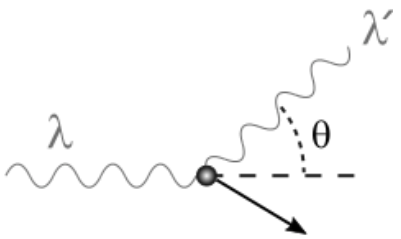

Figure 2.1: Illustration of Compton scattering. A photon λ with initial energy E_0 interacts with an electron. The photon goes out as λ', deflected an angle θ.

Another radiation-matter mechanism to be remarked is ***pair production***. When a photon travels carrying energy higher than 1022 keV, it can spontaneously convert its energy in mass under certain conditions, producing a positron-electron pair. Of course, as this only occurs upon 1022 keV, pair production is of no interest for PET imaging.

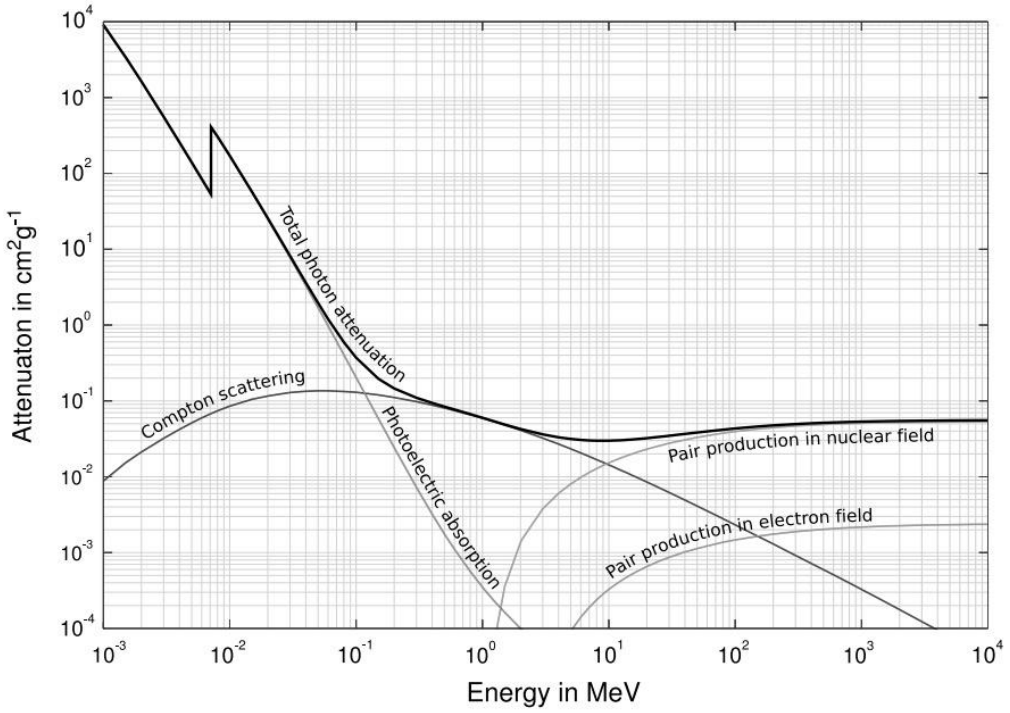

Figure 2.2: Contribution of the different described processes to the total cross-section. (Source: Nuclear Power non-profit project)

2.1.2.2 Macroscopic level

Photon interactions can be expressed as atomic cross sections (σ) with units of *cm^2/atom* or *barns/atom (1barn=10^{-24} cm^2).* On a macroscopic point of view, the attenuation of photons in a given path is dependent on the total cross-section:

$$\sigma_{tot} = \sigma_{pe} + \sigma_{cs} + \sigma_{pp} + \sigma_{others}$$

where σ_{tot} is the total cross-section, σ_{pe} is the contribution of photo-electric effect, σ_{cs} is the contribution of Compton scattering and σ_{pp} is the contribution of pair production. We named σ_{others} the contribution of other phenomena. These contributions can be expressed as mass attenuation coefficients ($^{\mu}/_{\rho}$):

$$^{\mu}/_{\rho}\,(cm^2 \cdot g^{-1}) = \frac{\sigma_{tot} \cdot N_A}{A}$$

where N_A is the Avogadro's number and A is the atomic mass of the material. Contributions of the different cross-sections to the total cross-section can be observed in *Figure 2.2*, where we can observe, as mentioned before, that Compton scattering is the most important mechanism for energies close to 511 keV, while photoelectric effect has a small contribution. These mass attenuation coefficients are very useful since they can be converted into linear attenuation coefficients by simply multiplying by the density in g/cm^3. These linear attenuation coefficients represent the probability for a photon to be attenuated by unit of length of the medium. For a photon beam of intensity I_0:

$$I_x = I_0 e^{-\mu \Delta x}$$

where I_0 represents the photon beam intensity at point *0* and I_x represents the photon beam intensity at point Δx, assuming they are being emitted from a collimated source. The attenuation process detailed by this formula is illustrated on *Figure 2.3*.

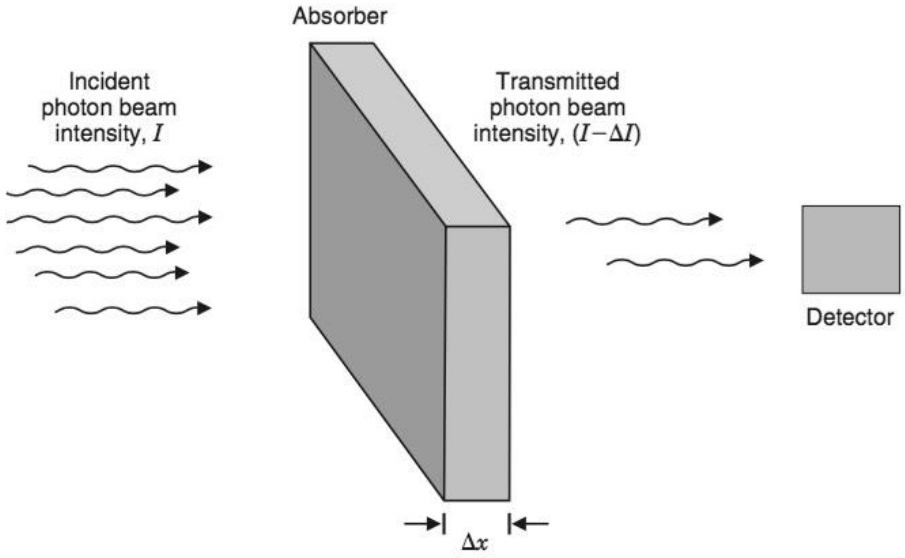

Figure 2.3: Attenuation of a photon beam by an absorber material of linear attenuation coefficient $\mu(cm^{-1})$. Figure is reproduced from (Cherry et al., 2012).

In PET, as two photons are emitted in opposite directions, the count rate is only dependent of the total thickness of the medium, and independent of the point of emission. This property is used for correcting count-rates for attenuation, which will be covered in following sections.

2.2 PET DATA ACQUISITION

PET acquisition is accomplished by detecting the annihilation photons produced when the positron interacts with an electron. This process is divided in two different steps. First, the energy of the photon arriving to the detector is converted into visible light photons by a scintillator crystal. Second, these scintillation photons are converted to electrical signals by a photodetector (Spanoudaki & Levin, 2010). This process is illustrated on *Figure 2.4*. The photodetector is coupled to the appropriate electronics in order to digitalize the signal for further processing. Despite a PET scanner has hundreds or even thousands of these detection elements; its performance characteristics are intimately related with the performance of this small blocks, so the choice and design of its components is crucial.

Figure 2.4: Scheme of the PET detection process. Modified from (Beyer et al., 2010).

2.2.1 PET Detectors

2.2.1.1 Scintillators

Photons will interact with the detector material by causing ionization or excitation of its atoms (Cherry et al., 2012). In the case of PET, the chosen materials are usually inorganic scintillator crystals that emit visible light radiation in form of scintillator photons when a photon interacts with the detector. The photon can deposit part or all of its energy in the detector. The transfer of all the energy can occur by a single photoelectric effect or by several successive Compton interactions in one or adjacent crystals followed by a photoelectric event (Humm et al., 2003). The alternative is that the arriving photon deposits part of its energy by one or multiple Compton events, and then leaves the detector carrying the remaining energy.

The absorbed energy excites the crystal, which decays to its original state by emitting a big number of low-energy photons, usually in the range of visible light. These scintillation photons are collected by a photodetector (*Figure 2.5*); usually the photocathode of a photomultiplier tube (PMT), and their number is proportional to the energy deposited by the primary annihilation photon. In the process of choosing a scintillator crystal, some of its properties should be taken into account. Photon attenuation length is defined as the average distance that a photon will travel through the detector before depositing all its energy, and it is an essential parameter for crystal sensitivity. Photoelectric and Compton cross-sections are a function of the density (ρ) and the

effective atomic number (Z_{eff}) of the crystal, so these properties have to be taking into account when choosing a crystal for a new detector. Higher density provides higher stopping power, making the photons more likely to interact within the crystal, while a big Z_{eff} favours photoelectric effect instead of Compton scattering. In a photoelectric interaction, the photon will deposit all its energy in a single event, being more efficient than the Compton scattering. Other important physical properties are the decay time and the light yield. The decay time is the time that the crystal needs to go back to a stable state after an interaction, being able to register a new interaction. The decay time is mainly related with the time that the scintillation photons need to travel through the detector, usually reflecting multiple times on the crystal walls, before they reach the surface of the photodetector. A longer decay time implies poorer timing resolution of the detector. The light yield is the amount of scintillation photons emitted per deposited energy, typically expressed in photons/MeV. A bigger number of photons implies better statistics and therefore better energy resolution. Unfortunately, fast response is usually related with a low light yield, so that a compromise between these two parameters has to be reached. *Table 2.2* presents some of the most common scintillators in PET detectors and their key properties. Most used scintillators nowadays are BGO and LSO. As we can observe in the table, LSO has higher light yield and lower decay time. This will provide better energy and timing resolution, being the common choice nowadays. Furthermore, we can observe that $LaBr_3$ and LuAP have excellent properties, but their high cost prevents their integration in commercial systems. In the case of CsI(Tl), it has the higher light yield, delivering excellent energy resolution, but its high attenuation length makes it deliver a very poor sensitivity and spatial resolution.

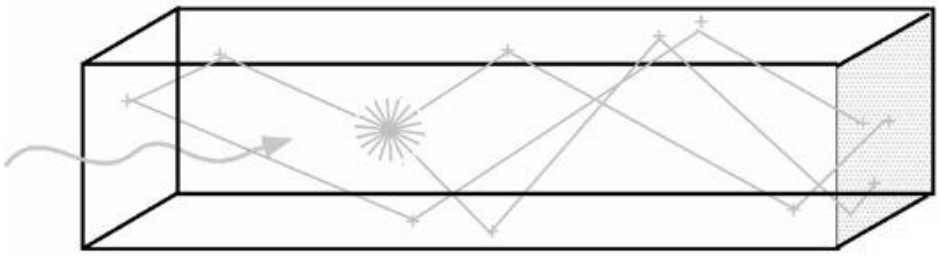

Figure 2.5: When an annihilation photon enters the crystal, it interacts producing multiple scintillation photons, which are emitted in all the directions. The photons are likely to be reflected in the crystal interfaces until they are collected by the photodetector.

Crystal	Composition	Density (g/cm3)	Zeff	Att. lenght for 511keV (mm)	Probability of PE (%)	Light Yield (ph/MeV)	Decay Time (ns)
BGO	$Bi_4Ge_3O_{12}$	7.10	75	10.4	35	9000	300
LSO	Lu_2SiO_5:Ce	7.40	66	11.4	32	30000	40
Na(Tl)	Na(Tl)	3.67	51	29.1	17	41000	230
CsI(Tl)	CsI(Tl)	4.51	52	22.9	21	85000	600
GSO	Gd_2SiO_5:Ce	6.70	59	14.1	25	12500	60
LuAP	LuAlO3:Ce	8.34	65	10.5	30	11400	18
$LaBr_3$	$LaBr_3$:Ce	5.29	47	10.4	13	70000	17

Table 2.2: Most relevant scintillators for PET and their properties.

2.2.1.2 Photodetectors

Photodetectors are used in PET for the translation of the scintillator photons into an electrical signal. The used photodetector will depend on the application, taking into account properties as the *gain* or the quantum efficiency (QE). We define as QE the ratio of charge generated per incident photon in the photo-sensible area. Other properties as temperature sensitivity or magnetic field sensitivity might be also taken into account for certain applications. High QE and gain of the photodetector will improve the performance of the PET System. *Table 2.3*, compares three types of photodetectors typically used for PET.

Photodetector	Gain	Rise time (ns)	QE (%)	Temperature Sensitivity (%/°C)	Magnetic Field Sensitivity	Typical Size
Photomultiplier (PMT)	10^6	1	25	1	yes	cm^2
Avalanche photodiode	10^3	5	70	3	no	mm^2
Silicion PMT	10^6	1	50	5	no	mm^2

Table 2.3: Most relevant photodetectors for PET and their properties.

The photomultiplier tube (PMT) is the most common photo-detector type for scintillator readout in PET. Its high gain combined with a low noise factor lead to minimal deviation from Poisson statistics as well as reduced statistical uncertainty in the generated charge signal (Spanoudaki & Levin, 2010). A PMT is a vacuum tube consisting of a photo-cathode, several electrodes called dynodes and an anode. The photocathode is a photosensitive electrode that emits charge (electrons) when scintillation photons reach the surface. Between the cathode and the anode, a bias voltage is applied to transport and amplify the electric current. Under the influence of a high potential the generated electrons from the photocathode drift and successively encounter the dynodes. At every dynode stage, the incident electrons have gained sufficient energy to create secondary electron emissions from collisions with the dynode, thus resulting in a large electron cloud at the anode and high gain. The main drawbacks of PMTs are their low QE around 25% and their large size, which make it difficult to couple them to very small detector crystals. A diagram representing the basic operation of PMTs is shown in *Figure 2.6*.

Avalanche Photo-Diodes (APDs) are based on the activation of PIN diodes (diodes with a wide undoped intrinsic semiconductor region between the p-type and n-type semiconductor regions) due to the interaction with the arriving scintillation photons. This interaction is much more likely than the appearance of a photoelectron on the photocathode of a PMT, providing a higher QE. Nevertheless, their gain is orders of magnitude lower and dependent of the temperature, which degrades energy resolution. Nowadays, installation of APDs is reserved to special situations, as in PET/MR hybrid systems.

Recently, ***Silicon Photomultipliers (SiPMs)*** have been introduced to address the different limitations of both PMTs and APDs. These devices are arrays of APDs that work on Geiger mode. In this mode of operation, the interaction of a photon results in a cumulative avalanche breakdown within the diode depletion region, improving the gain of the photodetector. SiPMs provide high gain and quantum efficiency and small size and

they are not sensible to magnetic fields, which delivers good spatial, energy and timing resolution. SiPMs are currently replacing the usage of PMTs and APDs in system development. The first commercial system introducing this technology, the Vereos PET/CT (Koninklijke Philips NV, Netherlands), was presented on 2014.

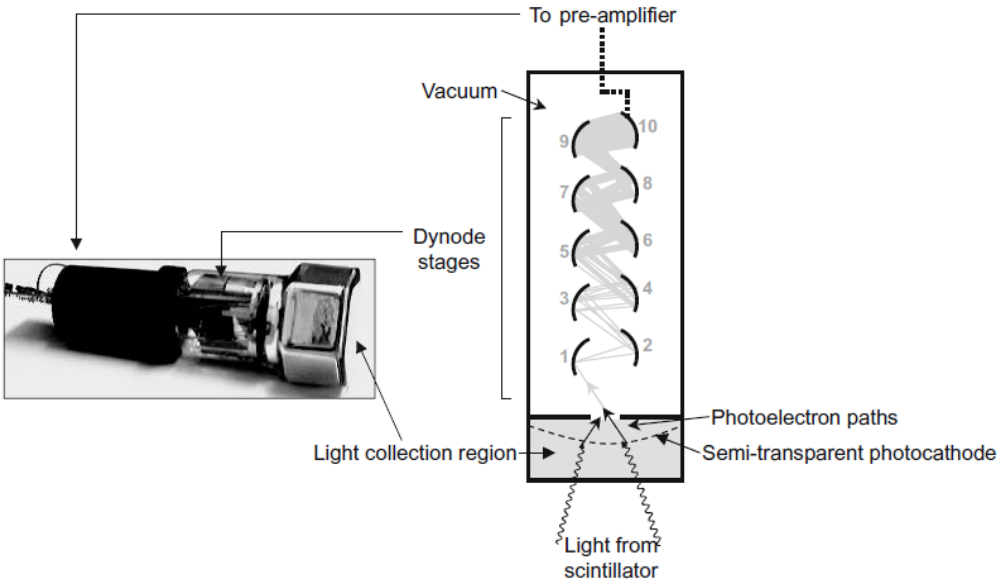

Figure 2.6: Diagram and basic operation of a PMT. Reproduced from (Bailey et al., 2005).

2.2.1.3 Detector arrangements

Scintillator crystals and photodetectors can be coupled in different arrangements. Most simple and intuitive is the ***one-to-one coupling***, where each crystal is coupled to its own photodetector. This approach has several drawbacks. On this configuration, the spatial resolution is determined mainly by the size of the photodetector, and PMTs, the most common photodetectors in PET instrumentation, are usually several centimetres wide. The problem can be solved by the use of Position-Sensitive PMTs (PS-PMTs), multichannel PMTs with arrays of small dynodes coupled to multi-anode structures, which essentially divide single PTMs into very small channels that can be coupled to individual crystals. Despite the very good spatial and timing resolution achieved by these configurations, the use of very small crystals with one-to-one coupling will generate an electric signal per crystal. Taking into account that a clinical PET system has thousands of crystals, the processing of all these signals would be very complex and expensive.

Anger coupling is defined as the configuration where a large continuous crystal is coupled to an array of PMTs. The light will spread in the crystal after the interaction, and each of the PMTs will receive a signal proportional to its position related to the interaction. A weighted centroid-positioning algorithm is used for estimation of the interaction position within the detector from the signals received by each PMT. Since these detectors involve significant light sharing between PMTs, a high light yield scintillator is needed for having enough statistics. Nevertheless, the main problem of this approach is the use of very wide crystals in PET imaging (typically 15-25 mm), which implies very complex light spread, especially in the crystal interface. Furthermore, the spread of scintillation light within the crystal leads to significant detector dead time at

high-count rates. Due to these limitations, Anger coupling is not used on current commercial systems.

The usually chosen hybrid solution is using ***block detectors*** *(Figure 2.7).* In block detectors, individual small crystals are coupled to the PMTs through a light guide. The light guide will spread the light from the individual crystal to the PMTs, reducing the spread of photons generated on the continuous crystal. A modified Anger logic is then used to calculate interaction point based on the signal of each PMT. This solution reduces the light spread, improving time response of the detector while reasonably maintaining spatial resolution. It is the most used solution on commercial PET systems.

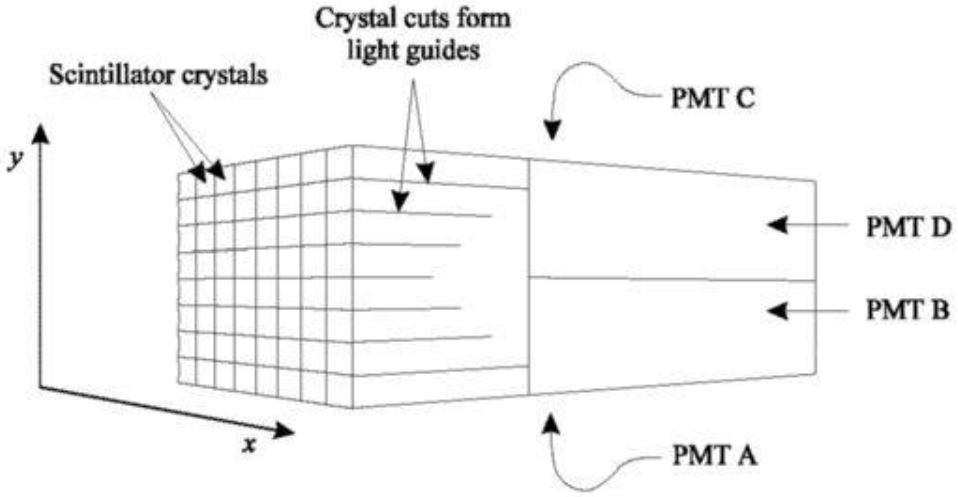

Figure 2.7: Example of a block detector. The 'block detector' uses four PMTs (PMT A-D) to decode an array of crystals with various combinations of reflectors and surface treatments between the crystals.

2.2.1.4 Electronics

When a photon hits the detector, the PMT emits a charge pulse proportional to the energy deposited on the detector. This pulse is sent to the electronics module, usually a pulse height analyser (PHA) to generate timing, energy and position information. Typically, the pulse is filtered to remove high frequency noise and converted to a digital signal. The PHA takes photons of a selected energy window and rejects the rest. If a narrow window is used, the energy discrimination is precise (small number of scattered photons) but the detection efficiency is low (also small number of unscattered photons) (Bailey et al., 2005). In the case of PET systems, the PHA window is centered on 511 keV, typically between 350 and 650 keV for BGO (Saha, 2010). Coincidence logic is used to discriminate if two detected photons are coming from the same annihilation. This discrimination process is known as "electronic collimation". Usually, the PHA attaches a digital time stamp to every photon. The coincidence module then compares the events from each detector with the ones recorded in opposing detectors. A coincidence event is assumed to have occurred when a pair of events are recorded within a specified coincidence timing window, which typically of the order of magnitude of 10 nanoseconds (Cherry et al., 2012).

2.2.1.5 PET detector characterization

The design of the individual detector block will determine the whole performance of the scanner. Several properties are used in order to characterize the performance of a detector block.

We define ***timing resolution*** as the uncertainty in the detector timing on an event-by-event basis due to statistical fluctuations. The timing resolution is important since PET events involve the detection of two photons coming from the same annihilation (Cherry et al., 2012). When a photon is detected, the scanner electronics generate a narrow time window, and if other photon reaches the scanner within this time window, it is considered to come from the same positron annihilation. If the timing of the detectors is poor, the coincidence window needs to be wider. The timing resolution is dominated by the scintillator properties so that the faster the decay time of the crystal, the better the timing resolution. For this reason, scintillators as $LaBr_3$ or LSO provide good timing resolution. Furthermore, Anger arrangements involve a high spread of scintillation photons (it involves multiple interactions of each scintillation photon before being detected in the PMT), which will lead to longer decay times and thus worse timing resolution (Bailey et al., 2005).

The ***energy resolution*** of a detector is defined as its ability to determine the energy of an incident photon. The energy resolution is directly related with two main factors that essentially improve the statistics of the measurement, the crystal light yield and the photodetector gain. Na(Tl) and Cs(Tl) provide high light yields and excellent energy resolution, but they are combined with very poor timing resolutions. $LaBr_3$ has excellent energy resolution, but at very high cost. LSO provide good energy and timing resolution at a reasonable price. About the photodetectors, PMTs offer the better energy resolution due to their very high gain (Lecoq, 2016).

The ***intrinsic sensitivity*** of a PET detector is its ability to detect a photon that reaches the crystal sensible volume. Sensitivity is determined by the stopping power of the scintillator for 511 keV. The sensitivity of PET scanners increases as the square of the detector efficiency, which is dependent of the scintillator decay time and stopping power. This is why LSO, LYSO and GSO detectors are preferred to NaI(Tl) or BGO detectors (Saha, 2010).

2.2.2 PET scanners

PET scanners are arrangements of block detectors, typically axially fixed full or partial rings with diameters around 80 cm, as shown by *Figure 2.8*. The selected arrangement will determine the geometric efficiency of the PET scanner, defined by the solid angle projected by the source of activity at the detector, and dependent on the distance between the source and the detector and on the diameter of the ring and the number of rings on the detector (Saha, 2010). This angle is usually narrow, and the scanner covers a small area of the body. To solve this, scanners are equipped with movable beds so the patient can be placed at different axial positions for whole-body scans (Cherry et al., 2012).

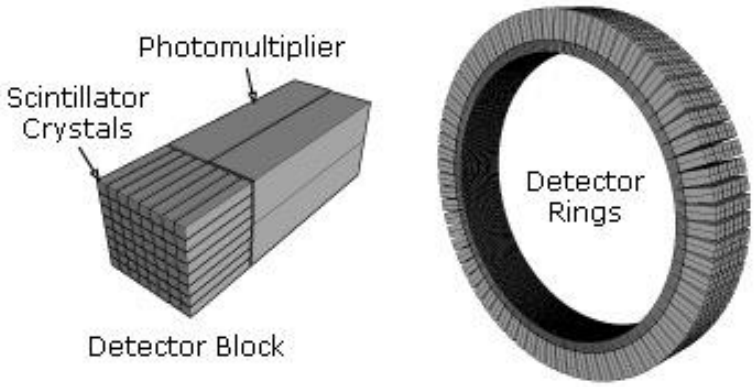

Figure 2.8: PET scanner formed by four rings of block detectors. Licensed under Public Domain via Commons.

2.2.2.1 Event detection in PET

PET scanner operation relies on the detection of coincident photons which are assumed to come from the same positron annihilation. The line between the arrival detector positions of the two photons constitutes a line-of-response (LOR), and identifies the line where the positron annihilated. Large numbers of these LORs are processed to generate images of the volumetric distribution of the radiotracer within the body. An event is considered a coincidence if it fulfils a couple of criteria. First, they should be detected within a predefined time window that is determined by the detector timing response. Second, both photons have deposited a certain amount of energy in the detectors within a range of energies known as the energy window. Due to the finite energy and timing resolution of PET detectors, undesired coincidences are generated in the normal operation of PET scanners. We can describe five different types of events in PET, named as trues, multiples, singles, scattered events and random coincidences (Abushab, 2013). Examples of the five types of events are shown in *Figure 2.9*.

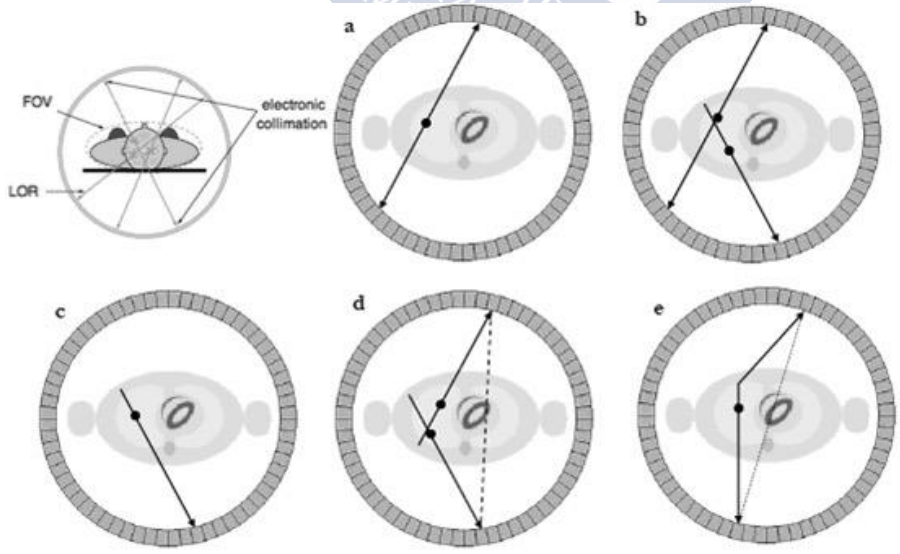

Figure 2.9: Examples of true (a), multiple (b), single (c), random (d) and scattered coincidences (e). Reproduced from (Abushab, 2013)

We consider a coincidence event a ***true event*** (a) when the scanner detectors detect photons from an original annihilation without having any additional interactions. In this case, the LOR is correctly assigned to the event.

Multiple coincidences (b) are produced when three or more photons are detected in coincidence, not knowing which of them represent a true coincidence. These events are usually discarded in PET acquisitions.

Single events (c) are produced when only one of the photons coming from annihilation is detected. These events are usually discarded, and they are by far the most common type of event found in PET acquisitions.

A ***scattered coincidence*** (d) occurs when one of the photons has passed through a Compton interaction that has deflected its trajectory. If the photon and the coincident photon are detected, and the energy resolution is not good enough to reject the scattered photon, an incorrect LOR will be assigned to the event.

A ***random coincidence*** (e) is recorded when two photons coming from different annihilations are detected into the same coincidence window. Randoms are introduced on the final image as a constant background. The random event count rate between a pair of detectors *"a"* and *"b"* can be calculated as $R_{ab} = 2\tau N_a N_b$, where 2τ is the time window and N_a and N_b are the number of single photons detected by detectors *"a"* and *"b"* within a time window. As the formula is proportional to the time window, improving the timing resolution by choosing a faster scintillator can reduce the number of random events.

Both multiple and singles events can be easily removed from the acquired data. By contrast, scatter and random coincidences consist on the detection of two photons and therefore they are recorded as valid coincidences. Ideally, only trues should be recorded, and in order to obtain optimal image quality, scattered and random coincidences should be removed by applying proper corrections, which will be discussed in upcoming sections.

2.2.2.2 The sinogram

PET data is stored as LOR histograms, which represent the number of coincidences, detected by each LOR. These data carry the useful information required for obtaining the original three-dimensional distribution of the radiotracer, and they are usually stored as a set of two-dimensional images called sinograms (Aguiar, 2010). A sinogram is a representation of the signal measured at a given angle in the imaging plane at varying distances along the detector array. An example is shown in *Figure 2.10*.

Given different LORs labeled as *A,* B, C, D, they can be completely characterized by the angle of orientation ($\emptyset$) of the LOR (0º for the case of LOR *A)* and the shortest distance between the LOR and the center of the scanner (s). These two parameters $(s, \emptyset)$ can be represented as points in a two-dimensional space, as in *Figure 2.2.B.* In the final sinogram, the value in each pixel represents the number of coincidence detections between the detectors pair associated with that LOR. For a PET scanner with multiple rings, sinograms are stored as multiple slices (Fahey, 2002).

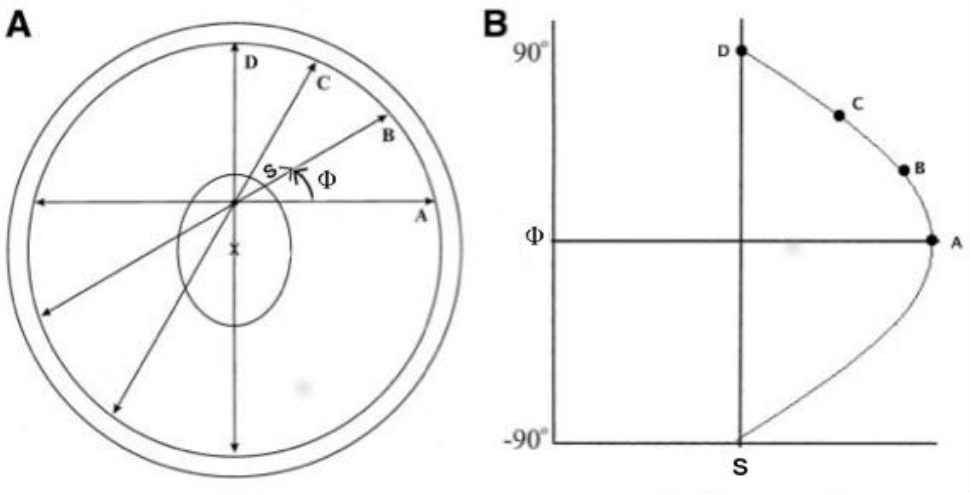

Figure 2.10: Example of PET acquisition and data storage. (A) example of PET acquisition, (B) Example of sinogram space. Image modified from (Fahey, 2002).

Instead of sinograms, PET data can also be stored as projections, which are sets of (s, z) data stored for each $(\emptyset)$ angle, as shown in *Figure 2.11*. Projections can be obtained from sinograms from reorienting the sinogram matrix. They are useful for visualization and for the implementation of certain reconstruction methods.

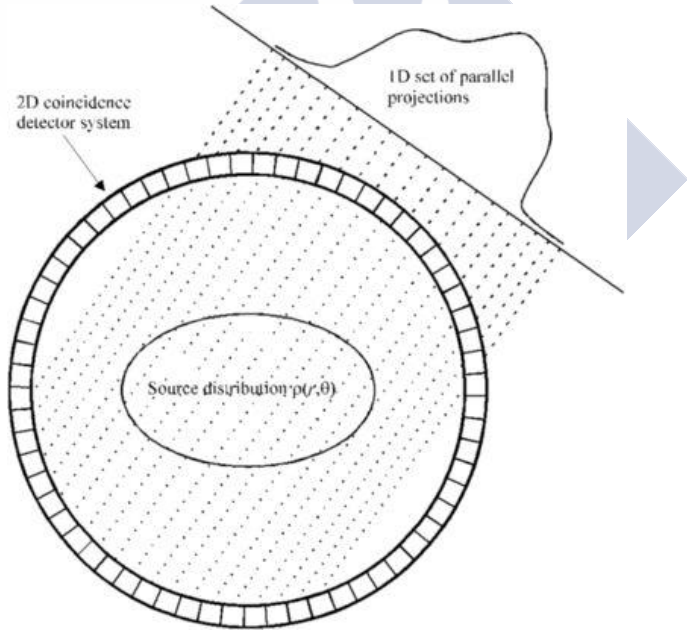

Figure 2.11: Projection data is stored as integrals of the activity for each *s* at a given angle. Extending the acquisition to all the z positions generates 2D projections. Figure is adapted from (Bailey et al., 2005)

2.2.2.3 Axial Sampling

A PET scanner includes several rings of detector crystals, arranged as shown in *Figure 2.12*, which defines the coordinate system of a PET scanner. A LOR can be labeled in the space as $L(s, \emptyset, \theta, z)$, where θ is the angle with the Z axis (axial angle) and z is the

position on the Z axis (axial position) and $(s, \emptyset)$ are the sinogram variables. We say that a PET scanner is operating in fully 2-dimensional mode (2D) when only coincidences between detectors on the same ring are accepted, which means that only $\theta = 0$ is accepted. On this mode, the geometrical sensitivity of the scanner is N times the sensitivity of a single ring, where N is simply the number of rings, and additional rings only serve to increase the coverage of the object, which is known as the axial FOV of the scanner. A scanner running in 2D mode will store data on N sinograms, one for each ring. In 2D acquisition mode, the rings are usually separated with physical septa, in order to minimize interactions between the detectors and scattered and random coincidences. In order to improve sensitivity, 2D acquisition modes usually include this "direct" sinograms and interplanes formed between rings with a ring difference of ± 1. The planes with ring difference of ± 1 are considered physically between detector rings (Bailey et al., 2005). This results on a total of $2N - 1$ (N direct sinograms and $N - 1$ interplanes).

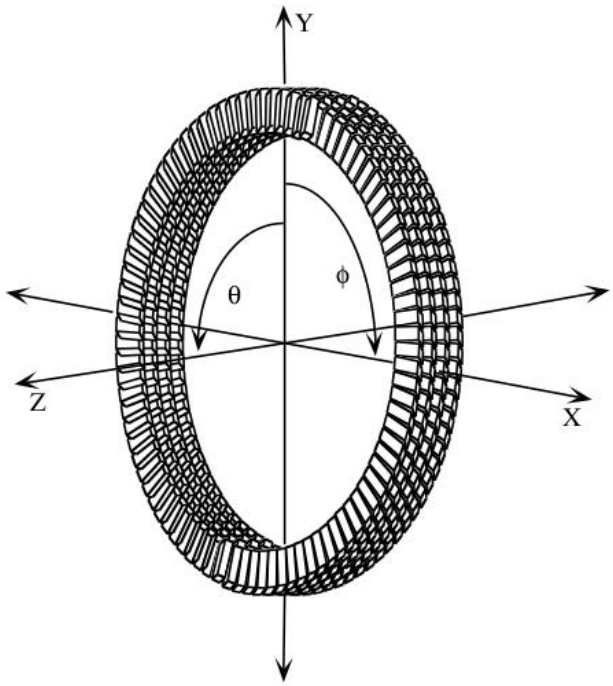

Figure 2.12: Diagram and coordinate system of a PET scanner of several rings. Figure reproduced from (Bailey et al., 2005)

In state-of-the-art scanners, the acquisition is usually performed in fully 3D-mode, where coincidences between any different rings are accepted. 3D acquisition was discarded for a long time due to the lack of efficient 3D reconstruction algorithms and scatter correction methods. The 3D acquisition will generate N^2 sinograms, one for each combination of detectors, drastically improving the sensitivity of the scanner. It has to be pointed that in 2D and 3D modes many coincidences are redundant, since the image can be reconstructed using only 2D data, but they help to increase sensitivity and thus to reduce noise. Nevertheless, the acceptance of all coincidences will degrade the image quality by including more scattered and random coincidences. We can see examples of the different types of acquisition modes in *Figure 2.13*.

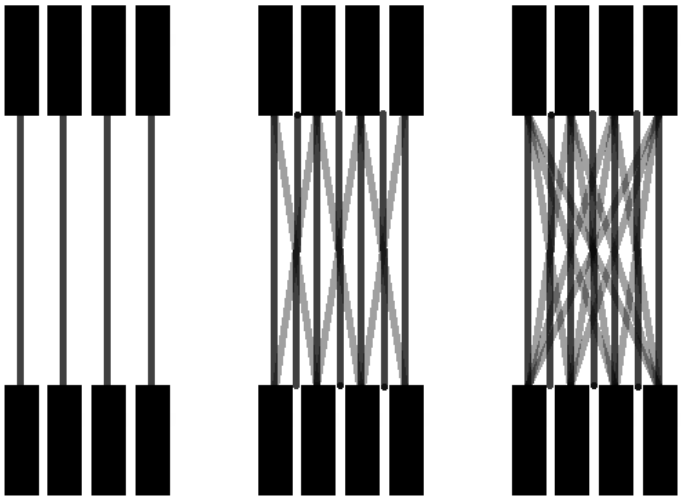

Figure 2.13: Example of accepted coincidences for fully 2D (left), 2D (center) and fully 3D (right) acquisition modes.

In 3D acquisition, sinograms between different rings are usually grouped to optimize the data storage and the reconstruction time. This process can be really confusing in modern scanners, which can have up to 64 rings. For having a convenient representation of the different possible acquisition modes in a PET scanner we use graphs known as "Michelograms". *Figure 2.14* shows an example of the different acquisition modes for a PET scanner with 8 rings. Each axis is numbered from 0 to 7 to represent the 8 rings. The point (0,0) represents the sinogram that includes coincidences within ring 0, the point (0,1) represents the sinogram that includes coincidences between ring 0 and ring 1, and so on. In the left, we can see that sinograms are stored for (0,0), (1,1), (2,2,). Which corresponds to the fully 2D acquisition mode with 8 sinograms. On the center of the image, we can observe a Michelogram where we have sinograms for ring differences of 0 and ± 1, and the line between ± 1 indicate that this sinograms are being added together. A set of sinograms with the same ring difference is called a segment. The addition is intended to reduce the number of sinograms. Span is a number that determines how much axial compression is used. The presented example corresponds to span 3; while no addition of sinograms corresponds to span 1. This corresponds to the 2D mode with 15 $(2N-1)$ sinograms in total. It has to be taken into account that sinograms with ring difference ± 1 that are added together will have approximately the double of counts that the ones with ring difference 0. In the right we can see the Michelogram for a fully 3D acquisition, where all the 64 sinograms are stored separately (span=1).

2.2.2.4 List mode acquisition

An alternative to sinogram storing is list mode acquisition. We define list mode as the storage of events in order of occurrence in the acquisition system. In list mode, each event is stored sequentially in a file containing the detection position of each photon, as well as the photon energiy and timing information. The main advantage of list mode compared to sinograms is that it allows the inclusion of external information such as gating parameters or patient motion records for further motion correction, or timing information in order to perform time-of-flight reconstruction. Furthermore, list mode

allows later binning into sinograms (Abushab, 2013; Nichols et al., 2002). In exchange, list-mode acquisition implies the creation, storage and management of very large files, which have created problems for high-end modern scanners with a very large amount of crystals.

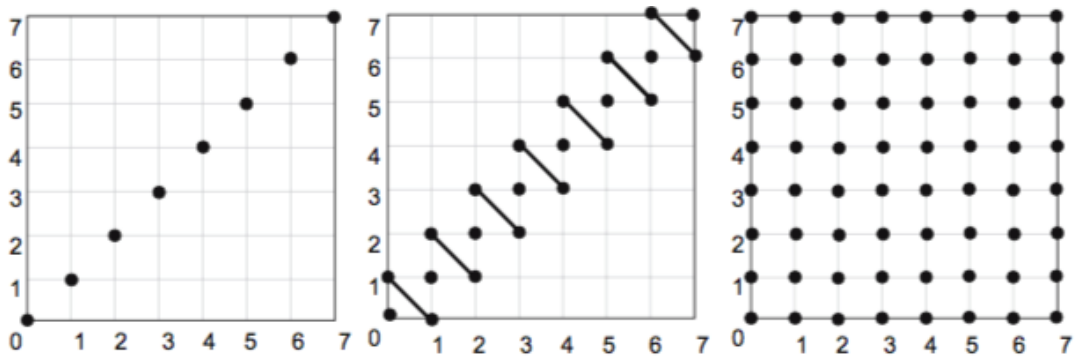

Figure 2.14: Different examples of Michelograms for fully 2D (left), conventional 2D (center) and fully 3D (right) acquisitions.

2.3 PET DATA CORRECTIONS

2.3.1 Attenuation Correction

As previously mentioned, photons can interact with matter by different processes, being Compton Effect the dominating mechanism for energy ranges of interest for PET. From a macroscopic point of view, the probabilities of interaction are given by attenuation coefficients μ/ρ expressed in units $cm^2 * g^{-1}$. For a well-collimated source and a detector, attenuation takes the form of an exponential $I = I_0 e^{-\mu x}$, where I is the intensity of the beam, I_0 is the initial intensity, x is the material thickness and μ is the linear attenuation coefficient $\mu(cm^{-1}) = \mu/\rho(\, cm^2 * g^{-1}) * \rho(g * cm^{-3})$. Attenuation coefficients and densities for different tissues and materials are shown in *Table2.4*. For a point of emission inside the body, the detected counts between two detectors are $C = C_0 * e^{-\mu D}$ where the number of photon pairs emitted through the LOR is C_0, D is the total thickness of tissue travelled by the photon pair and μ is the average linear attenuation coefficient (Bailey et al., 2005). The attenuation is independent of the point of emission and it is a characteristic of the LOR. Thus, attenuation sinograms can be directly acquired, for example by using an external transmission source, in order to perform the attenuation correction.

Material	Density (ρ) (g*cm^3)	μ (511keV) (cm^{-1})
Adipose tissue	0.95	0.090
Water	1.0	0.095
Lung	1.05	0.025
Muscle	1.05	0.101
Cortical bone	1.92	0.178
NaI(Tl)	3.67	0.340
BGO	7.13	0.95

Table 2.4: Densities and linear attenuation coefficients for different types of tissues and materials (Bailey et al., 2005).

2.3.1.1 Positron-emitting transmission sources

A common approach for measuring attenuation is using transmission measurements of positron emitters with very long half-life such as ^{68}Ge ($t_{1/2} = 270d$) (Bailey, 1998). A set of two or three thin rod sources are placed along the scanner gantry and rotated around the scanner, exposing detectors uniformly (See *Figure 2.15*). A transmission scan usually takes 10-30 minutes to acquire for whole-body imaging. An important limitation of this type of correction is the high noise of the acquired data, due to the low probability of a photon trespassing the whole body. Therefore, transmission measurements for attenuation are a major source of noise.

2.3.1.2 CT-based attenuation correction

With the emergence of multimodality PET/CT scanners in the last decade, new methods to use the CT transmission data for the correction of PET attenuation have been studied. CT data provides lower noise and better spatial resolution when compared with transmission data (Kinahan et al., 2003). Furthermore, the acquisition of the CT data is much faster, substantially increasing patient throughput. The main challenge is the calculation of 511 keV $\mu(cm^{-1})$ values from the low energy ones obtained with the CT and the translation from Hounsfield units acquired in CT to $\mu(cm^{-1})$ coefficients.

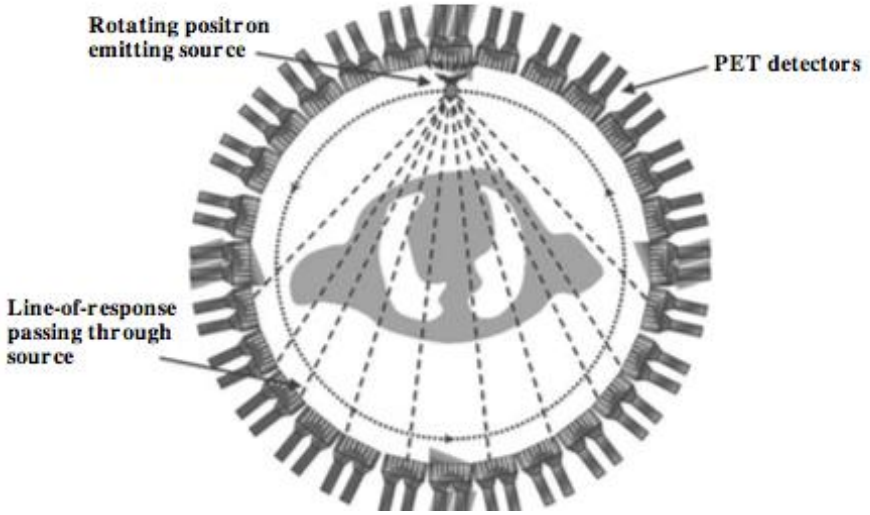

Figure 2.15: A rotating positron-emitting source is used for the acquisition of attenuation sinograms. In each position, LOR between the nearest detector and different opposed detectors are measured. (Bailey et al., 2005)

2.3.2 Scatter Correction

Due to the finite energy resolution of the PET detectors, certain scattered events are still accepted as valid coincidences by the scanner. Their fraction depends of several factors such as the size and geometry of the object (typically the patient), the geometry of the scanner, the energy window and the acquisition mode (2D or 3D). Scattered counts are a factor degrading the contrast of the final images, and several techniques have been developed in order to correct for scatter in PET. Since both scattered and true coincidence rates vary linearly with the administered activity, the scatter-to-true ratio does not change

with the injected activity. In 2D acquisition, the use of retractable septa removes most of the scatter, delivering scatter fractions around 10%, while in 3D mode the fraction can be as high as 30%-50% (Polycarpou et al., 2011). The scatter fraction and the absence of effective scatter correction methods was one of the factors preventing the implementation of 3D PET scanners. First scatter corrections were performed by assuming that the scatter fraction is uniform for all the FOV. Assuming this, the correction is made by taking the counts outside the object, where true coincidences are not expected. More sophisticated approaches are described below.

2.3.2.1 Multiple Energy Windows

This empirical approach exploits the fact that a great portion of scattered photons is in the single photon region of the spectrum below the photopeak. Thus, data recorded in energy windows set in this region can be used to estimate the scatter contribution to the photopeak. The dual energy window (DEW) method sets the window below the photopeak, and estimates the scattered events on the photopeak window using the amount of radiation on the lower window (see *Figure 2.16*) (Bailey et al., 2005). The DEW assumes that the spatial distribution of the scatter in the photopeak energy window is equivalent to that in a second energy window, which is not true. Scattered events, registered in the Compton window, are normalized and subtracted from the photopeak window (Castiglioni et al., 1999). The main drawback is that scatter measurements are noisy and should be smoothed in order to be subtracted from the photopeak data. Apart from the DEW, more complex methods using three (TEW) or more windows to obtain a more precise measurement of the scatter have been proposed.

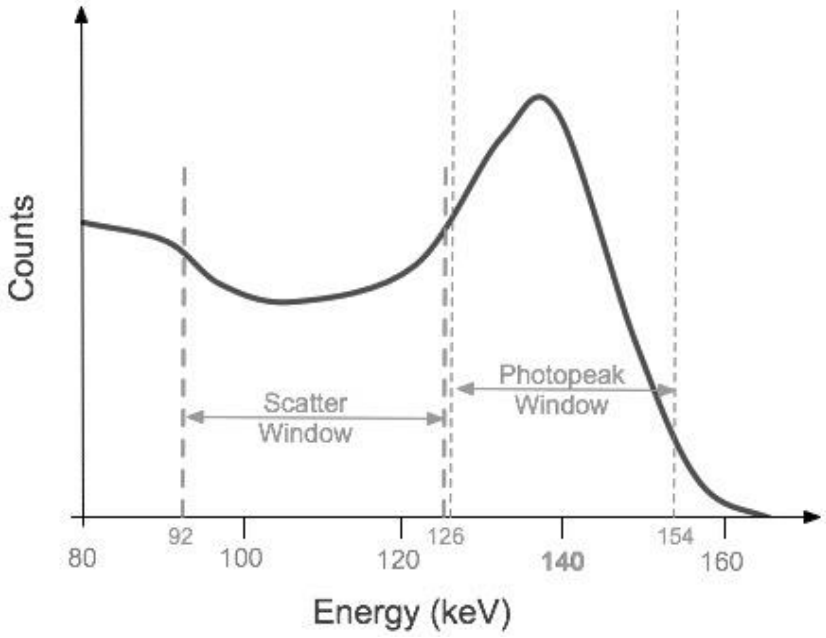

Figure 2.16: Window settings in the DEW scatter correction method. The "Main" window is centered on the photopeak; while the "Scatter" window is used to estimate the scatter contribution on the photopeak. Licensed under Public Domain via Commons.

2.3.2.2 Monte Carlo Simulations

Monte Carlo (MC) simulations allows scattered and true coincidences to be simulated and stored separately, so it is a powerful tool for correcting scatter. The method uses the reconstructed image as the input activity map and the measured CT as an attenuation map for a Monte Carlo simulation. It is assumed that the number of events in each pixel of the image represents the original isotope concentration without the scatter contribution. From the simulation, separated sinograms can be obtained for scattered and true coincidences. The calculated scatter contribution is then used to correct the original data set. (Levin et al., 1995). The method can be iteratively applied to reduce the error produced when assuming no scatter on the original distribution. Monte Carlo simulation is one of the most accurate correction methods for scattered counts. Nevertheless, the long time required to perform simulations with enough statistics to obtain a reliable correction makes it unviable in the clinical routine.

2.3.2.3 Single Scatter Simulation (SSS)

The Single Scatter Simulation technique (SSS) is an intermediate approach that approximates the scatter on a given LOR by estimating only the single scatter component (Watson et al., 1996; Ollinger & Johns, 1993). This method exploits the fact that the contribution of a small scattering region of the object to a LOR can be analytically calculated by the Klein-Nishima equation, and thus the total amount of single scatter can be calculated as the sum of the contributions of many of this regions, which are named scatter points on the bibliography (Werling et al., 2002). The main shortcut of this approach is that the contributions are calculated with non-corrected data, so an overestimation of the scatter distribution is expected. In order to solve this problem, the SSS is applied iteratively inside the reconstruction (Brix et al., 1997).

2.3.3 Randoms Corrections

A random event occurs when the photons coming from different annihilations hit the detector during the same time window and they are interpreted as a coincidence. Random coincidences are extremely important on modern PET systems, where 3D acquisition has significantly increased the sensitivity of the acquisition. In order to achieve absolute quantification, it is important to estimate and subtract random coincidences (Brasse et al., 2005). Different correction methods can be used.

2.3.3.1 Tail Fitting

Random coincidences are supposed to be approximately constant through the FOV of the scanner. Due to this, it is possible to estimate the number of randoms inside the object by fitting the tails outside the body to a Gaussian with a constant background. This background will give us an estimate of the ratio of random counts that can be subtracted to the measured counts for each LOR. This method requires that the object does not cover all the field of view, so the tails and background can be adequately fitted.

2.3.3.2 Estimation from singles

As mentioned in previous sections, the number of random coincidences can be estimated as $R_{ab} = 2\tau N_a N_b$, where 2τ is the time window and N_a and N_b are the number of single photons detected by detectors *"a"* and *"b"* within a time window. As N_a and N_b can be measured, R_{ab} can be calculated for each LOR and subtracted from the measured data (Cooke et al., 1984). This method has the advantage that the measure is performed measuring singles, which usually have very high statistics. Nevertheless, measuring and storing single rates is very inefficient and the method does not take into account the electronics dead-time arising from the coincidence processing circuitry, which may be an important factor in high sensitivity systems.

2.3.3.3 Delayed Coincidence Channel

In the "delayed coincidence channel (DCC)" method, the timestamp of one of the recorded coincidence photons is intentionally delayed, so only random coincidences are produced. This random coincidence sinogram is a good estimate of the random ratio, and can be subtracted from the original sinograms (Brasse et al., 2005). The advantage of this method is that the delayed channel has identical dead-time properties to the prompt channel. The disadvantage is that the statistical quality of the randoms estimate is poorer than in the previous method. Current DCC methods perform separate acquisitions for the prompt and the delayed coincidence windows. Using this approach, randoms estimated sinograms could be post-processed in order to reduce the noise before subtracting them from the sinograms. The only significant drawback of this method (compared to direct subtraction of the delayed channel data) is that acquiring a separate randoms sinogram doubles the size of the dataset. This can be a particular problem for fast dynamic scanning in 3D mode, where sorter memory and data transfer time can be a limiting factor.

2.3.4 Data Normalization

Conventional PET reconstruction algorithms usually assume that all the LOR have the same sensitivity. Nevertheless, this is not true since LOR sensitivities can be affected by a number of different factors such as non-uniform PMT gain, variations due to the geometry of the scanner and physical variations of the detectors, resulting in non-uniformity of the acquired data even when using uniform sources (Defrise et al., 1991). Due to this, information on the variations on sensitivity for each LOR is required for achieving quantitatively reliable images. The first of them is the angle of the LOR. Only in LORs passing through the center of the FOV are perpendicular to the detector face. For the rest, the LOR and the detector surface form a different angle, and the effective area of the detector is reduced, which also reduces sensitivity (Bailey et al., 2005). This phenomenon can be observed in *Figure 2.17*. Additionally, in a block detector system each detector element will have different efficiencies due physical variations on crystal or PMT gains. The process of correcting for these effects is called normalization, and the individual correction factors for each LOR are referred to as normalization coefficients (NCs).

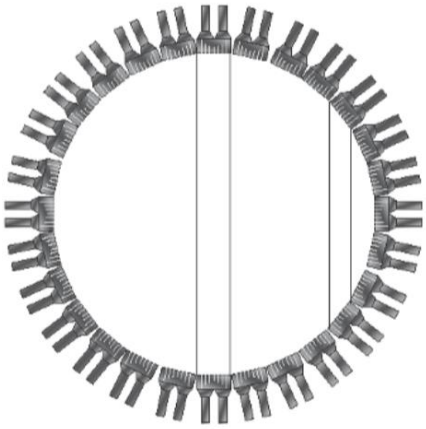

Figure 2.17: Reduction of the effective detector surface when moving away from the center of the field of view along the same ring. Figure reproduced from (Bailey et al., 2005).

Direct normalization is the simpler method for normalization correction. All detector pairs are exposed to a 511keV photon source, typically ^{68}Ge, without any source in the field of view, which is known as a blank scan. NCs are calculated for each pair of detectors by dividing the counts for the LOR joining the two detectors by the average counts of all LORs (Zanzonico, 2008). Afterwards, the emission sinograms are divided by the calculated normalization sinograms for normalizing the PET data.

2.3.5 Dead time correction

A PET scanner cannot register an infinite coincidence events rate. When a coincidence is produced, the scanner needs a certain time to be in good conditions to acquire the subsequent event. Usually, the most important factor affecting the minimum time between two separable events is the integration time, which is the time used to integrate the charge arriving on the PMT from the scintillator crystal. If a new photon hits the detector while the charge is being integrated, both events will be considered as a single one, resulting in a pulse pile-up effect (Vicente et al., 2013). In this case, either both events are considered one with different energy and position, or more likely, they will be discarded due to the upper energy threshold.

Coincidence processing also takes time, during which no further coincidences are accepted. There is also a chance that two true events occur during the same coincidence window. This is known as a multiple coincidence and both events are rejected. This can be especially problematic in modern scanners, where signals are multiplexed to reduce the amount of used coincidence circuitry. This shared circuitry processes many data, and it is an important contribution to the whole system dead time (Bailey et al., 2005).

For measuring the dead time of a PET scanner, a simple experiment is usually performed. A uniform cylindrical source with very high activity concentration is placed on the center of the FOV of the scanner. Consecutive acquisitions for singles, prompts and randoms are performed while the activity in the field of view decays. After several half-lives, the activity should be very small and the effects of dead time should be negligible. The incident count- rate for a given level of activity in the FOV is obtained by

linear extrapolation and is compared with the measured activity for that level, estimating the dead-time contribution (see *Figure 2.18*).

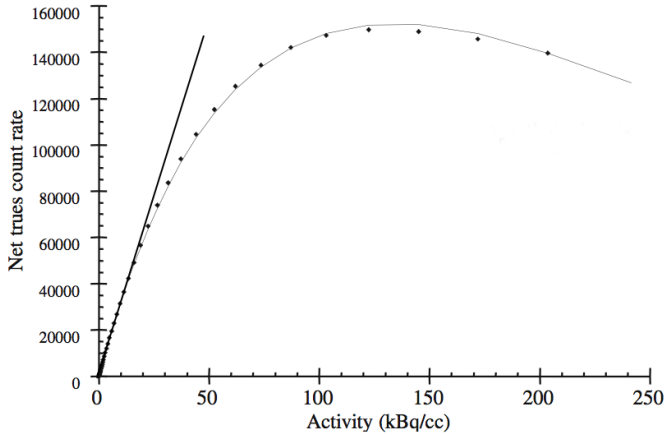

Figure 2.18: The trues count rate is not proportional to the activity in the FOV due to dead time of the scanner. The net activity can be calculated from a linear extrapolation (straight line) for activities bellow saturation. Figure adapted from (Bailey et al., 2005).

An accurate correction of dead time is not easy. The simplest approach would be to use the data from uniform sources for calculating correcting factors for each activity, using a curve as the one shown in Figure 2.18. Nevertheless, this method does not take into account the possible variations due to the changing shape of the source. A more accurate methodology is modelling each part of the system, experimentally or analytically, and correcting for all the sources. Dead time models use two components of the dead time, "paralyzable" and "non-paralyzable".

Paralyzable dead time refers to the situation where the system is unable to process events for a fixed amount of time τ after each event, but the system is not dead. For example, after a photon hit, the detector needs a certain integration time to register that event but new photons can still be hitting the detector during this time. For a "paralyzable" case, the relation between the real (N_0) and measured event rate (N) follows the equation $N = N_0 e^{-n\tau}$, where τ is the deat time for processing a single event.

In a ***"non-paralyzable"*** scenario, the events arriving during this time are simply ignored. This is the case for the coincidence circuit. Events arriving while a coincidence is being processed are simply ignored. For a "non-paralyzable" case, the relationship between real (N_0) and measured event rate (N) follows the equation:

$$N = \frac{N_0}{1 - N_0\tau}$$

The two components can be present in the system in series and this has been shown to be the case for PET systems. Each of the PET sub-systems can have one of these or a mixed behaviour, which can be modelled and corrected jointly or separately.

2.4 PET PERFORMANCE MEASUREMENTS

Different parameters such as spatial resolution, statistical noise, scatter fraction, contrast or sensitivity are routinely assessed for both characterization and calibration of PET scanners. These parameters are usually dependent on each other, and getting to compromise solutions between them is one of the crucial tasks of scanner and protocol design (Saha, 2010). The evaluation of these parameters is usually performed by using the NEMA-NU 2007 guidelines (National Electrical Manufacturers Association, 2007) (International Atomic Energy Agency, 2009).

2.4.1 Sensitivity

The sensitivity of a PET scanner is defined as the number of counts per second detected by the device per unit of activity in the source, and it is usually expressed in $counts/s \cdot MBq$. The sensitivity depends on the geometry of the scanner, the efficiency of the crystal, the width of the energy window, and the dead time of the system (Saha, 2010). About the geometry, current PET scanners cover a small solid angle of the patient, which implies low sensitivity. Due to this, patient studies are long acquisitions including multiple bed positions. The axial FOV may be increased by incorporating additional rings of block detectors in order to increase the solid angle coverage and hence the overall sensitivity (Eriksson et al., 2006). The intrinsic detection efficiency is the probability that two coincident photons traversing the scintillator crystal deposit all their energy in the detector. This sensitivity is related to the scintillation material decay time, density, atomic number and thickness (Levin, 2008). Furthermore, the energy window and the system dead time also have an effect on the scanner sensitivity. A wider energy window will provide a better sensitivity while increasing the number of scatter events. Faster electronics will provide reduced dead time and thus higher sensitivity in high activities. Sensitivity of a single ring PET can be calculated as (Budinger, 1998):

$$S = 100\frac{A \cdot \varepsilon^2 \cdot e^{-\mu D}}{4\pi R^2}(cps/MBq)$$

where A is the area of the detector, ε is the intrinsic detection efficiency, μ is the linear attenuation coefficient at 511 keV, D is the thickness of the detector and R is the radius of the scanner. We can observe that the sensitivity increases with the square of the detector intrinsic efficiency ε, which depends on the scintillator crystal choice. The sensitivity of current PET scanners is around 0.2-0.5% for 2D acquisitions and 2-10% for 3D PET (Cherry et al., 2012).

To evaluate the sensitivity by the NEMA-NU 2-2007 protocols, a 700 mm long polyethylene tube with diameter of 3 mm filled with 4 MBq of ^{18}F and is subsequently covered by different widths of aluminium (2.5 mm, 5 mm, 7.5 mm, 10 mm, 12.5 mm) simulating an attenuation medium and acquired for 300s (see *Figure 2.20*). The measurements are repeated at positions (0, 0, 0) and (100 mm, 0, 0). The sensitivity is obtained by fitting to an exponential function the series of sensitivity values for different aluminium thicknesses (see *Figure 2.20*).

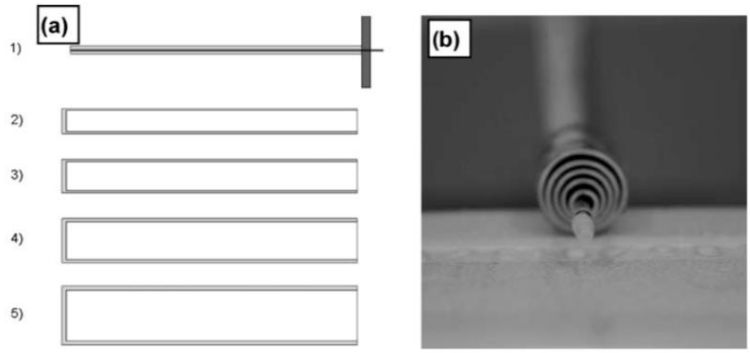

Figure 2.20: NEMA NU 2-2007 sensitivity phantom (a) diagram (b) phantom. Figure reproduced from (International Atomic Energy Agency, 2009), showing the different layers of aluminium surrounding the source.

2.4.2 Spatial Resolution

Spatial resolution is defined as the system ability to separate two points after image reconstruction and it determines the minimum size of a lesion or structure that can be detected. The main factors limiting spatial resolution in PET imaging are the crystal size (when segmented detectors are used), the positron range, the non-collinearity of the emitted photons and the tomographic reconstruction algorithm. The intrinsic resolution of the system is defined as *d/2*, where *d* is the width of the detector crystal element. As an example, for scanners with typical detector sizes around 5mm, the contribution of the crystal size to the final resolution is around 2.5mm. Furthermore, the position where the positron annihilates creating the two 511 keV photons is separated from the position of the parent nucleus by a distance known as positron range, generating some blurring on the final image. Positron range is relatively low for ^{18}F (0.54 mm), but it can be an important contribution for other radioisotopes such as ^{11}C (0.92 mm), ^{13}N (1.49 mm), ^{15}O (2.48 mm) or ^{68}Ga (2.83 mm) (Moses, 2011). Finally, as the positron has a certain kinetic energy when it annihilates, the two emitted photons are generally emitted with a small angle of around 0.2º between them. This angular uncertainty, known as the non-collinearity of the photons, causes a blurring on the final image proportional to the radius of the scanner (*R*), given by *0.0044R*. This value is around 2 mm for current scanners of 80-90 cm of diameter. The total resolution is calculated as:

$$R = \sqrt{(R_i^2 + R_p^2 + R_{nc}^2)}$$

where R_i is the intrinsic resolution of the detector, R_p is the contribution of the positron range and R_{nc} is the contribution of the non-collinearity. This theoretical value would result around 3.5 mm for actual scanners. It should be convolved with the degradation from the reconstruction process and additional small effects such as electronics decoding errors, detector penetration or limited sampling (Moses, 2011).

In order to evaluate the spatial resolution, the NEMA-NU 2-2007 suggest that a point source of 1x1x1 mm^3 of ^{18}F is placed on 4 different positions (0, 1 cm, 0), (0, 10 cm, 0), (0, 1 cm, (¼ FOV) cm), (0, 10 cm, (¼ FOV) cm) where the position (0,0,0) is the center of the field of view (FOV) of the scanner (see *Figure 2.19*). The activity of the point source should be low enough to keep the ratio of randoms to total events below 5%. The

obtained data should be rebinned using FORE and reconstructed using the 2D filtered backprojection (FBP) in a matrix of 1.0x1.0x1.0 mm^3 pixels. The obtained point-spread function (PSF) is fitted to a Gaussian distribution in order to obtain the spatial resolution in terms of Full Width Half Maximum (FWHM) and Full Width Tenth Maximum (FWTM) (Jakoby et al., 2011).

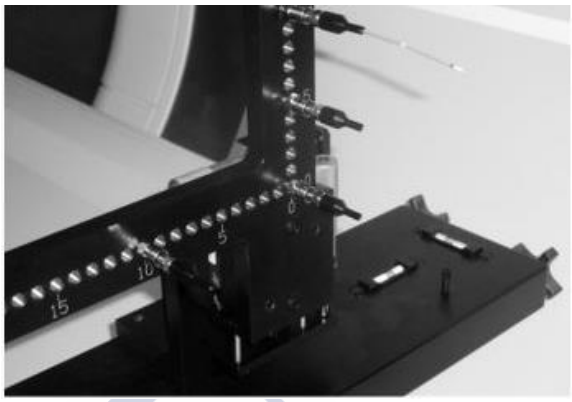

Figure 2.19: NEMA NU 2-2007 resolution measurement. Figure modified from (Martí-Climent et al., 2013).

2.4.3 Noise and scatter fraction

One of the main factors degrading PET images is the statistical noise, which is much more important in PET when compared to other modalities such as CT or MRI, and a good characterization of the noise levels is paramount for the characterization of a PET system. Unfortunately, a detailed description of the statistical noise affecting clinical PET images is not trivial, mainly because the noise distribution is altered by data corrections and image reconstruction, which may destroy the Poisson properties of PET imaging (Teymurazyan et al., 2013). Noise ratio is given by $\left(\frac{1}{\sqrt{N}}\right) * 100$, where N is the number of counts per pixel. Thus, noise can be reduced by increasing image acquisition statistics (N), which can be achieved by imaging for a longer time, increasing the dose injected to the patient or improving the scanner sensitivity (Saha, 2010). Furthermore, post-processing methods, mainly based on image smoothing, has also been used for improving noise properties while degrading other such as image resolution. In the NEMA protocols, the image noise in PET is characterized by a parameter named noise equivalent count ratio (NECR), which is defined as:

$$NECR = \frac{T^2}{T + S + R}$$

where *T* is the number of true coincidences, *S* is the number of scattered coincidences and *R* is the ratio of random coincidences. On the NEMA NU 2-2007 protocols, noise and scatter fraction are evaluated by measuring the NECR. This parameter is proportional to the signal-to-noise ratio (SNR) on the final image. The NECR estimates useful count rates of a scanner by taking into account the contribution of true events and of scattered events and randoms to the total coincidence rate (International Atomic Energy Agency, 2009). NECR is usually measured by making a long time measurement using a solid cylindrical polyethylene phantom with a line source radially offset from the centre (see

Figure 2.21). The radial displacement of the line source is expected to give a value for scatter fraction that is representative of a typical PET scan (Ferrero et al., 2011). At the start of the acquisition, with very high activity, T, S and R will have an important contribution. After the activity has decayed, the contribution of random coincidences will go down, allowing us to calculate the scatter contribution $S_F = S/T$. This fraction depends on multiple parameters, mainly the activity and attenuation distribution and the scanner geometry (Paans et al., 1989), and is a key factor for image quality.

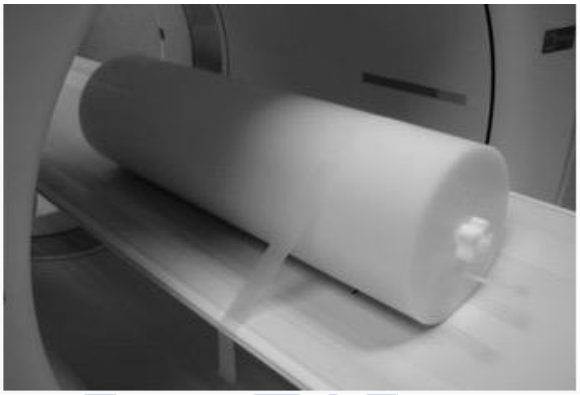

Figure 2.21: NEMA NU 2-2007 scatter phantom. The polyethylene cylinder is used to produce scatter in the activity coming from the inserted line source. Figure modified from (Martí-Climent et al., 2013).

2.4.4 Image quality

PET image quality is influenced by a number of different performance parameters, such as scanner sensitivity, uniformity, image contrast and spatial resolution, and by the performance of the reconstruction methods. Image quality is assessed in PET by calculating image contrast and background variability ratios for both hot and cold spheres. Contrast evaluates the variations in counts between adjacent areas in the image, and thus detectability of the lesions in the image. Image contrast also depends on the lesion size, especially when the size is similar to the scanner resolution, so different sizes of spheres can provide different contrast values. To take into account these different parameters, the NEMA IEC Body Phantom contains six coplanar methacrylate spheres with diameters of 10, 13, 17, 22, 28 and 37 mm and a polyethylene cylindrical insert of 50 mm of diameter (Jakoby et al., 2011). *Figure 2.22* shows the IEC Body Phantom.

Figure 2.22: NEMA NU 2-2007 image quality phantom.

3

Image reconstruction

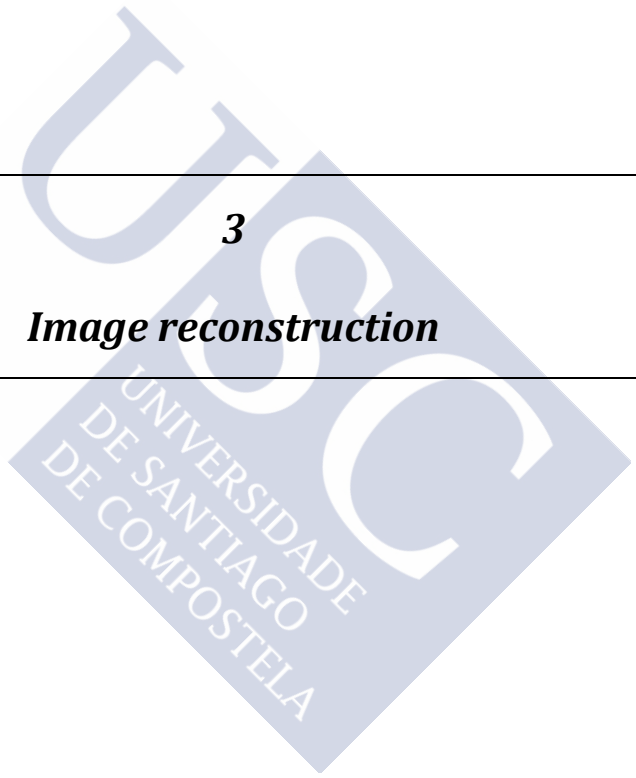

USC
UNIVERSIDADE
DE SANTIAGO
DE COMPOSTELA

3 IMAGE RECONSTRUCTION

PET reconstruction is defined as the recovery of the original radiotracer distribution from the sinograms or projections obtained in a PET acquisition. Due to the limited nature of PET in terms of statistics and resolution, numerous researchers have focused on improving PET reconstruction methods (Aguiar, 2010). This section is aimed at defining the reconstruction problem and presenting the most common reconstruction methods.

3.1 ANALYTICAL RECONSTRUCTION METHODS

The problem of image reconstruction can be formulated as a linear inverse problem:

$$s = Hf$$

where f is the radiotracer distribution, s are the measured data and H is known as the system response matrix (SRM). The reconstruction process consists essentially on inverting the SRM to obtain the radiotracer distribution f from the measured data s (Tong et al., 2010).

This formulation assumes that data are deterministic, which is not true, but is a simplification used by analytical image reconstruction methods. These methods attempt to find a mathematical solution based on the central section theorem. This theorem states that the projection data is the Fourier transform of the activity distribution:

$$P(v_s, \phi) = F(v_x, v_y)|_{v_x = v_r cos\phi, v_y = v_r sin\phi}$$

where $P(v_s, \phi)$ is the 1D Fourier transform of the projection $p(s, \phi)$:

$$P(v_s, \phi) = (\mathcal{F}p) = \int_{\mathbb{R}} ds\, p(s, \phi) \exp(-2\pi i s v)$$

and $F(v_x, v_y)$ is the 2D Fourier transform of the object distribution $f(x, y)$. Thus, the measurements in the projection space $\phi \in (0, \pi)$ allows the recovery of $F(v_x, v_y)$ for the whole frequency space $(v_x, v_y) \in \mathbb{R}^2$. Afterwards, the activity distribution $f(x, y)$ can be reconstructed by using the inverse Fourier transform, which is known as direct Fourier reconstruction (Bailey et al., 2005).

3.1.1 Filtered back-projection (FBP)

FBP is the most common analytical reconstruction algorithm for 2D-PET image reconstruction due to its low computational requirements and to its simplicity. The counts from each LOR are reprojected back into the image space placing a constant value into all the pixels along the LOR. Repeating this to all the LORs, a linear superposition of backprojections is obtained (*Figure 3.1*).

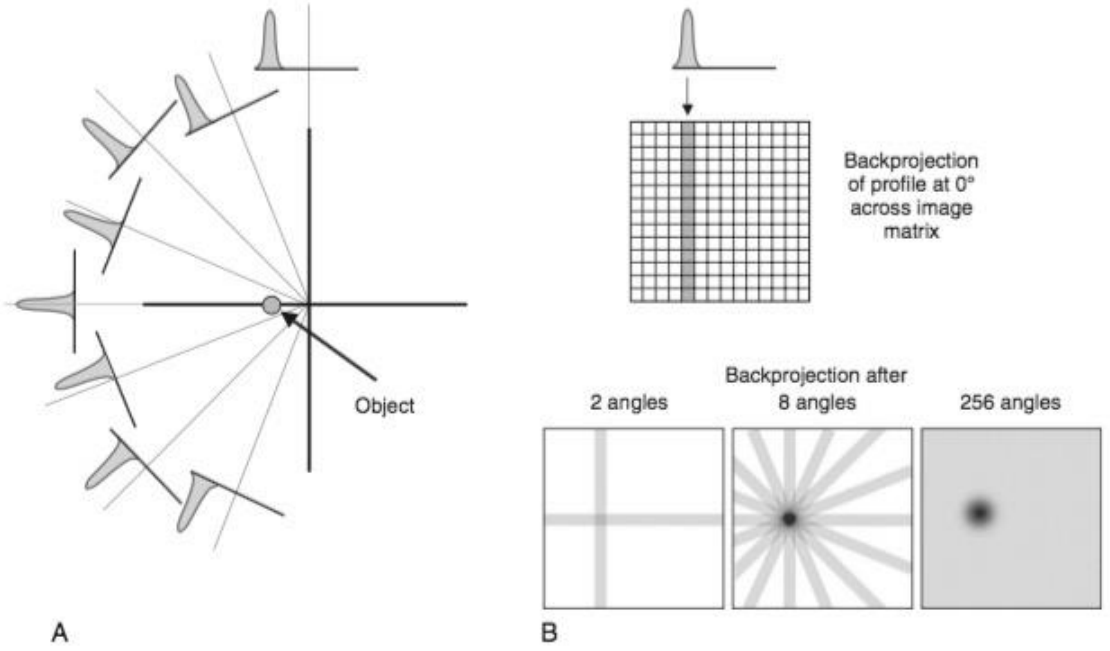

Figure 3.1: Illustration of the backprojection process. At left (A) we can observe the projections obtained for different angles for a very simple object. At right (B), a simple example of backprojection for 1, 2, 8 and 256 angles. Figure reproduced from (Cherry et al., 2012).

However, backprojected images are usually blurred due to the fact that counts are equally distributed along the LORs (Tong et al., 2010). This can be partially solved by filtering the data in the Fourier space, leading to a two-step inversion formula:

$$f(x,y) = (X^* p^F)(x,y) = \int_0^{\pi} d\phi \, p^F(s = xcos\phi + ysin\phi, \phi)$$

where p^F are the filtered projections:

$$p^F(s,\phi) = \int_{-R_F}^{R_F} ds' \, (p'(s',\phi) h(s-s')$$

and $h(s)$ is the ramp filter, which is the Fourier transform of the ramp function $|v|$. The objective of introducing the ramp filter is the recovery of high frequencies, which have been lost in the backprojection process:

$$h(s) = \int_{-\infty}^{+\infty} dv \; |v| 2\pi i s v$$

Of course, this formulation is an approximation based on continuous data, and some modifications are needed to apply FBP to discrete measured data $p(s,\phi)$. Several problems can occur due to the limited statistics of PET, since this is an ill-posed problem. This means that a minimum perturbation of $p(s,\phi)$ can produce a big error on the reconstructed image $f(x,y)$. This happens because the ramp filer amplifies high

frequencies present in the statistical noise distribution, which can be solved by the use of a low-pass window in the frequency domain. The most commonly used is the Hamming window (Baghaei et al., 2003). Image comparison between direct and filtered backprojection is shown in *Figure 3.2*.

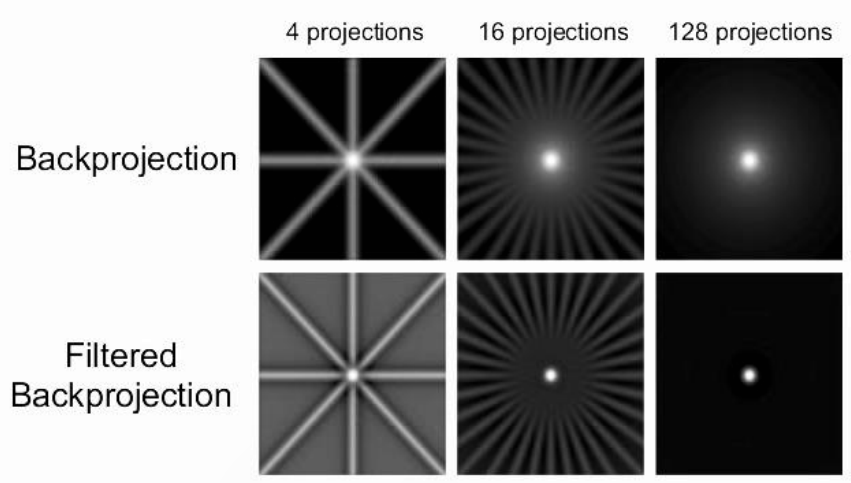

Figure 3.2: Comparison between direct and filtered backprojection for different numbers of projections/angles.

3.1.2 3DRP and Rebinning Algorithms

FBP is straightforward for 2D data, but its implementation for 3D data requires some modifications due to the limited axial extent of scanner (Baghaei et al., 2003), which truncates some of the projections depending on the object's position (see *Figure 3.3*). To solve the problem, 3D FBP algorithms reconstruct the image using the 2D algorithm first, and then use the reconstructed image to perform an analytical projection on 3D, filling the missing truncated projections. After that, the data can be reconstructed in 3D using combined measured and projected data. Another approach to reconstruct 3D data is to convert the 3D data into 2D sinograms that contain one sinogram for each axial position, and then use the 2D FBP algorithm for the reconstruction. These factoring methods are known as rebinning algorithms, being the simplest the single slice rebinning (SSRB), which assigns the sinograms between two different rings to a new sinogram lying between them in the axial direction (Daube-Witherspoon & Muehllehner, 1987). This approach is good for reduced and centered objects, but it produces large errors with radially extent objects. In multi-slice rebinning (MSRB), the oblique LORs are rebinned into different direct sinograms, improving the resolution while increasing noise (Lewitt et al., 1994). Further than this, the most extended algorithm is the Fourier rebinning (FORE), where the oblique LORs are rebinned using the frequency-distance information on the Fourier space (Alessio et al., 2006), and which is more accurate than the SSRB and MSRB. In FORE, the oblique rays are rebinned into 2D sinograms based on the frequency-distance relationship in the Fourier space (Defrise et al., 1997). The continuous Fourier transform of the sinogram $p_s(s, \phi, z, tan\theta)$ is calculated as:

$$P_s(w, k, z, tan\theta) = \int_0^{\pi} d\phi \; e^{-ik\phi} \int_{s_{min}}^{s_{max}} ds \; p_s(s, \phi, z, tan\theta) \; e^{-iws}$$

where w is the continuous spatial frequency of the Fourier transform, k the azimuthal Fourier index, and $z = \frac{z_A - z_B}{2}$ is the axial position of the new sinogram. The Fourier rebinning is based on the following approach:

$$P_s(w, k, z, 0) \approx P_s\left(w, k, z + k\frac{tan\theta}{2\pi w}, \theta\right)$$

which makes very easy to calculate $P_s(w, k, z, 0)$ from the measured oblique sinograms. Then, each generated sinogram P_s can be normalized for the contributions, which it has received, and the inverse Fourier transform can be used to obtain the rebinned data $p_s(s, \phi, z)$ (Bailey et al., 2005).

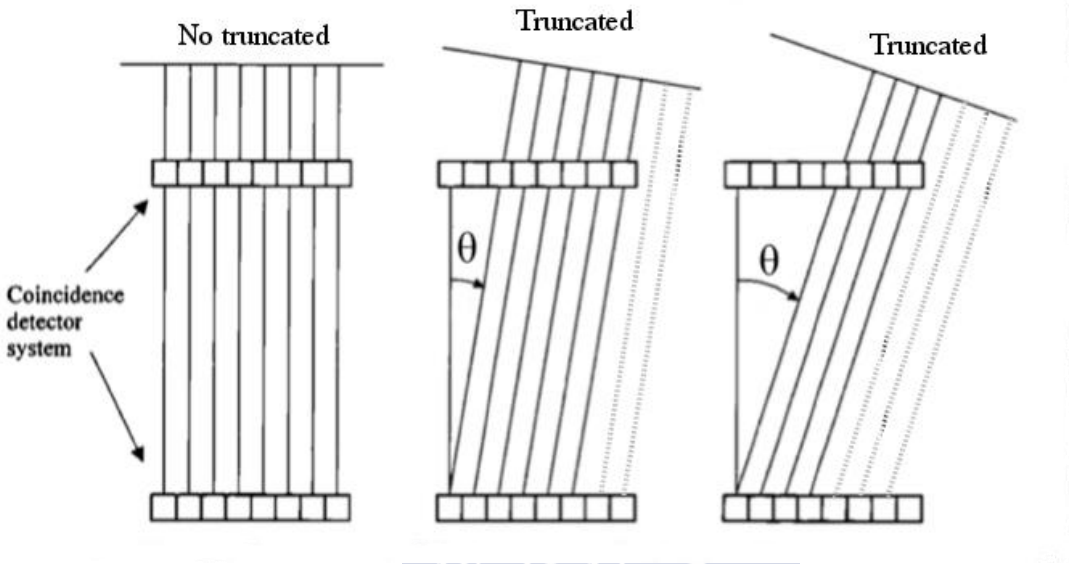

Figure 3.3: Axial view of a PET scanner. Extend of the different projections for different Θ angles. Figure adapted from (Badawi, 1998).

3.2 ITERATIVE RECONSTRUCTION

The analytic reconstruction algorithms are simple and predictable, but they assume that the measurements are noise-free, and statistical noise is a very important issue in PET imaging. Due to this, reconstructed images can be noisy, low-contrasted of and usually include artifacts, which degrades the image quality. These limitations boosted the development of iterative reconstruction algorithms based on statistical approaches. Iterative reconstruction starts with an estimate $f^0(x, y)$, which can be a simple shape as a cylinder. The estimate is forward-projected using the SRM of the scanner, and the calculated projections $p^0(r, \phi)$, are compared with the measured projections $p(r, \phi)$. The differences between $p^0(r, \phi)$ and $p(r, \phi)$ are used to modify the estimate $f^0(x, y)$ and generate a new estimate $f^1(x, y)$. This process is repeated until the difference between both sets of projections falls below a pre-set level (Cherry et al., 2012). *Figure 3.4* shows a schematic view of the iterative reconstruction process.

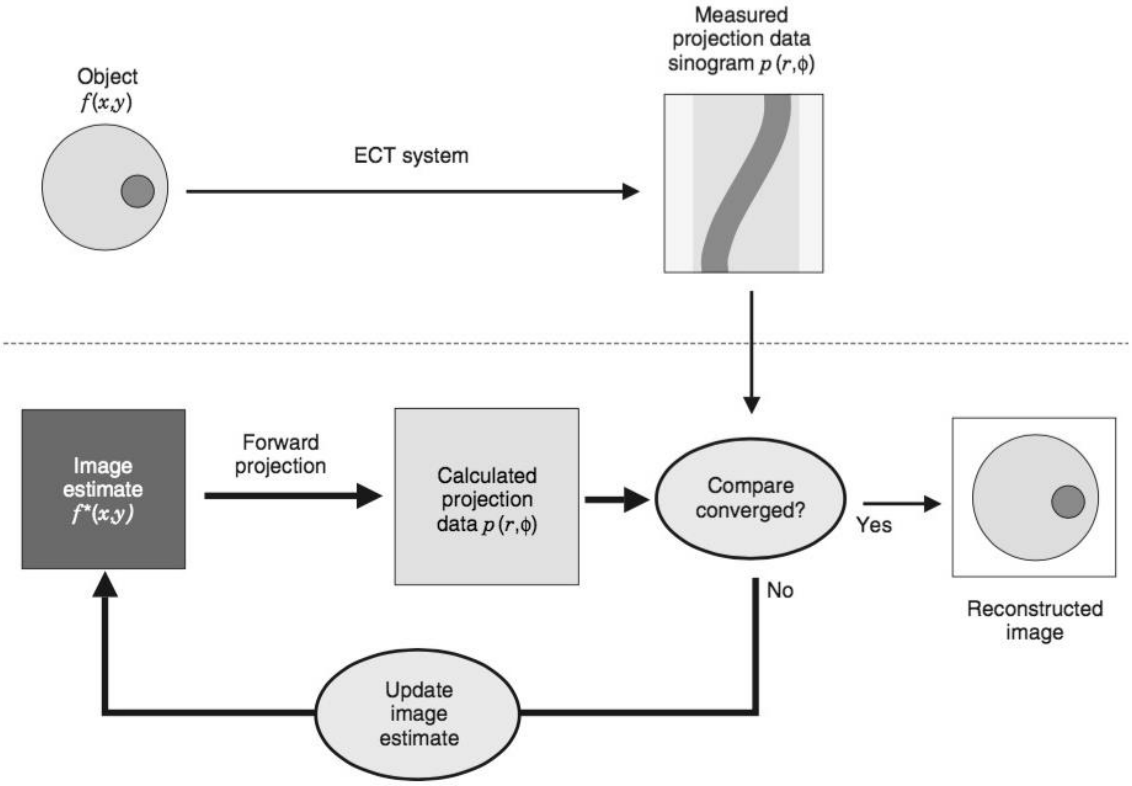

Figure 3.4: Schematic view of the iterative reconstruction process. Image adapted from (Cherry et al., 2012).

The main disadvantage of iterative reconstruction is the time needed for the reconstruction. Furthermore, the non-linearity makes it less predictable than conventional methods. Nevertheless, iterative reconstruction methods do not produce the artifacts observed in analytical methods, providing better signal-to-noise ratios. Overall, iterative methods reduce noise providing high-quality images and are currently included in all PET systems (Saha, 2010).

3.2.1 Maximum Likelihood Expectation-Maximization

Maximum Likelihood Expectation-Maximization (ML-EM) was one of the first iterative reconstruction methods applied to PET. It is based in the EM algorithm, which is widely used in different computer science applications such as machine learning, natural language processing or psychometrics (Aguiar, 2010). This algorithm deals with the discrete nature and the high noise of PET data. It requires the calculation of a SRM where each element ij represent the probability of a positron emission in voxel j to be detected in the LOR i, being the measured projection p_j:

$$p_j = \sum a_{ij} f_i$$

where f_i is the radiotracer distribution and a_{ij} are the elements of the SRM. The reconstruction inverse problem consists, in this context, in obtaining the radiotracer distribution f_i from the measured projections p_j. This could be done by inverting the

SRM, but this is not possible since it requires too many computational resources. The ML-EM algorithm is used to find a solution such that the estimated image produces the measured projections. After each iteration, the algorithm updates the image voxel values as:

$$f_j^{k+1} = \frac{f_j^k}{\sum_i a_i^j} \sum_i \frac{p_i a_{ij}}{\sum_m a_{im} f_m^k}$$

where f_j^k is the estimate at iteration *k* and $\sum_m a_{im} f_m^k$ are the projections obtained by forward-projecting f_j^k. ML-EM produces a solution such that $\sum_m a_{im} f_m^k = p_j$ with a given likelihood. This likelihood will increase with the iterations to a maximum value, while the noise also increases after each iteration (Aguiar, 2010). A compromise must be established between likelihood and noise level to decide the number of iterations to be made. In contrast with analytic reconstruction methods, in MLEM corrections for scatter, randoms and attenuation or normalization factors can be incorporated into the SRM a_{ij} (Hutton, 2011).

3.2.2 Ordered Subsets Expectation-Maximization (OSEM)

The main problem of ML-EM is that it is too slow, especially in 3D PET, where computing the SRM requires a very large amount of memory and computation time. Ordered Subsets Expectation-Maximization (OSEM) (Hudson & Larkin, 1994) is a modification of the ML-EM equation that makes the application of the method to clinical data more practical, and nowadays both 2D and 3D OSEM are commonly included on commercial systems. The projection data are divided in S disjoint angular subsets S_1, S_2,…..,S_s.., and the ML-EM algorithm is applied separately for each subset, which is known as a sub-iteration. The LOR data is separated in order of the projections into subset should be carefully chosen in order to maximize the new information at each sub-iteration. Then, the ML-EM equation updates the estimate for each subset, updating the estimate q_i^k after processing each subset:

$$f_j^{k+1} = \frac{f_j^k}{\sum_{i \in S_s} a_i^j} \sum_{i \in S_s} \frac{p_i a_{ij}}{\sum_m a_{im} f_m^k}$$

The convergence is accelerated by a factor similar to the number of subsets S, which makes possible to use iterative reconstruction in clinical scanners. *Figure 3.5* shows a comparison of different 3D reconstruction methods, showing the improvements on noise handling and the absence of artifacts of OSEM when compared with analytical reconstruction.

3.2.3 New developments on iterative reconstruction

3.2.3.1 Including physical effects into the SRM

Both ML-EM and OSEM assume that the measured data follow a Poisson noise distribution; so that the variations of counts for each LOR due to PET low counts are

independent from one LOR to another. This is true for raw uncorrected data, but the correction of effects such as attenuation, scatter, random coincidences or normalization over projection data could invalidate this precondition. Due to this, these physical effects should be included in the SRM or modelled into the reconstruction. Since the coefficient a_{ij} in the SRM is influenced by the attenuation or the probability of attenuation from the point of emission to the detector (Hutton, 2011), this effect can be included into the SRM. More commonly, an estimate of the scatter, calculated by one of the previously described methods, can be included in the projection step of the ML-EM as a background term as follows:

$$f_j^{k+1} = \frac{f_j^k}{\sum_i a_i^j} \sum_i \frac{p_i a_{ij}}{\sum_m a_{im} f_m^k + S}$$

where *S* is the scatter distribution. The SRM can be also easily modified to include information about the system resolution through the point spread function (PSF) and about randoms, normalization or even patient motion for motion correction.

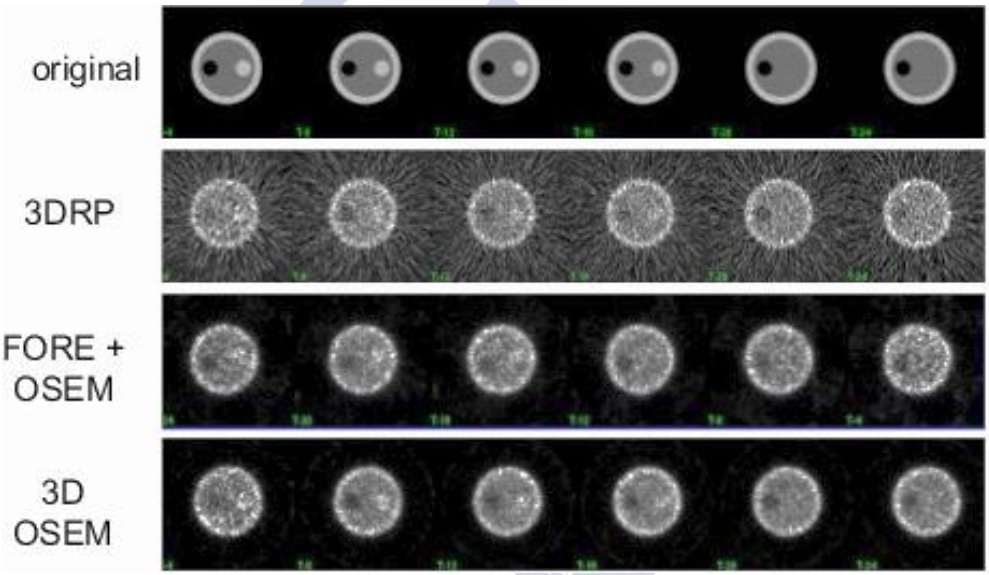

Figure 3.5: Comparison of different reconstruction methods including 3D reprojection (3DRP), FORE rebinning followed by 2D OSEM reconstruction and 3D OSEM.

3.2.3.2 Reducing noise

One of the main concerns in image reconstruction is handling the inherent noise in functional imaging data. In iterative reconstruction, noise increases with the number of iterations, and stopping the algorithm at earlier iterations is not optimal due to lack of convergence. Post-reconstruction smoothing can be applied after the reconstruction process, but with the consequent reduction of resolution. As alternative, 'prior' terms can be introduced to include additional information into the reconstruction, which has demonstrated to reduce image noise. The maximum a-posteriori (MAP) algorithm (Hebert & Lealhy, 1989) uses a penalty term, usually a function of the values in the immediate neighborhood of each voxel, which reduces noise by penalizing differences in between adjacent voxels. The MAP algorithm equation is as follows:

$$f_j^{k+1} = \frac{f_j^k}{\sum_i a_i^j + \beta \frac{dU}{df_j^k}} \sum_i \frac{p_i a_{ij}}{\sum_m a_{im} f_m^k}$$

where $U(f)$ is the penalty term and β is a scaling constant. Furthermore, additional terms providing additional information about the object, as separate anatomical images, can be introduced to ensure that the activity distribution is preserved.

3.2.3.3 Time of Flight (TOF)

Most recent scanners are equipped with Time of Flight (TOF) capabilities. Good timing resolution of a PET detector can be used to estimate the annihilation point between the two detectors by looking at the difference of arrival time between the two photons (ΔT). This process is illustrated in Figure 3.6 (reproduced from (Kadrmas et al., 2009)). This estimation provides improved contrast and signal-to-noise ratio due to a reduction in noise propagation during the image reconstruction process (Bailey et al., 2005) and a faster convergence in the reconstruction algorithm. Clinical studies have demonstrated that the incorporation of TOF provides better lesion detectability, especially for small lesions and for obese patients (Lois et al., 2009).

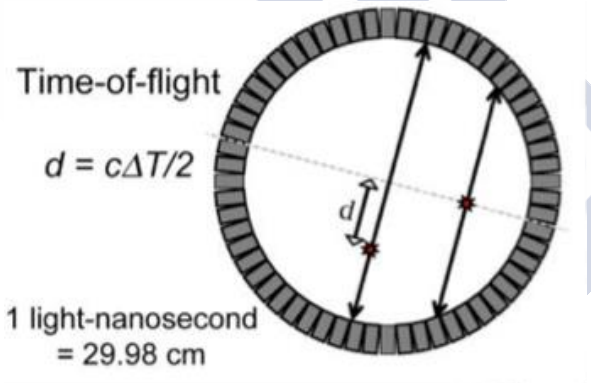

Figure 3.6: The difference between arrival times (ΔT) provides an estimation of the emission point (d).

3.3 THE STIR LIBRARY

STIR (Software for Tomographic Image Reconstruction) is an open-source software package written in C++, consisting of classes, functions and utilities for 3D PET image and SPECT image reconstruction (Thielemans et al., 2012). STIR provides the essential building blocks for image reconstruction, projection, and basic manipulations like format conversion, math operations and filtering. It provides libraries for two-dimensional and three-dimensional FBP, ML-EM and OSEM reconstruction. On its second release (STIR 2.0), STIR incorporates new scanner geometries, flexible and modular designs and additional features such as single scatter simulation (SSS), MAP penalties and additional iterative reconstruction algorithms. In its next release, STIR will incorporate TOF reconstruction capabilities and list-mode reconstruction.

4

Clinical PET

USC
UNIVERSIDADE
DE SANTIAGO
DE COMPOSTELA

4 CLINICAL PET

PET has always been exciting because of the potential application of new ligands in the clinic. Nevertheless, in contrast with SPECT, this potential has not been fully delivered, and PET is nowadays dominated by one single radiotracer, glucose analogue 2-deoxy-2-(^{18}F)-fluoro-D-glucose (^{18}F-FDG), which is sometimes complemented by a reduced number of alternative tracers (Farwell et al., 2014). Anyway, ^{18}F-FDG-PET yields excellent quality images, which can be appreciated by non-nuclear medicine clinicians in the first term, but also have an enormous clinical impact, as demonstrated in many early studies, most of them summarized by Gambhir et al. (2001). ^{18}F-FDG-PET can be used for studying brain metabolism, myocardial viability, infections and inflammations, and of course for detecting cancer, with thousands of studies being performed worldwide every day. Results from the National Oncologic PET Registry, which included data from 85,658 patients with a wide variety of cancer types, concluded that FDG-PET imaging changed physicians' intended management in about 36% of patients (Hillner et al., 2012), making PET an essential part of patient management.

4.1 FDG-PET IN ONCOLOGY

In the 1920s, Warburg reported that cancer cells have abnormally high rates of glycolysis. Even when tumour cells have sufficient oxygen supply, they prefer to produce energy using anaerobic glycolysis followed by a transformation of pyruvate into lactic acid. In addition, tumours often overexpress glucose transporters (GLUTs), allowing energy-independent transport of glucose across the cell membrane. In tumours, GLUT-1 is frequently overexpressed, but other transporters such as GLUT-2, GLUT-3, GLUT-4, GLUT-5, and GLUT-12 have been reported to present elevated levels in several tumours types (Szablewski, 2013). This mechanism offers a very general approach for cancer detection, especially for staging new or recurrent cancers. Most commonly imaged cancers with FDG-PET include lymphoma, head and neck cancer, lung, colorectal cancer, breast cancer, oesophageal cancer, melanoma, cervical cancer, thyroid cancer, and pancreatic cancer (Kelloff et al., 2005). *Figure 4.1* shows an example of a solitary pulmonary nodule imaged with FDG-PET. Others such as prostate cancer, bladder cancer, neuroendocrine cancer, and well-differentiated hepatocellular carcinoma, are often not contrasted enough in FDG-PET for different reasons, usually high uptake on surrounding tissue, while thyroid and breast tumours show very variable FDG uptakes (Hoh et al., 1998; Eubank & Mankoff, 2004), being susceptible to the use of other specific tracers.

One of the main weaknesses of ^{18}F-FDG comes from its main strength. Its unspecific nature allows using 18F-FDG in a wide variety of applications, but it also causes a high ratio of wrong or inconclusive diagnostics. Since elevated glycolysis is not limited to cancer cells, false-positive findings are still relatively common on ^{18}F-FDG-PET (Kelloff et al., 2005). Typical alternative causes of increased FDG uptake may include infectious and inflammatory processes, muscular activity or metabolism in brown fat. Due to this, new radiotracers for cancer diagnostics and treatment planning have been under development on recent years (Farwell et al., 2014).

Figure 4.1: Patient with lung cancer imaged with FDG-PET. Image is reproduced from (Kaira et al., 2009). Dark colours indicate high uptake, while light colours indicate low uptake. The dark spot in the left lung is the lung tumour.

Radiotracer	Target/Mechanism
^{18}F-FDG	Glucose Analogue
^{18}F-NaF	Chemisorption onto hydroxyapatite
^{11}C-choline	Lipid-metabolism agent associated with overexpression of choline kinase
^{18}F-choline	Lipid-metabolism agent associated with overexpression of choline kinase
^{68}Ga-PSMA	Low molecular weight urea-based PSMA inhibitor
^{11}C-acetate	Lipid-metabolism agent associated with overexpression of fatty acid synthase
^{18}F-FLT	Expression of thymidine kinase
^{18}F-FMISO	Accumulation in hypoxic cells via covalent binding
^{11}C-MET	Amino acid transporters
^{18}F-FET	Amino acid transporters
^{18}F-FMT	Amino acid transporters
^{18}F-FDOPA	Amino acid transporters

Table 4.1: Overview of Current PET tracers for cancer imaging. Data from (Farwell et al., 2014) and (Sharma, 2014).

Table 4.1 summarizes some of the radiotracers for oncology PET that are on the clinic or in clinical trial research nowadays. Many of them are related with increased protein synthesis in tumours because of their uncontrolled and accelerated growth. Increased protein synthesis expression is an excellent target for tumour imaging, and radiolabelled amino acids such as 11C-methionine (MET), 18F-fluoroethyl-tyrosine (FET), 18F-fluoromethyl-tyrosine (FMT) and 3,4-dihydroxy-6-18F-fluoro-L-phenylalanine (FDOPA) have been of great interest for the molecular imaging community (Dolfi et al., 2013). MET-PET and FDOPA have been extensively tested for the initial

diagnosis, grading, prognostication and treatment planning of cerebral gliomas and for distinguishing benign from malign tissue in head and neck cancer, melanoma and ovarian cancer (Inoue et al., 1996). *Figure 4.2* shows a comparison between FDG and FDOPA in a glioma patient. Another molecule that has raised interest along the community is choline, a compound that supports the synthesis of cell membranes. ^{18}F-fluorocholine (FCH) molecule labelled with ^{18}F showed the highest biological compatibility with choline, showing a biodistribution very similar to that of natural choline. This molecule, and its ^{11}C and ^{18}F labelled equivalents have been extensively used for the evaluation of prostate cancer (DeGrado et al., 2001), which has been strongly related with elevated levels of choline uptake and certain choline metabolites. More recently, prostate-specific membrane antigen (PSMA) labeled with ^{68}Ga have shown promising results on the accurate staging of primary disease and restaging of recurrent detection of metastatic lesions on prostate cancer (Mease et al., 2013).

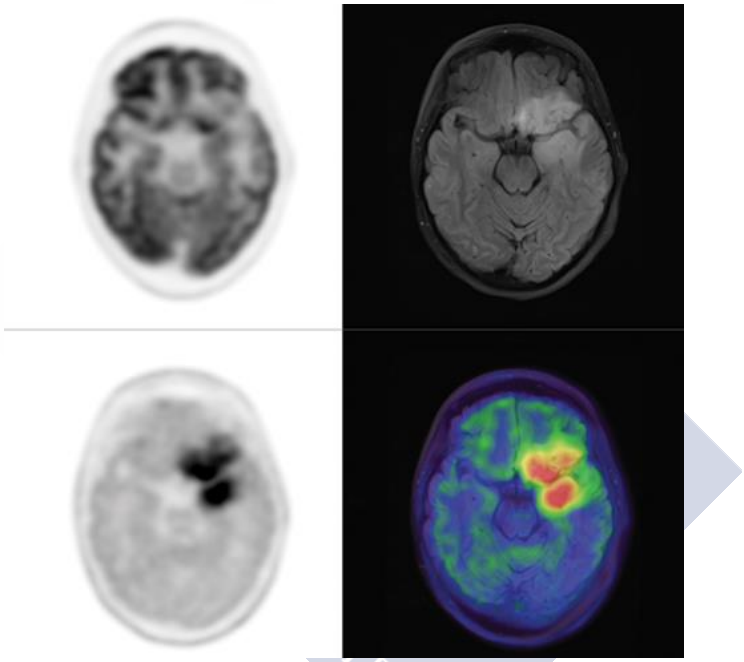

Figure 4.2: A glioma imaged with FDG (top left) and FDOPA PET (bottom left). We can observe the higher contrast of the amino acid imaging when compared with FDG. We also can see the much better correspondence between FDOPA and MRI image (top right). Bottom right shows FDOPA/MRI co-registration. Image is reproduced from Intech Open Acces library (*DOI: 10.5772/62823*)

Another interesting property of cancer is tumour hypoxia, which has been associated with treatment failure after radiotherapy and chemotherapy, and biomarkers for measuring the degree and extent of tumour hypoxia have the potential to play a significant role in staging and treatment planning for a wide variety of tumour types. During the last 20 years, different radiotracers have been developed intended to measure this key property (Sun et al., 2011). Of them, 18F-fluoromisonidazole (FMISO) has the largest body of preclinical validation studies and clinical experience. Recent studies have demonstrated that tumour hypoxia measured by FMISO-PET is predictive of patient outcome and that hypoxic tumours have considerably earlier relapse or progression (Lee et al., 2009). Due to this, FMISO is a promising radiotracer to complement primary

diagnostic with FDG, combining both metabolism and hypoxia information for treatment planning.

Further than primary diagnosis, detection of recurrence and treatment planning, FDG-PET has demonstrated to be useful for treatment monitoring and post-treatment response assessment. Many studies have shown that FDG-PET is useful for detecting early response, which is highly correlated with clinical outcome. The objective is to evaluate the effectiveness of the therapy faster than it is feasible through symptoms or other clinical parameters, which could allow for earlier changes to new therapeutic regimes in patients who are not responding. A recent study has pointed that PET changed intended management in about 50% of patients, including a switch to a different therapy in 27% of patients, an adjustment in dose or duration in 17% of patients, and a switch from therapy to observation or supportive care in 6% of patients (Hillner et al., 2008). These findings pointing that FDG-PET is capable of demonstrating changes in tumour biology hours to days after starting therapy are revolutionary when compared to conventional response measures by CT, which take weeks to months to evolve and can be misleading at early time points. Beyond ^{18}F-FDG, alternative radiotracers have been proposed for evaluating effective response to therapy based on different tumour characteristics. In this regard, a decline in proliferation is one of the earliest events in response to effective cancer therapy (Bading & Shields, 2008). The correlation between ^{18}F-FDG uptake and cellular proliferation is not very strong, but the alternative tracer ^{18}F-fluorothymidine (^{18}F-FLT), a thymidine analogue, demonstrates a much closer correlation between uptake and labelling with Ki-67, a cellular marker of proliferation, and can be used in combination with ^{18}F-FDG to assess response to therapy (See *Figure 4.3*) (Weber, 2010). Several studies have shown the ability of FLT-PET to measure tumour response after two weeks of treatment on different types of cancer, such as recurrent malignant brain neoplasms or breast cancer, showing a strong correlation between changes in FLT uptake during treatment and clinical response (Troost et al., 2010).

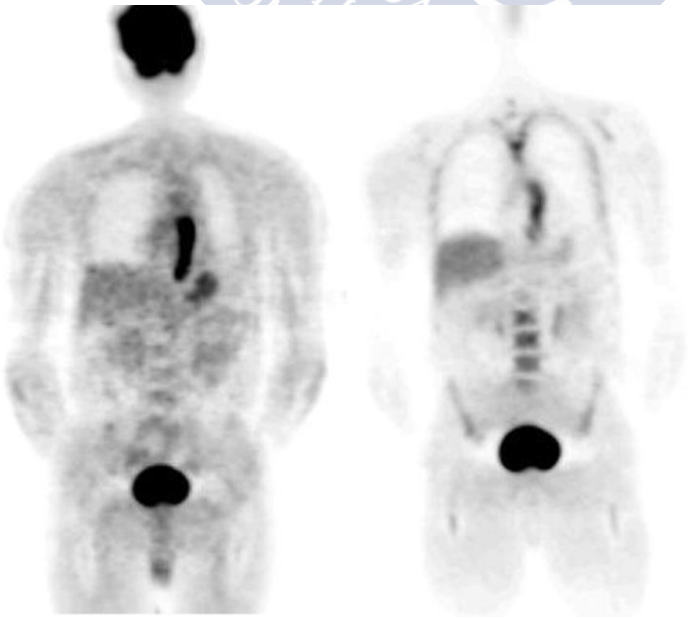

Figure 4.3: Comparison of FDG PET (left) and FLT PET (right) on a patient with esophageal cancer. Reproduced from (van Westreenen et al., 2005).

4.2 PET IN NEUROLOGY

Glucose is the main energy supply for the brain. Its metabolism maintains ion gradients and glutamate turnover and is closely coupled to neuronal function at rest and during functional activation (Sokoloff, 1977). Due to this ^{18}F-FDG-PET is extensively used for the investigation of brain metabolism and it is increasingly being proposed for many diagnostic purposes (Jones & Rabiner, 2012). The most common indications of brain ^{18}F-FDG-PET are early diagnosis of different dementias, differential diagnosis between Alzheimer's disease (AD) and frontotemporal dementia (FTD) (Herholz et al., 2002), pre-surgical evaluation of refractory epilepsy (Van Paesschen et al., 2007) and differentiation between Parkinson disease and atypical parkinsonian syndromes (Eckert et al., 2008).

In dementia, FDG-PET has a sensitivity of 93% and specificity of 76% in identifying progressive dementia in patients undergoing evaluation for cognitive impairment, and it exhibits characteristic hypometabolism patters for each of the diseases (Silverman et al., 2001). Alzheimer is characterized by hypometabolism in temporoparietal areas, which can be easily differentiated from frontal patterns in FTD or occipital affectation of dementia with Lewy bodies. Furthermore, PET evaluation before and after therapy with drugs as donepezil or rivastigmine is helpful in assessing the treatment benefits (Kumar et al., 2005). Furthermore, since AD is characterized by an abnormal accumulation of beta-amyloid plaques in certain areas of the brain, specifically binding compounds are being developed from radiolabelled beta-amyloid antibodies. The most widely validated of these radiotracer compounds is N-methyl-[11C]2-(4'-methylaminophenyl)-6-hydroxybenzothiazole, known as Pittsburgh Compound-B (^{11}C-PIB), showing a marked retention in AD patients in several brain regions (Lu & Yuan, 2015) (see *Figure 4.4*).

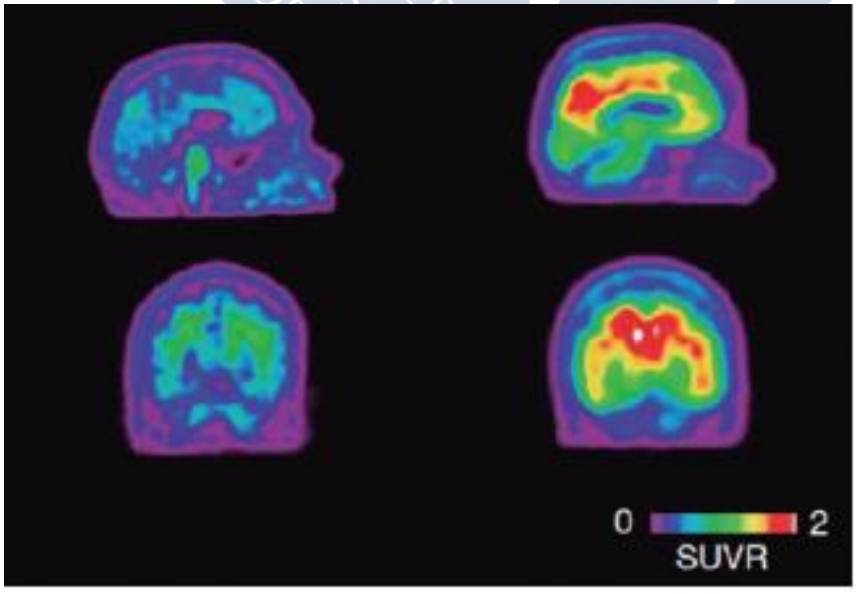

Figure 4.4: 11C-PIB images of a normal healthy subjet (left) and an Alzheimer's disease patient (right), showing accumulation of the radiotracer in amyloid plaques. Figure is reproduced from (Porcello et al., 2016)

Regarding epilepsy, interictal ^{18}F-FDG-PET is routinely used as a complement for MRI in the localization of the epileptogenic focus before surgery (Fuster et al., 2013) (Spencer, 1994). FDG-PET shows hypometabolic foci on the affected areas, and it has demonstrated to be more sensitive than MRI in certain situations (Won et al., 1999; Kassem et al., 2013). Furthermore, the usefulness and sensitivity of PET have increased in the later years by two main facts. First, the availability of co-registered PET/MR images has improved the interpretation of images of both modalities and enabled a more straightforward use of PET information on MRI-guided surgery (Shin et al., 2015). Second, the use of PET quantification techniques has improved the localization of the epileptogenic focus (Kim et al., 2002; Lee et al., 2002). *Figure 4.5* shows an example of an epilepsy PET/MR image.

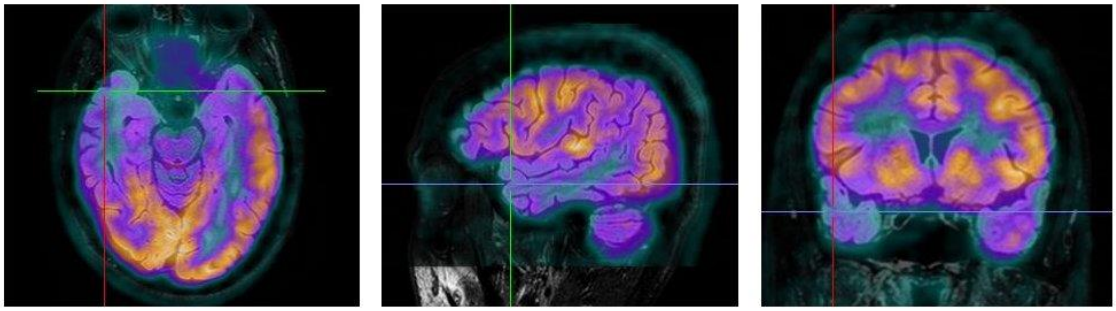

Figure 4.5: PET/MR co-registered image of a patient with temporal lobe epilepsy. Image is granted by the Molecular Imaging Research Group at IDIS (Santiago de Compostela).

4.3 PET IN CARDIOLOGY

In cardiology, PET is dominated by two radiotracers nowadays. The first one is cardiac perfusion measuring agent ^{13}N-ammonia, and the second one is ^{18}F-FDG, which can be used for evaluating myocardial viability after heart strokes. PET/CT indications have grown in last years, particularly for the diagnosis of the ischemic myocardium, obstructive coronary artery disease, and large vessel arteritis, in direct competition to using stand-alone CT and MR imaging for these applications. (Steiner, 2011).

4.4 FUTURE DEVELOPMENTS

PET imaging future will be determined by the arising of new radiotracers. Artificial beta emitters can be generated from common biological elements such as carbon (^{11}C), nitrogen (^{13}N), oxygen (^{15}O) and fluorine (^{18}F), that can be attached to molecules with either no or minimal impact on their behaviour in the body. This approach will allow to label any molecule of interest and to track its path through the body with minimal interference in the near future, placing PET as one of the most interesting technologies in the era of personalized medicine. Furthermore, technical developments will also drive the widespread of PET. Scanners are becoming significantly more sensitive leading to considerably faster patient throughput, and multimodality imaging, mainly PET/CT, has allowed combining molecular and anatomical imaging (Eubank et al., 1998). Furthermore, it allows us to perform PET simultaneously with CT in situations where CT would be the modality of chose on previous times, enabling an easier incorporation of PET on clinical routine. Recently, PET/MR imaging systems have hit the market promising to revolutionize the scene, but their clinical applications are still unclear.

However, the greatest benefits of multimodal imaging may eventually come from software, rather than hardware, because of the flexibility and cost-effectiveness of co-registering multiple imaging modalities as well as sequential PET acquisitions over time, which will be of increasing importance for PET-based treatment response follow-up. The true power derived from quantification will be revealed, as measurements of early tumour responses becomes routine practice. Many of these benefits come from the investment of time and money that industry is putting into PET as it is increasingly perceived as a major area of expansion in medicine. With increased patient throughput and a greater number of PET scanners and imaging resources, there are opportunities for PET to be used for current SPECT-based studies such as bone scans with ^{18}F-F-, cardiac perfusion and viability studies, and many other (e.g. imaging neuro- endocrine tumours using [^{111}In]-octreotide or [^{131}I]- mIBG). A lot will depend on the inventiveness of the cyclotron operators and radiochemists who will be responding to the clinical agenda.

USC
UNIVERSIDADE
DE SANTIAGO
DE COMPOSTELA

5

PET quantification

USC
UNIVERSIDADE
DE SANTIAGO
DE COMPOSTELA

5 PET QUANTIFICATION

The main advantage of PET when compared with other imaging modalities is the possibility of providing absolute or relative quantification values characterizing physiological and molecular processes; especially for the diagnosis, staging and treatment evaluation of cancer (Buvat, 2007). Image quantification needs two essential steps. The first step consists on translating the given counts from the detectors to measurements of radiotracer concentration. This step includes the introduction of the different corrections and proper image reconstruction, as explained in the previous sections. The second step is to propose physiological models describing the system in order to obtain meaningful quantitative parameters from these numbers of counts. These quantitative values result in a much deeper interpretation of the data when compared with the conventional visual interpretation of the images (Basu et al., 2011). This is especially relevant for differential diagnosis, when comparing a parameter value with a certain previously established level can help to assess the malignancy/benignancy of a tumour or for therapeutic management and follow-up, where quantification values for different stages of the disease are compared for evaluating the evolution of the disease or the efficiency of the treatment. Thus, quantification enables objective tumour characterization, reliable benignity/malignancy differential diagnosis, and early evaluation and monitoring of treatment response (Freudenberg et al., 2008; Weber, 2005). In the clinical routine, this quantitative evaluation is mainly based on a semi-quantitative parameter known as Standard Uptake Value (SUV), which provides an index of tissue FDG consumption.

5.1 SUV

The concentration of radioactivity (i.e. FDG) in a certain tissue depends on two main factors. First, the physiology of the given tissue and its avidity for the given molecule. Second, the input function, or the availability of the particular substance in the blood flow to fulfil this avidity (Bailey, 1998). In theory, it is possible to develop a mathematical model that can predict the amount of FDG in a given tissue knowing both of these variables, which in PET research is known as kinetic modelling. However, this requires the acquisition of dynamic data and continuous arterial blood sampling to obtain the input function, which is impractical for clinical practice (Hess et al., 2014). The risks of excessive bleeding, bruising and infection are too big to be clinically assumed. Due to this, a simpler semi-quantitative parameter known as Standardized Uptake Value (SUV) is usually used in the clinic, using a static image instead of dynamic acquisitions. The SUV reflects FDG uptake in a ROI at a certain time after FDG injection, assuming that the activity curves have reached a plateau in the given region. SUV is usually normalized to the injected dose and to the patient's body weight. SUV can be calculated by the following equation, and is usually expressed in units of g/ml:

$$SUV = \frac{c_{act}}{D/BW}$$

where c_{act} is the measured activity, D is the injected dose and BW is the body weight, which is used as an approximation of the body volume. Usually, maximum SUV (SUV_{max}, where c_{act} is the higher activity concentration on the ROI) or mean SUV (SUV_{mean}, where c_{act} is the average activity concentration on the ROI) are reported.

Different studies have shown the correlation between SUV and the glucose metabolism determined by kinetic modelling (Minn et al., 1993). It is important to remark that the SUV approximation works for FDG because it remains trapped in the cells, which is a necessary condition for fulfilling the plateau condition. This condition is not fulfilled for other tracers, being one of the reasons of the widespread of FDG-PET.

5.1.1 Applications of SUV in the clinical practice

Recent studies have shown that most anti-cancer drugs are effective only in less than 60% of the patients (Aspinall & Hamermesh, 2007). Thus, early understanding of the response of each individual patient to the treatment is of paramount importance. In this context, semi-quantitative measurements like SUV have proved to be more effective than the conventional visual assessment for distinguishing effective from ineffective treatment during early-stage follow-up (Wahl et al., 2009). Nowadays, all commercial PET scanners automatically calculate SUV, providing the physicians with quantitative values for the clinical routine, and several studies have demonstrated the usefulness of these values on the clinical practice.

One of the tumour types where SUV quantification plays a major role from its early days is lymphoma. It has been shown that the use of SUV for evaluating the response to first-line chemotherapy improves the prognostic value of early FDG-PET (Lin et al., 2007). The predictive accuracy of PET improves from 65% to 76% when quantitative analysis is added to a visual score. Furthermore, SUV is also used for determining the need of a biopsy after treatment of lymphomas (Ben-Haim & Ell, 2009).

Despite FDG-PET has limited value in the initial diagnosis and staging of breast cancer, it has proven to be useful for the detection of primary invasive breast cancer and especially in the assessment of disease recurrence, with an overall accuracy of 90%, and has been shown to guide changes in the management of up to 50% of these patients. SUV values has been used for the assessment of early response to therapy, and a reduction in the SUV as early as 8 days after initiation of therapy has been calculated in successful treatments (Cochet et al., 2014), preceding anatomical changes. After the first course of therapy, complete responders show a mean decrease in SUV of 85%, compared with a 22% decrease in non-responders. After two courses, SUV can predict pathological response with an accuracy of 87%, significantly higher than that of conventional imaging. Moreover, in multivariate analysis the change in SUV was the only factor predictive of complete response (Rousseau et al., 2006).

FDG-PET has also been extensively used in the diagnosis and staging of lung cancer. For diagnosis of lung nodules, the positive and negative predictive values are 91%, and 92%, respectively. A preoperative maximum SUV of 5.5 or higher is considered an independent predictor of relapse and death. There is also a close correlation of the change in SUV and the tumour response to therapy using a reduction of 20% in tumour SUV as a criterion for metabolic response (Weber et al., 2003).

Furthermore, SUV measurements of pre-therapy tumours have also been shown to predict survival in oesophageal cancer (Yanagawa et al., 2012), and some publications have shown the usefulness of SUV values for the early assessment of response to therapy

and in patients with ovarian cancer, uterine cancer, head and neck squamous cell carcinoma, sarcoma, mesothelioma, and melanoma (Ben-Haim & Ell, 2009).

5.1.2 Limitations of the SUV

Although the potential of quantitative FDG-PET has been clearly demonstrated and SUV values are routinely measured in most centres (90%) (Beyer, Czernin, & Freudenberg, 2011), large variations across institutions have been reported because of different procedures and methodologies (Graham et al., 2011), showing the necessity of standardized protocols (Adams et al., 2010). SUV values must be used carefully since they are affected by many different factors. Error sources affecting SUV values are divided in two groups, those related with physiological variability issues and those attributable to technical parameters related to the acquisition, reconstruction and quantification protocols. Recently, comprehensive descriptions of the different variability factors have been performed and new protocols for the standardization of FDG-PET studies in multicentre trials have been proposed (Boellaard et al., 2008; Boellaard, 2009). These guides include recommendations for patient preparation, in order to minimize physiological variability, and for administered FDG dose, acquisition protocol parameters, tomographic reconstruction and quantification procedures. Other technical and clinical studies have also been published in order to understand some of these factors, thus enabling a more accurate interpretation of SUV values. Regarding the physiological variations, high blood glucose level (Hoekstra et al., 2002), patient motion, (Lee et al., 2013) and high uptake in brown fat due to patient stress (Alkhawaldeh & Alavi, 2008) have been related to lower tumour SUV values. Regarding acquisition and reconstruction protocols, low spatial resolution or insufficient convergence can lead to lower SUV values, particularly for small lesions (Visvikis et al. 2012; Jaskowiak et al., 2005; Villeneuve et al., 2013). Finally, regarding the quantification procedure, SUV outcome depends on the region of interest (ROI) volume and type (Boellaard et al., 2004; Sattarivand & Caldwell, 2010) and SUV normalization (Hoekstra et al., 2002). These and other factors affecting SUV are summarized in *Table 8.1*.

5.2 BEYOND SUV

5.2.1 Metabolic Tumour Volume (MTV) and total lesion glycolysis (TLG)

Due to the high variability of SUV, different alternative measurements may offer benefits to PET imaging diagnostics. Metabolic Tumour Volume (MTV) is defined as the volume of tumour cells with increased FDG uptake, while total lesion glycolysis (TLG) is obtained by multiplying $MTV * SUV_{mean}$. Both parameters have shown promising results for patient prognosis and response to therapy on the clinical practice (Kiyohara et al., 2010), but they are compromised by the good delineation of the tumour, which has been a controversial topic since the start of PET quantification.

5.2.2 Heterogeneity and textural analysis

Tumour heterogeneity is defined as the coexistence of different types of cancerous cells with different morphology and physiologic behaviour within the same tumour. Recently, several studies have tried to develop parameters measuring tumour

heterogeneity, which is related with disease evolution, response to therapy and malignancy, since heterogeneous tumours have worse outcome and response to treatment. Because biopsy probes reflect only a particular part of the tumour, they will not reflect tumour heterogeneity, which could be analysed using alternative techniques such as imaging (Buvat et al., 2015). In FDG-PET, heterogeneity is evaluated as spatial variations in uptake represented by textural features, computational methods that can measure the relations between adjacent groups of pixels. These methods have been previously used in MRI and CT imaging (Lambin et al., 2012; Rahim et al., 2014), and have arrived to PET imaging in the last decade. Recent papers have pointed to the fact that there is a relationship between PET textural features and malignancy in different types of cancer (Soussan et al., 2014). An example can be observed in *Figure 5.1*.

Factor Affecting SUV	Effect
Blood glucose level	Increasing blood glucose level is correlated with lower uptake and SUV.
Uptake period	Higher SUV at increasing time interval between injection and start of PET study.
Patient motion/breathing	Image artefacts in case of mismatch in position between CT-AC and emission scan and lower SUV due to respiratory motion due to resolution loss.
Patient comfort	Patient stress and uncomfortable waiting conditions increase uptake of FDG in muscle and/or brown fat and may affect SUV quantification.
Inflammation	Inflammatory processes near or at the tumour results in a false positive increase of SUV.
Paravenous administration of FDG	Paravenous injection results in slow delivery of FDG to the tumour and therefore in incorrect SUV.
Scan acquisition parameters (acquisition mode, scan duration, bed overlap, FDG dose)	Affect signal to noise ratio (SNR) of PET scan. Poorer SNR results in an upward bias of SUV.
Image reconstruction settings (number of iterations, filters, matrix size, zoom factors)	Insufficient convergence and lower resolution results in lower SUV and increases partial volume effects. Moreover, insufficient convergence makes SUV more dependent on surrounding activity distributions.
Region of interest (ROI) strategy to derive SUV	Higher or lower SUV depending on size and type of ROI used.
Normalization factor in SUV calculation	SUV outcomes are numerically different when using body weight, body surface area or lean body mass as normalization factor in the SUV equation.
Correction for blood glucose level in SUV calculation	Higher blood glucose levels will result in underestimation of SUV. Use of a blood glucose level correction in the SUV equation will thus result in different SUV outcomes.
Use of contrast agents during CT-AC	Can result in overestimation of attenuation and thus results in higher SUV (upward bias).

Table 8.1: Main factor affecting SUV. Data reproduced from (Boellaard et al., 2008).

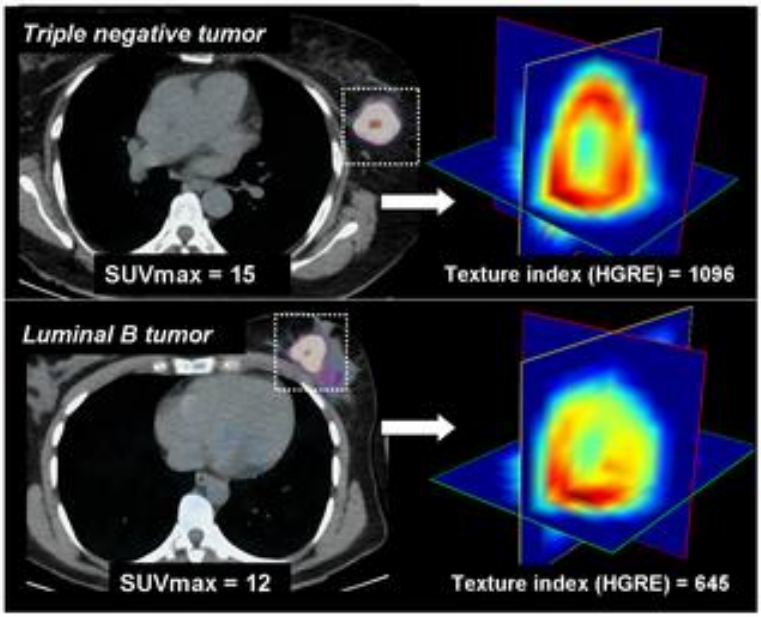

Figure 5.1: High-Gray-level Run Emphasis (HGRE) textural feature calculations for different breast tumours. A triple negative tumour shows higher SUV than a more aggressive luminal B tumour. Nevertheless, HGRE can correctly classify the tumours. Figure is reproduced from (Soussan et al., 2014).

USC
UNIVERSIDADE
DE SANTIAGO
DE COMPOSTELA

6

Monte Carlo simulation

USC
UNIVERSIDADE
DE SANTIAGO
DE COMPOSTELA

6 MONTE CARLO SIMULATION

Monte Carlo (MC) simulation techniques make use of random numbers as the base to simulate any specific situation. These methods are used to solve very complicated deterministic problems by applying a statistical approach. The implementation of modern MC methods and its application to physics problems have to be acknowledged to Stanislaw Ulam, who developed the methods while working on the Manhattan Project. Since then, MC methods have been extensively applied to physics and other fields of science (Raeside, 1976). MC methods were originally named statistical sampling methods, but due to the similarity between its random behaviour and casino games such as wheels or roulettes, they were finally named MC simulations, in reference to the Monte Carlo casino in Monaco. MC simulation relies in the fact that the simulated physical processes which can be modelled from probability density functions (PDF). Due to the stochastic nature of emission radiation, transport and detection, SPECT and PET systems are ideal for Monte Carlo techniques (Andrea, 1991).

6.1 MC METHODS IN NUCLEAR MEDICINE

The advance in computer power and the availability of parallel processing systems has increased the use of the MC techniques as a research tool for emission tomography, mainly for simulating the physical processes inside the scanner. It can serve for evaluating and improving design, corrections, dosimetry and acquisition, reconstruction and quantification protocols. *Figure 6.1* shows the increase of the number of papers using MC simulation for radiation physics research from 1970 to 2000. MC simulations have multiples advantages with respect to the experimental measurements. For instance, the simulations yield information about the system that is impossible to obtain by physical measurement. Furthermore, a simulation can often be carried out quickly and cheaply, while experimental measurements are often very expensive. For radiation transport problems, the computational model includes geometry and material specifications. Every computer code contains a database of experimentally obtained quantities, known as cross-sections, which determine the probability of a particle interacting with the medium through which it is transported (Zaidi, 1999). Nowadays, MC methods are used in emission tomography to optimize design parameters such as sensitivity and resolution, to study image degradation issues such as attenuation, scatter, positron range or statistical noise, or to evaluate correction methods, image reconstruction algorithms and quantification methods.

6.1.1 MC methods for assessing quantification methods

SUV has been much discussed it is not still widely accepted (Visser et al.,2010). This is due to that the uncertainties affecting the SUV are not well documented, in particular those accounting for changes during the treatment. SUV can be affected by many different parameters, for example those accounting for physiological changes between patients or between the same patient and those attributable to technical issues related to acquisition, reconstruction and quantification protocols (Boellaard, 2011). In the last years, several descriptions of the variability sources affecting PET quantification have been published in literature, enabling a more accurate interpretation of quantitative values. Using

anthropomorphic physical phantoms carries out a lot of these studies, being these phantoms ideal for the investigation of the impact of changing technical factors on the output images, enabling us for applications where patients cannot serve or should not serve (Schwartz et al., 2011). The limitations of these physical phantoms are reduced flexibility for changing shapes and volumes of the internal structures, high cost and cumbersome to use. The usage of radioactivity sources and manipulation of radiotracers are also a shortcoming on pure research facilities. An alternative is the use of digital phantoms, so that simulated PET studies are generated from the projection of phantoms by using analytical or Monte Carlo (MC) simulation techniques (Zaidi, 1999). Simulation techniques have been used to evaluate different parameters of PET systems and to assess potential issues on design that would be very complicated, expensive and time demanding on the hardware development phase, and they have become essential for nuclear medicine system design (Popota et al., 2015). Furthermore, MC methods are also used to the evaluation of scatter and attenuation correction methods, motion correction and reconstruction algorithms and quantification methods (Rogers, 2006).

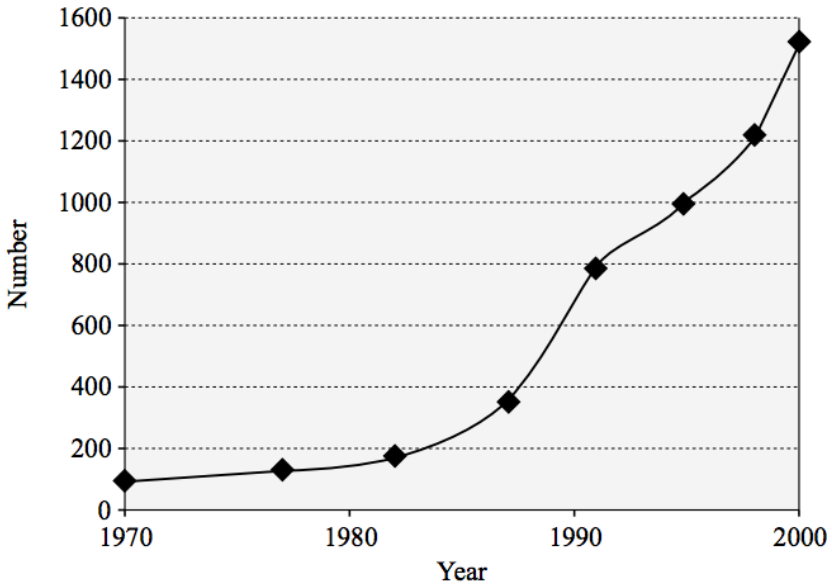

Figure 6.1: Number of published papers on MC simulation applications in medical radiation physics from 1970 from 2000. Figure reproduced from (Buvat & Castiglioni, 2002)

Due to the active use of these techniques, many different software alternatives specific for nuclear medicine are available right now for the MC simulation of PET systems, being the most widely used GATE (GEANT4 Application for Tomographic Emission) (Jan et al., 2011) and SimSET (Simulation System for Emission Tomography). While GATE is a powerful tool for PET detector design in the lowest level, SimSET provides much faster data generation while providing less detail into the simulation, without integrated models for system electronics and signal processing and more basic photon transport physics. *Figure 6.2* shows an example of a MC simulation performed with Gate version 6.2

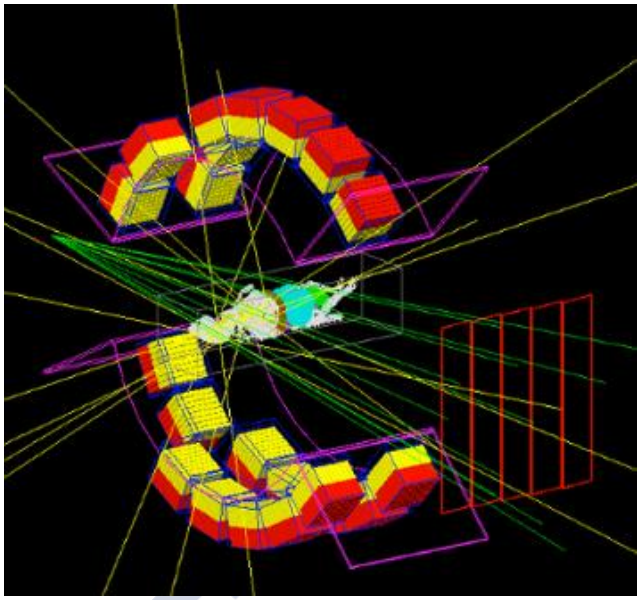

Figure 6.2: MC simulation of a partial ring PET scanner. Reproduced from Gate Collaboration web page.

6.1.1.1 SimSET 2.9.2

SimSET 2.9.2 (Simulation System for Emission Tomography, version 2.9.2) is an open-source dedicated MC code for use in molecular imaging developed by Robert Harrison in the University of Washington Imaging Research Laboratory since 1993 (Harrison, 2010). The software is written in C-language and divided in modules (mainly object, detectors, collimators, photon history generator and binning).

SimSET detector module provides a range of different detector models of increasing complexity. The photon history generator tracks photons through the specified object and detector, recording the interactions within them for each photon. The interactions are used to compute a detected location and total energy deposited on the detector. The simplest of SimSET detectors is the 'simplePET' model. This model does not simulate any detector interaction, taking account only of the object photon propagation. Finally, it applies an analytical Gaussian blurring on detected energy to emulate the limited energy resolution and it bins the data on the specified number of bins by the binning module. Main counterpart of the 'simplePET' is that detection efficiency is 100%, needing large correction factors in order to provide realistic noise to the images. The 'cylindricalPET' detector software models the detector as a series of adjacent regular right cylinders with transaxial layers. Photon interactions within the detector including scatter, absorption, and depth of interaction are simulated, but there are no blocks and hence no gap effects that are only present in the block detectors, so sensitivity is slightly overestimated. This simulation model is much more accurate than the simplePET, but also more time consuming due to the simulation and tracking of each individual photon through the detector. Efficiency correction factors are applied to compensate for differences in scintillator volumes and sensitivity due to the lack of gaps between the detectors. Random coincidences are added analytically after the simulation using the tools provided by tools provided by the library but they require storing the data in list mode. SimSET MC simulation toolkit provides since version 2.9.2 the ability of simulating block detectors,

providing a new layer of complexity to perform more realistic simulations. Unfortunately, these more realistic simulation techniques also have an impact on time performance.

6.2 ANTHROPOMORPHIC PHANTOMS

Despite the huge advances in the development of Monte Carlo Codes for nuclear medicine, another key part for obtaining a realistic simulation is the availability of the necessary phantoms, computational models that are used for the representation of patients in simulation experiments in order to develop new image-reconstruction and processing algorithms. These anthropomorphic phantoms can be defined by mathematical functions, digital (voxel-based) volume arrays, or hybrid equation-voxel models. Mathematical models are built by combining simple continuous objects in order to obtain the most realistic possible representation of the human body, while voxel-based models are derived from segmented and labelled voxels from patient's medical images of different modalities. While voxel-based models are usually more realistic, mathematical models assume that any complex radioactivity distribution and corresponding attenuation properties of the human body can be modelled with simplified geometrical shapes. In contrast, mathematical models are more suitable for applications involving anatomical variability and temporal changes such as respiratory or cardiac motion corrections (Zaidi & Xu, 2007). Since the start of the development of mathematical phantoms, many efforts have been done to deliver most accurate phantoms. Of these, the most wide-spread have been the ones provided by the Medical Internal Radiation Dose (MIRD) Committee of the Society of Nuclear Medicine (SNM) in the United States (you can see the current version on *Figure 6.3*). For many years, these stylized models have served to the radiation-protection community.

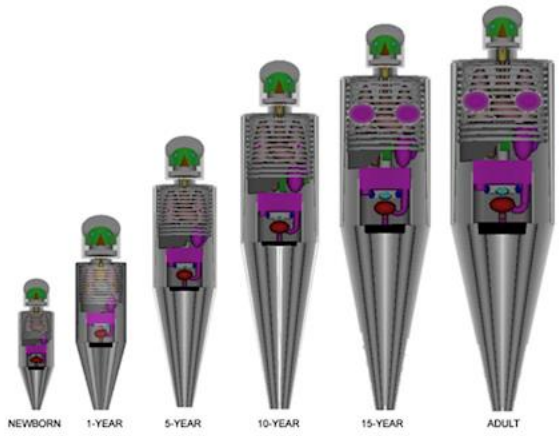

Figure 6.3: Female MIRD phantoms for different ages. Licensed under Public Domain via Commons.

Unlike mathematical whole-body phantoms, voxelized phantoms are image-like data containing a huge number of tiny cubes grouped to represent each anatomical structure. The creation of a voxelized phantom involves the acquisition of a set of medical images and the (usually manual) segmentation of the different organs, which is a very time-consuming and laborious process (Zaidi & Xu, 2007). The most popular voxelized anthropomorphic phantom was developed by Zubal et al. (1994) from Yale University in 1994, and it is known as the VoxelMan or just the Zubal's phantom, being the first computational model developed for optimizing nuclear medicine imaging protocols.

Other relevant voxelized phantom is the VIPman (Xu et al., 2000), one of the most realistic computerized phantoms until know, based on cross-sectional photography of a 39-year-old male corpse. The detail difference between the VIPman and the mathematical models of MIRD can be observed in *Figure 6.4*.

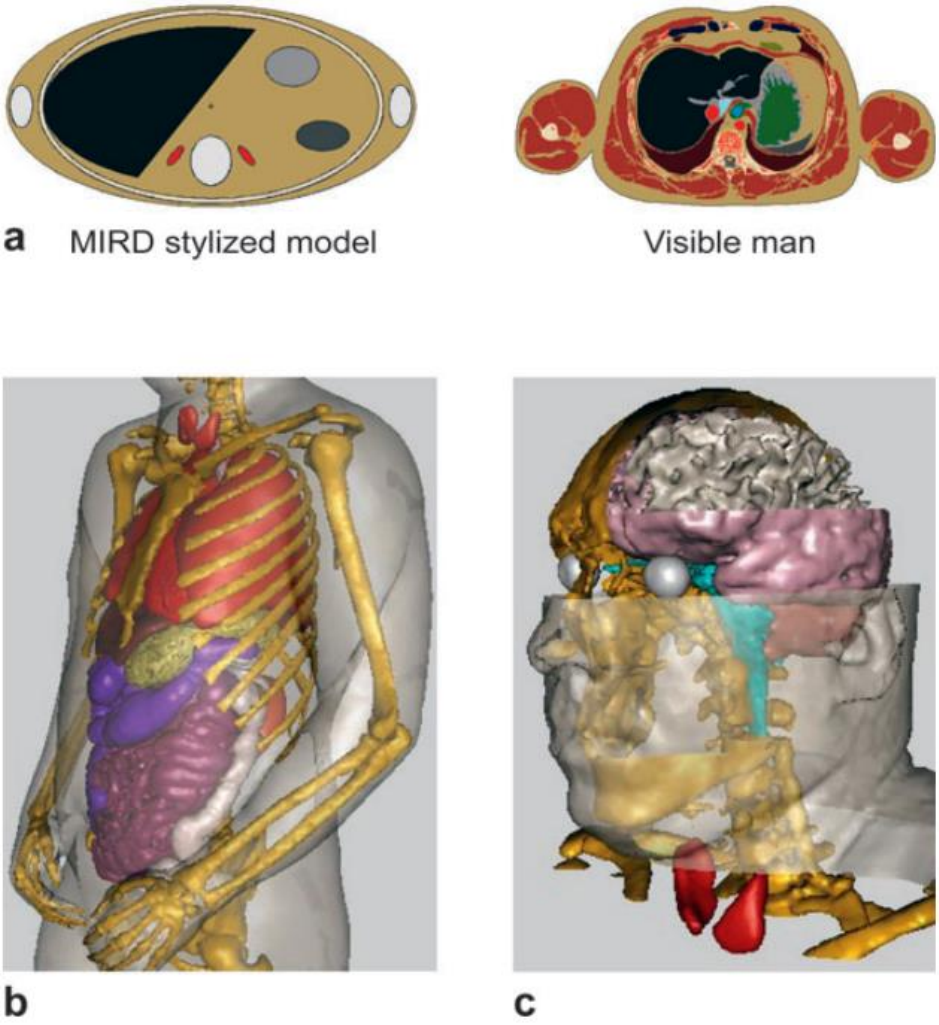

Figure 6.4: (a) Comparison of axial sections from the MIRD (top left) and the VIPMan phantom (top right), showing the details from the liver (black) area. (b) 3D model of the VIPman torso. (c) 3D model of the VIPman head. Figure modified from (Zaidi & Xu, 2007).

6.2.1 The XCAT Phantom

In addition to mathematical and voxelized models, recent developments are centered on hybrid phantoms exploiting the advantages of the two types. Hybrid phantoms are based on segmentations of real data, that later is processed with polygonal meshes to define each anatomical object, usually by using non-uniform rational B-splines (NURBS), which can accurately model any surface on the body, providing mathematical models while preserving the details of voxelized phantoms. Of these phantoms, one of the most popular is the 4D extended cardiac-torso (XCAT) phantom (Seagars et al., 2010). The XCAT phantom provides the details in the VIPman, while adding versatility

to have phantoms of different genders and ages (See *Figure 6.4*) and mathematical models for cardiac and respiratory motion.

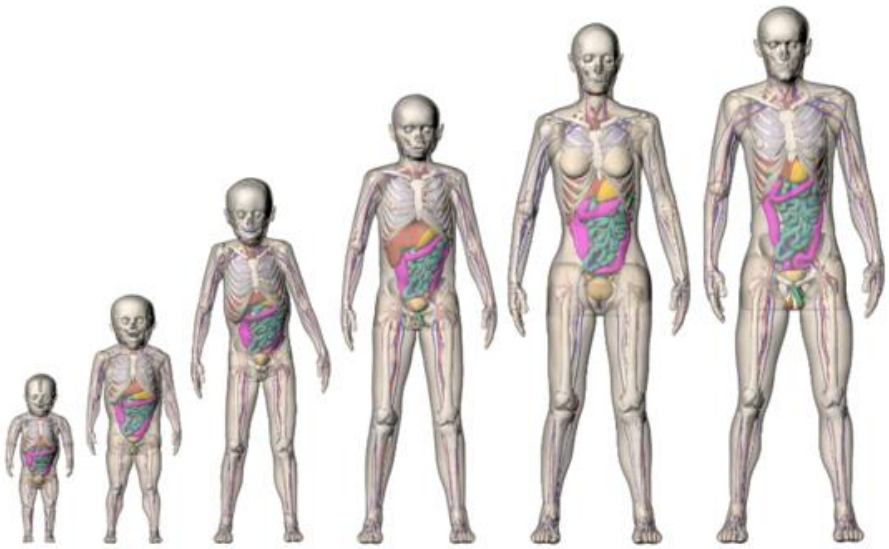

Figure 6.4: XCAT phantom models for different ages and genders. Image is reproduced from the Duke University File (Duke File #: 3513).

Recently, respiratory-induced errors in tumour SUV were recently evaluated by using the XCAT anthropomorphic digital phantom (Geramifar et al., 2013). Multiple PET studies were simulated from analytical projections of the phantom. The use of Monte Carlo simulation methods instead of analytical projectors for simulating PET studies is more realistic.

7

Aims of this thesis

USC
UNIVERSIDADE
DE SANTIAGO
DE COMPOSTELA

7 AIMS OF THIS THESIS

7.1 STATEMENT OF THE PROBLEM

Although the information from PET images has been traditionally evaluated by a qualitative visual inspection, the current trends in PET clinical research advance towards the quantitative analysis, which provides reliable and reproducible numerical measures that cannot be obtained qualitatively, offering additional information for a more precise diagnosis. Despite the good results provided by SUV during years, significant efforts are still needed to apply SUV in differential diagnosis, and especially in treatment follow-up, where the necessity to detect smaller changes requires a better understanding of SUV and its uncertainty. Regarding this, both the image quality and the quantitative accuracy of PET can be degraded by several effects, which we tried to describe in the previous sections. First, we identified physical factors such as gamma photons undergoing scatter processes prior to detection (scattered coincidences), two photons which do not arise from the same annihilation being detected within the same coincidence time window (random coincidences), positron range or non-collinearity, which can degrade PET data acquisition. In addition, the number of detected coincidences is limited and the effect of image noise can be important, while the requirements of administering smaller doses due to radiation protection need to be fulfilled. Second, we discussed physiological changes between patients and between different studies on the same patient, such as different glucose levels, inflammation, variations in the accumulation of the radiotracer in the bladder or muscular uptake due to stress, discomfort or cold. Finally, we reviewed technical factors related with patient handling (residual activity in the syringe, paravenous injection, variable uptake period), reconstruction (insufficient iterations, bad co-registration between attenuation and activity, etc..) or quantification (bad ROI placing, bad SUV normalization). Many studies have been published in the last decade evaluating some of these factors. Most of these studies are carried out by using anthropomorphic physical phantoms or patient data. Physical phantoms are ideal for investigating the impact of changing technical factors on the output images, enabling us for applications where patients cannot serve or should not serve, but they have reduced flexibility for changing shapes and volumes of the internal structures, high cost and cumbersome to use. Patient data offers a very realistic framework for evaluating different parameters related with the number of counts, the reconstruction or the quantification procedures, but they are not suitable for many other the applications. As an alternative, MC simulation is a very appealing solution since it is cheap, it does not require the use of radioactivity sources, and it provides a well-controlled framework where all the parameters are known *a priori*, allowing a precise evaluation of each individual uncertainty source. Nevertheless, the simulation of realistic patient studies requires a solid methodology including a deep understanding of the studied problem, in order to generate realistic databases of digital phantoms, the use of validated MC models of the real scanners and a good reproduction of the reconstruction process.

7.2 GENERAL AIM

The general aim of this thesis was the evaluation of the different factors affecting SUV and the development of correction and standardization methods for improving the quantification accuracy of Positron Emission Tomography (PET) images.

7.3 SPECIFIC AIMS

a) Evaluation and correction of the impact of the extravasation of the injected dose in whole-body PET studies.

b) Evaluation of the robustness of different SUV metrics (SUV_{max}, SUV_{mean}, SUV_{peak}) in low-dose studies, in terms of accuracy and reproducibility.

c) Evaluation of the impact of variable muscular uptake due to patient stress, discomfort or cold, in SUV quantification.

d) Evaluation and correction of the impact of spill-in counts coming from the bladder on the quantitative evaluation of tumours in the pelvic region.

8

Cohesion of this thesis

USC
UNIVERSIDADE
DE SANTIAGO
DE COMPOSTELA

8 COHESION OF THIS THESIS

The cohesion of this thesis comes from the development of a methodology for the Monte Carlo simulation of clinical studies, and its application to different problems related with SUV variability. The designed workflow is based on the generation of simulated whole-body ^{18}F-FDG and ^{18}F-Fluorocholine (FCH) studies using SimSET, STIR and the XCAT phantom. All phantoms were based on the anatomy of an average Caucasian adult male human (172 cm, 76 Kg) and the uptake of the different tissues and radiotracers was obtained from real patients derived to our Nuclear Medicine Department and from bibliography, which provides activity concentrations, contrast ratios or SUV variations with time measured on patient studies.

The simulation of the generated phantoms was performed using the SimSET package. The scanner geometry was based on the General Electric (GE) Advance NXi PET scanner present at our Nuclear Medicine Department. Our model was based on previous models developed with SimSET and GATE (Barret et al., 2005), and was validated by comparing real and simulated NEMA tests, obtaining an accuracy within 5% in terms of resolution, sensitivity, scatter fraction, contrast recovery and noise. Realistic acquisition times of 300 seconds per bed were simulated. The number of simulated photons was carefully adjusted to obtain realistic signal-to-noise ratios, and the simulations were performed on a computer cluster with computer nodes including a Xeon® Processor E5-2418L (Intel Corporation, Santa Clara, California, United States) and 8 GB DDR3 RAM. Each simulation was performed on an individual node divided on 8 sub-processes in order to use the eight threads of the processor. Variance reduction tools on SimSET were activated to improve simulation times. Each simulation consumed around 200 hours of CPU time adding the time used by the eight processes.

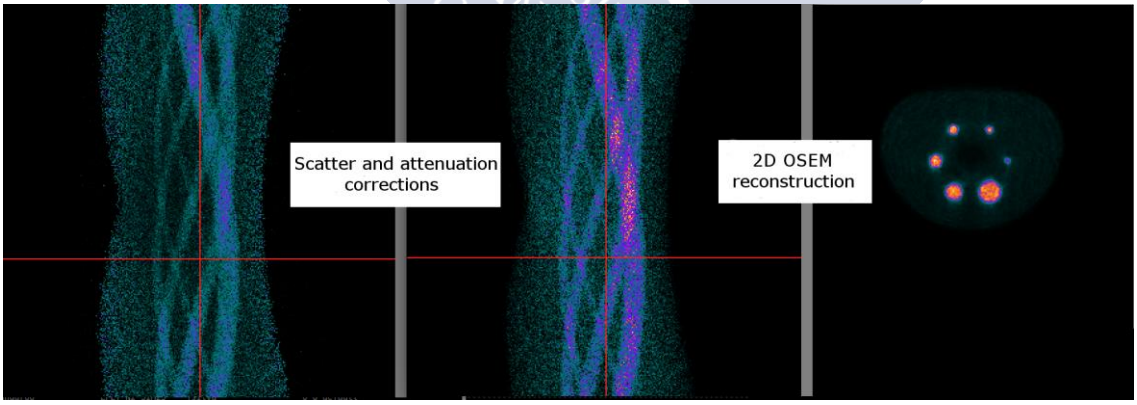

Figure 8.1: Example of the simulation and reconstruction process. We can see the SimSET simulated sinograms (left), the sinograms after attenuation and scatter correction (center) and the reconstructed image (STIR) of the NEMA IEC phantom (right).

Attenuation and scattered photons were pre-corrected before the reconstruction, following the methodology followed for the particular system by the scanner manufacturer (Bailey & Meickle, 1994). The reconstruction was performed (if the contrary is not stated) with the OSEM implementation present in STIR library release 2.2. Reconstruction parameters were tuned to fit those in the scanner. Sixteen full iterations

were performed (16 sub-iterations, 2 subsets), and no post-filtering was applied. Matrix and voxel size of the reconstructed images were 128x128x35 and 4.3x4.3x4.47 mm3 respectively, as in the manufacturer protocols. An example of the simulation and reconstruction process is shown in *Figure 8.1*. This framework enabled us to compare the SUV values obtained from the simulated PET images with the real SUV value (simulated value), thus making it possible to evaluate the accuracy and repeatability of SUV quantification under different conditions. An example of the workflow is shown in *Figure 8.2*. This methodology was applied to four different problems affecting SUV robustness that were previously described, giving rise to the presented journal articles.

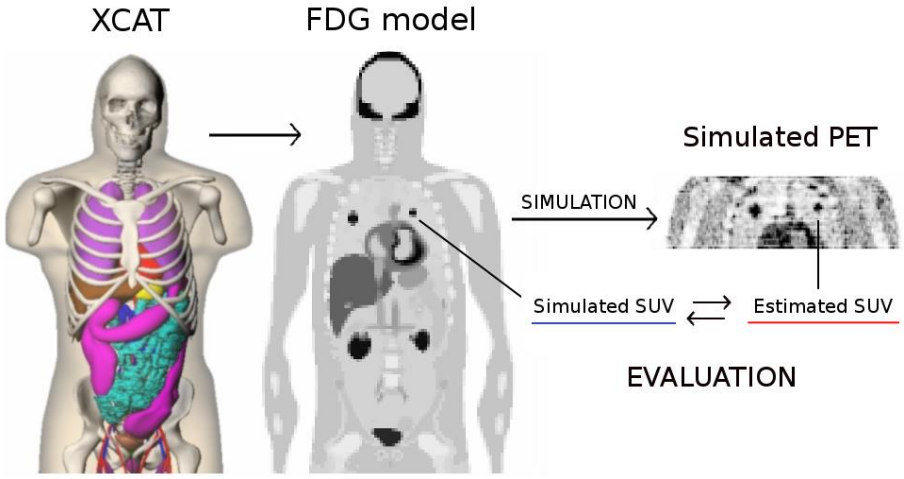

Figure 8.2: Workflow was based a realistic framework of multiple simulated FDG-PET studies

Article List

Part II: Journal Articles

9 **CORRECTION FOR FDG PET DOSE EXTRAVASATIONS: MONTE CARLO VALIDATION AND QUANTITATIVE EVALUATION OF PATIENT STUDIES**

LINK: http://onlinelibrary.wiley.com/doi/10.1118/1.4870979/abstract

10 **SIMULATED FDG-PET STUDIES FOR THE ASSESSMENT OF SUV QUANTIFICATION METHODS**

LINK: http://www.sciencedirect.com/science/article/pii/S2253654X14001474

11 **IMPACT OF MUSCULAR UPTAKE AND STATISTICAL NOISE ON TUMOR QUANTIFICATION BASED ON SIMULATED FDG-PET STUDIES**

LINK: http://www.sciencedirect.com/science/article/pii/S0969806X16305540

12 **IMPACT AND CORRECTION OF THE BLADDER UPTAKE ON ^{18}F-FCH- PET QUANTIFICATION: A SIMULATION STUDY USING THE XCAT2 PHANTOM**

LINK: http://iopscience.iop.org/article/10.1088/0031-9155/61/2/758

13

Discussion

USC
UNIVERSIDADE
DE SANTIAGO
DE COMPOSTELA

13 DISCUSSION

MC simulation is a very interesting approach for the evaluation of PET acquisition, reconstruction and quantification methods. It does not require the use of radioactivity sources, it provides a well-controlled framework where all the parameters are known a priori, and it allows a precise evaluation of each individual uncertainty source. Nevertheless, the simulation of realistic patient studies requires a solid methodology including the generation of realistic databases of digital phantoms, the use of validated MC models of the real scanners and a good reproduction of the reconstruction process.

As a first part of this thesis, we have developed a methodology for the simulation and reconstruction of studies from the GE Advance NXi scanner. The main objective was to have a framework for the simulation of clinical PET studies from our scanner. This methodology was afterwards applied to different problems related with SUV uncertainty. The selected problems were the dose extravasation due to a paravenous injection of the radiotracer, the image noise due to low dose, the SUV variations due to the physiological variations of SUV uptake and the spill-in effect when evaluating areas surrounded by high activity sources. After the development of the MC model, the challenge for each of these evaluations was the generation of realistic anthropomorphic phantoms including these effects.

First, we evaluated the impact of dose extravasations in the SUV. The evaluation, based on XCAT phantom, was carried out in order to mimic complex patient extravasations varying shapes, volumes and concentrations. Proper activity indexes for different organs and tissues were used to simulate the normal physiologic distribution of the FDG tracer, and volumes of different complex shapes were added in the anthropomorphic phantom's arm in order to mimic real extravasations in patients. The extravasated doses were simulated by adding volumes of different and complex shapes on the patient arm. Two methods for estimating the extravasated dose were proposed (manual-based and threshold-based) focusing in accuracy and easiness in order to enable a future clinical application, and their accuracy and repeatability were evaluated using our MC methodology. The performance of both methods showed relative bias below 5% for PVI doses higher than 1% of the injected dose. Although the PVI volume could be more closely encapsulated by using the threshold segmentation (only predefined simple shapes were used in manual ROI method), a similar performance was found for manual and threshold ROI methods. The problem was then evaluated in patient studies. A visual inspection of our patient database (1367 patients) revealed that 18% of the patients presented some kind of paravenous injection, which was in good agreement with previous works (Osman et al., 2011; Hall et al., 2006). The subsequent analysis of the patient database by using the validated PVI estimation methods showed that only a small fraction of the patients (2%) presented PVI doses higher than a 1% of the injected dose. Nevertheless, the extravasated dose was important in some patients, with values up to a maximum of a 22% of the injected dose, and was especially important for paediatric studies. It has to be mentioned that different repeatability studies have shown that SUV uncertainty is around 10% (Kinahan & Fletcher, 2010; Schwartz et al., 2011), so in these cases PVI contribution would be very relevant. Applying the proposed correction

methods, doses can be estimated with an error below 5%, allowing an accurate estimation of the SUV quantification on these FDG-PET studies.

For the evaluation of noise and the performance of SUV in low dose PET, we added three spherical lung lesions to our anthropomorphic activity and attenuation maps in order to mimic solitary pulmonary nodules with a theoretical SUV of 4.3 and diameters of 31, 21 and 9 mm. SUV_{max}, SUV_{mean} and SUV_{50} were obtained from the different noise realizations, injected doses and tumour sizes. The obtained SUV values were averaged over noise realizations and then compared to the simulated SUV values for different tumour sizes and injected doses. The repeatability of the SUV measurements was evaluated as the Standard Deviation (STD) of the ten simulations. Our results showed an overestimation associated with $SUV_{max,}$ which can be explained by the statistical noise level. SUV_{mean} showed significant underestimations for all lesion sizes and without significant changes with the injected dose. This can be explained by the partial volume effect, due to which part of the tumour activity is outside the delineated tumour ROI. Finally, SUV_{50} provided the best match to the simulated values, with excellent accuracy for lesion sizes of 31mm and 21mm, and only a slight underestimation for the smallest lesion. Nevertheless, in most cases, SUV estimations matching the real uptake values are not required in clinical routine, where SUV estimations are compared with estimated values from other FDG-PET studies. In this regard, the repeatability of SUV_{max} and SUV_{50} estimations was ranged between 2% and 8% for injected doses greater than 3mCi and it increased significantly for doses below this value. Instead, the variability of SUV_{mean} was below 5% for all lesion sizes and injected doses greater than 3mCi. In terms of repeatability, the tumour quantification based on SUV_{mean} showed a better performance than SUV_{50}, in particular for small lesions, where the ROI used for SUV_{50} estimation had a very small number of pixels, making SUV_{50} very similar to SUV_{max}. Overall, SUV_{50} showed better performance for accurately estimating tumour SUV values. These results were in agreement with recently reported data that showed SUV_{50} provides accurate quantifications (Sher et al., 2016). On the other hand, SUV_{mean} showed better results in terms of repeatability. This is because ROI delineation for SUV_{50} depends on the value of a single-pixel maximum. Another remarkable observation is that a reduction of dose in the range from 9 to 3 mCi would not affect significantly the results of quantification when SUV_{mean} and SUV_{50} estimations were used. It can be expected that further studies in modern scanners could demonstrate that these doses can be even lower. It has to be pointed that we did not perform any detectability studies, so image quality degradation due to the increased noise might have an impact on the diagnostic quality of the images. Nevertheless, our results might be useful for treatment follow-up, were the position of the lesions is previously known and the interest is on the evolution of SUV values during time.

The impact of muscular uptake in the SUV values was evaluated by using a new model for including physiological muscular uptake changes in the anthropomorphic phantoms from the previous work. Our model was based on the tracer-stealing phenomenon (Lindholm et al., 2013), so that higher muscular uptake gives rise to lower uptake in other tissues and lesions. This work tries to demonstrate that, as long as the injected doses are maintained, FDG distribution constitutes a relative mechanism. Physiological muscular uptake values were obtained from patients remitted to our center and phantoms for different muscular uptakes were generated. The variability in SUV

quantification was assessed as deviations from the mean value (in %), obtained by using SUV_{max}, SUV_{50} and SUV_{mean}, and different tumor sizes (9mm, 21mm and 31mm). The variability estimations were 17-22% in SUV_{max}, 10-19% in SUV_{50} and 8-10% in SUV_{mean} (intervals are related to the three lung lesions). We observed that the variability in tumor quantification was mainly affected by muscular uptake variations for tumor sizes of 21mm and 31mm, while statistical noise is the dominant source of variation for tumors as small as 9mm. The latter statement is also true for low injected activities, but the variability is strongly affected by statistical noise when the injected activity is below 222MBq. Our findings revealed that the SUV variability could be dominated by muscular uptake changes between relaxed patients in certain circumstances. In particular, our results showed that muscular uptake has to be taken into account as a source of uncertainty, significantly higher than the statistical noise, for large tumors (>2cm) and commonly injected activity values (>222MBq). Instead, the impact of muscular uptake is much lower when considering small tumors (<2cm) or lower injected activities (below 222MBq), where statistical noise is still the main contribution to the variability. The main contribution of our work was to generate the first database of simulated PET studies including a realistic model of muscle uptake variations. This database was used for addressing the impact of muscular uptake on PET quantification, providing an accurate estimation of SUV variability. According to our study, in a common PET scan, the estimation of SUV is affected by variability values of at least 8-10%. It is convenient to evaluate the variability related to muscular uptake changes in the context of previously reported uncertainties associated to SUV measurements. First, it has to be mentioned that the PET response criteria in solid tumors (PERCIST) classification system assumes a biologic change with SUV_{peak} about 30% (de Langen et al., 2008). Furthermore, a recent work (de Langen et al., 2012) determined the repeatability of different SUV measurements using previously published data, providing variability values in SUV_{mean} estimations about 20%, which are according to earlier reported values (Hoekstra et al., 2002). Therefore, we can conclude that muscular uptake variations between relaxed patients represent a significant uncertainty source for tumor quantification values in PET studies. Nevertheless, the simple model used to propagate the effect of the muscular variations limits our work's scope, and further assessment of the current effect needs to be done using more realistic approaches.

Finally, we developed and tested a novel software-based correction method that allows us to correct the effects of bladder accumulation on ^{18}F-based radiotracers, and that is potentially applicable to other situations. A modified version of the anthropomorphic XCAT2 phantom was obtained by including typical ^{18}F-FCH distribution, uptake variations for the bladder and prostatic lesions. A hot spot (24 ml) was added to the prostatic left lobe in order to simulate a primary prostate tumour or local recurrence. The phantoms were generated with different combinations of prostate, tumour and bladder activities. Different bladder volumes were also simulated. Our results revealed that the measured SUV values could be biased as much as 41.3% for SUV_{max} and 22.2% for SUV_{mean} when the bladder SUV varies on a range from 1.01 g/l to 18.19 g/l, with strong dependence on bladder/lesion ratio. These results reveal that the quantification on the prostatic area is very sensitive to variations on bladder accumulation, which is dependent on physiological factors, suggesting that uncorrected ^{18}F-FCH might not be an appropriate radiotracer for quantification of tumours in this area, with ^{11}C-labelled choline analogues providing a more reliable solution. The prevention of this

effect with bladder voiding, or the usage of a proper correction methods is mandatory. We proposed a correction method based on the hypothesis that spill-in counts from the bladder could be corrected with appropriate modification of the reconstruction process. The bladder is segmented from the conventional reconstructed PET image using a manually drawn ROI. After the segmentation, the bladder is analytically projected with the same projector that is used for the iterative reconstruction, generating new analytical sinograms of the bladder only. Following segmentation and forward projection, the reconstruction of the original sinograms is performed again, with the bladder sinograms as a physiological background term for the reconstruction. The process is mathematically the same as used for standard scatter and random coincidences corrections. This new method was applied to all the simulated images and the result is an image without the bladder contribution. We compared the SUV_{max} and SUV_{mean} quantification values before and after the correction. After the correction, the images provided higher accuracy and repeatability of both SUV_{max} and SUV_{mean} values, with good repeatability and in good agreement with simulated SUV values and quantified values without bladder uptake respectively. The usage of the method makes possible a reliable use of SUV on prostatic lesions when injecting ^{18}F-FCH, at least from a reconstruction point of view. More experiments are needed to ensure the applicability of the proposed method to patient studies and modifications of the methodoly might be necessary when applying it to the clinic, particularly related with the segmentation of the bladder that can be hindered by the physiology of clinical PET studies. These and other factors affecting the segmentation such as influence of patient movement and bladder volume variations are out of the scope of this work but subject of future investigations.

In summary, we have developed a methodology that allowed us to obtain simulated whole-body studies comparable to the ones obtained in our scanner. This methodology, combined with novel anthropomorphic patient databases, allowed us to evaluate the impact of different effects over the SUV values. We chose and evaluated four different effects, and proposed corrections and recommendations for each of them, allowing a more comprehensible and precise quantification of PET images. The developed methodology could be used for evaluating other effects remaining to be studied.

14

Conclusions

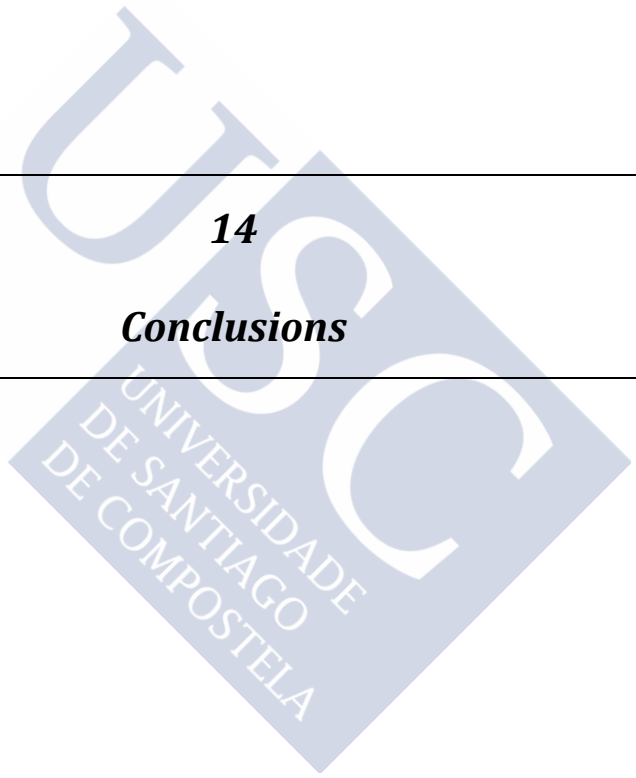

USC
UNIVERSIDADE
DE SANTIAGO
DE COMPOSTELA

14 CONCLUSIONS

During this thesis, different factors affecting SUV were evaluated, resulting on correction methods and different recommendations for improving the accuracy of PET quantification methods:

a) Different methods for estimating the extravasated dose in FDG-PET studies were developed, extensively validated by using Monte Carlo simulations, and then applied to patient studies. Our findings revealed that paravenous injection is relatively frequent effect (18%), with a small fraction of the patients presenting considerable PVI doses ranging from 1% to a maximum of 22% of the injected dose. We developed and validated a fast and easy manual method based on predefined volumetric ROIs and background subtraction for estimating the effectively administered FDG dose and then correct SUV quantification. Applying this correction, the SUV bias due to the PVI effect can be reduced. The simplicity of the proposed method suggests that its clinical application would be feasible, so that those FDG-PET studies with remarkable extravasated doses can be included in quantification protocols.

b) Regarding noise in low dose PET, we carried out an evaluation study of the accuracy and repeatability of SUV estimations obtained from FDG-PET studies in patients with solitary pulmonary nodules. Our findings showed that SUV_{50} provides the better performance for accurately estimating tumour SUV values, while SUV_{mean} provides the best results in terms of repeatability

c) For studying the impact of muscular uptake variations, we generated a new database of simulated PET studies by using an anthropomorphic phantom of patients with solitary pulmonary nodules and a realistic model of muscle uptake variations. Our findings demonstrated that muscular uptake variations between relaxed patients should be considered as a significant uncertainty source of tumor quantification values in PET studies.

d) Finally, the impact of the bladder uptake on prostate tumours quantification was evaluated using MC simulations. Our results showed that measured SUV can be biased as much as 40% when bladder/tumour ratios are high, pointing to the need for developing a correction methodology. A method based on the introduction of prior information about bladder on the reconstruction was proposed and tested, showing improvements both on visual detectability and quantification. Applying the proposed correction method, reliable SUVs can be obtained from ^{18}F-FCH images.

USC
UNIVERSIDADE
DE SANTIAGO
DE COMPOSTELA

References

Baghaei , H., Wong, W., Hongdi, L. & Uribe, J. (2003). Evaluation of the effect of filter apodization for volume PET imaging using the 3-D RP algorithm. *IEEE Trans Nucl Sci, 50*(1), 3-8.

Abushab, K. (2013). *PhD Thesis: Simulation and image reconstruction of clinical TOF-PET scanners.* Madrid, Spain: Universidad Complutense de Madrid.

Adams, M., Turkington, T. W. & Wong, T. (2010). A Systematic Review of the Factors Affecting Accuracy of SUV Measurements. *AJR Am J Roentgenol, 195*(2), 310-320.

Aguiar, P. (2010). *Quantification in Positron Emission Tomography: Reconstruction, standarization and processing methods.* LAP LAMBERT Academic Publishing.

Akamatsu, G., Ikari, Y., Nishida, H., Nishio, T., Ohnishi, A., Maebatake, A. & Senda, M. (2015). Influence of Statistical Fluctuation on Reproducibility and Accuracy of SUVmax and SUVpeak: A Phantom Study. *J Nucl Med Technol, 43*(3), 222-6.

Alessio, A., Sauer, K. & Kinahan, P. (2006). Analytical reconstruction of deconvolved Fourier rebinned PET sinograms. *Phys Med Biol, 51*(1), 77-93.

Alkhawaldeh, K. & Alavi, A. (2008). Quantitative assessment of FDG uptake in brown fat using standardized uptake value and dual-time-point scanning. *Clin Nucl Med, 33*(10), 663-667.

Anderson, C. (1933). The Positive Electron. *Phys Rev, 43*(6), 491–494.

Andrea, P. (1991). Monte Carlo techniques in medical radiation physics. *Phys Med Biol, 36*(7), 861-920.

Anger, H. (1958). Scintillation camera. *Rev Sci Instrum, 29*(1), 27-33.

Aspinall, M. & Hamermesh, R. (2007). Realizing the promise of personalized medicine. *Harv Bus Rev, 85*(1), 108-117.

Badawi, R. (1998). *PhD Thesis: Aspects of optimisation and qualification in 3D positron emission tomography.* UK: Kings College London.

Bading, J. & Shields, A. (2008). Imaging of cell proliferation: status and prospects. *J Nucl Med, 49*(Suppl 2), 64S-80S.

Bailey, D. (1998). Transmission scanning in emission tomography. *Eur J Nucl Med Mol Imaging, 25*(7), 774-87.

Bailey, D. & Meickle, S. (1994). A convolution-subtraction scatter correction method for 3D PET. *Phys Med Biol, 39*, 411-24.

Bailey, D., Townsend, D., Valk, P. & Maisey, M. (2005). *Positron Emission Tomography: Basic Sciences.* UK: Springer.

Barret , O., Clark , J., Ansorge , R. & Fryer, T. (2005). Monte Carlo simulation and scatter correction of the GE advance PET scanner with SimSET and Geant4. *Phys Med Biol, 50(20):4823-40*.

Basu, S., Zaidi, H., Holm, S. & Alavi, A. (2011). Quantitative techniques in PET-CT imaging. *Curr Med Imaging Rev, 7*(3), 216-233.

Ben-Haim, S., & Ell, P. (2009). 18F-FDG PET and PET/CT in the Evaluation of Cancer Treatment Response. *J Nucl Med, 50*(1), 88-99.

Berger, A. (2002). Magnetic resonance imaging. How does it work? *BMJ, 324*(7328), 35.

Beyer, T., Czernin, J. & Freudenberg, L. (2011). Variations in clinical PET/CT operations: results of an international survey of active PET/CT users. *J Nucl Med, 52*(2), 303-310.

Beyer, T., Schwenzer, N., Bisdas, S., Claussen, C. & Pichler, B. (2010). MR/PET – Hybrid Imaging for the Next Decade. *MAGNETON Flash, 3*(2), 19-29.

Boellaard, R. (2009). Standards for PET image acquisition and quantitative data analysis. *J Nucl Med, 50* (Suppl 1), 11S-20S.

Boellaard, R. (2011). Needs for standardization of 18F-FDG PET/CT for treatment response assessment. *J Nucl Med, 52* (Suppl 2), 93-100.

Boellaard, R., Krak, N., Hoekstra, O. & Lammertsma, A. (2004). Effects of noise, image resolution, and ROI definition on the accuracy of standard uptake values: a simulation study. *J Nucl Med, 45*(9), 1519-27.

Boellaard, R., Oyen , W., Hoekstra, C., Hoekstra, O., Visser, E., Willemsen, A. & Pruim J. (2008). The Netherlands protocol for standardisation and quantification of FDG whole body PET studies in multi-centre trials. *Eur J Nucl Med Mol Imaging, 35*(12), 2320-33.

Brasse, D., Kinahan, P., Lartizien, C., Comtat, C., Casey, M. & Michael, C. (2005). Correction methods for random coincidences in fully 3D whole-body PET: impact on data and image quality. *J Nucl Med, 46*(5), 859-67.

Brendle, C., Kupferschläger, J., Nikolaou, K., la Fougère, C., Gatidis, S. & Pfannenberg, C. (2015). Is the standard uptake value (SUV) appropriate for quantification in clinical PET imaging? - Variability induced by different SUV measurements and varying reconstruction methods. *Eur J Radiol, 84*(1), 158-162.

Brenner, D. & Hall, E. (2007). Computed tomography – an increasing source of radiation exposure. *N Engl J Med, 357*(2), 2277–84.

Brix, G., Doll, J., Bellemann, M., Trojan, H., Haberkorn, U., Schmidlin, P. & Ostertag, H. (1997). Use of scanner characteristics in iterative image reconstruction for high-resolution positron emission tomography studies of small animals. *Eur J Nucl Med Mol Ima, 24*(7), 779–86.

Brownell GL. (15 de October de 1999). A History of Positron Imaging. *Celebration of the 50th year of services of GL Brownell.*

Brownell, GL., Burnham, C.A., Hoop, B. Jr. & Bohning, D.E. (1971). *Quantitative Dynamic Studies Using Short-Lived Radioisotopes and Positron Detection.* International Atomic Energy Agency (IAEA): IAEA. Bruyant, P. (2002). Analytic and Iterative Reconstruction Algorithms in SPECT. *J Nucl Med, 43*(10), 1343-1358.

Budinger, T. (1998). PET instrumentation: what are the limits? *Semin Nucl Med, 28*(3), 247-67.

Buvat, I. (2007). Quantification in emission tomography: Challenges, solutions, and performance. *Nucl Instrum Meth A, 571*(2), 10-13.

Buvat, I. & Castiglioni, I. (2002). Monte Carlo simulations in SPET and PET. *Q J Nucl Med, 46*(1), 48-61.

Buvat, I., Orlhac, F. & Soussan, M. (2015). Tumour Texture Analysis in PET: Where Do We Stand? *J Nucl Med, 56*(11), 1642-1644.

Castiglioni, I., Cremonesi, O., Gilardi, M., Bettinardi, V., Rizzo, G., Savi, A. &Fazio, F. (1999). Scatter Correction Techniques in 3D PET: A Monte Carlo Evaluation. *IEEE Trans Nucl Sci, 46*(6), 2053 - 2058.

Cherry, S., Sorenson, J. & Phelps, M. (2012). *Physics in Nuclear Medicine* (Fourth Edition ed.). Science Direct.

Cochet, A., David, S., Moodie, K., Drummond, E., Dutu, G., MacManus, M. & Hicks, R. (2014). The utility of 18 F-FDG PET/CT for suspected recurrent breast cancer: impact and prognostic stratification. *Cancer Imaging, 14*(1), 13.

Cooke, B., Evans, A., Fanthome, E., Alaire, R. & Sendyk, A. (1984). Performance figure and images from the Therascan 3128 positron emission tomograph. *IEEE Trans Nucl Sci, 31*(1), 640-644.

Daube-Witherspoon, M. & Muehllehner, G. (1987). Treatment of axial data in three-dimensional PET. *J Nucl Med, 28*(11), 1717-24.

Daube-Witherspoon, M., Karp, J., Casey, M., DiFilippo, F., Hines, H., Muehllehner, G. & Stearns, C. (2002). PET Performance Measurements Using the NEMA NU 2-2001 Standard. *J Nucl Med, 43*(10), 1398 –1409.

de Langen, A., van den Boogaart, V., Marcus, J. & Lubberink, M. (2008). Use of H215OPET and DCE-MRI to measure tumour blood flow. *Oncologist, 13*, 631–644.

de Langen, A., Vincent, A., Velasquez, L., van Tinteren, H., Boellaard , R., Shankar, L. & Hoekstra, O. (2012). Repeatability of 18F-FDG uptake measurements in tumours: a meta-analysis. *J Nucl Med, 53*, 701-708.

Defrise, M., Kinahan, P., Townsend, D., Michael, C., Sibomana, M. & Newport, D. (1997). Exact and approximate rebinning algorithms for 3D PET data. *IEEE Trans Nucl Med, 16*(2), 145-58.

Defrise, M., Townsend, D., Bailey, D., Geissbuhler, A., Michel, C. & Jones, T. (1991). A normalization technique for 3D PET data. *Phys Med Biol, 36*(7), 939-52.

DeGrado, T., Coleman, E. & Wang , S. (2001). Synthesis and Evaluation of 18F-labeled Choline as an Oncologic Tracer for Positron Emission Tomography: Initial Findings in Prostate Cancer . *Cancer Res, 61*(1), 110-117.

Dolfi, S., Chan, L. & Qiu, J. (2013). The metabolic demands of cancer cells are coupled to their size and protein synthesis rates. *Cancer Metab, 1*(1), 20.

Doot, R., Scheuermann, J., Christian, P., Karp, J. & Kinahan, P. (2010). Instrumentation factors affecting variance and bias of quantifying tracer uptake with PET/CT. *Med Phys, 37*(11), 6035-46.

Eckert, T., Tang, C., Ma, Y., Brown, N., Lin, T., Frucht, S. & Eidelberg, D. (2008). Abnormal metabolic networks in atypical parkinsonism. *Mov Disord, 23*(5), 727-733.

Eriksson, L., Townsend, D., Conti, M., Eriksson, M., Rothfuss, H., Schmand, M. & Bendriem, B. (2006). An investigation of sensitivity limits in PET scanners. *Nucl Instrum Meth A, 580*(2), 836–842.

Eubank, W. & Mankoff, D. (2004). Current and future uses of positron emission tomography in breast cancer imaging. *Semin Nucl Med*(34), 224-240.

Eubank, W., Mankoff, D., Schmiedl, U., Winter, T., Fisher, E., Olshen, A. & Eary, J. (1998). Imaging of oncologic patients: benefit of combined CT and FDG PET in the diagnosis of malignancy. *AJR Am J Roentgenol, 171*(4), 1103-1110.

Fahey, F. (2002). Data Acquisition in PET Imaging. *J Nucl Med Technol, 30*(2).

Farwell, M., Pryma, D. & Mankoff, D. (2014). PET/CT Imaging in Cancer: Current Applications and Future Directions. *Cancer, 120*(22), 3433-45.

Ferrero, A., Poon, J., Chaudhari , A., MacDonald, L. & Badawi, R. (2011). Effect of Object Size on Scatter Fraction Estimation Methods for PET—A Computer Simulation Study. *IEEE Trans Nucl Sci, 58*(1), 82-86.

Freudenberg, L., Rosenbaum-Krumme, S., Bockisch, A., Eberhardt, W. & Frilling, A. (2008). Cancer of unknown primary. *Recent Res Cancer*, 70:193-202.

Fuster, B., Esteban, O., Planes, X., Aguiar, P., Crespo, C., Falcon, C. & Ros, D. (2013). FocusDET, a new toolbox for SISCOM analysis. Evaluation of the registration accuracy using Monte Carlo simulation. *Neuroinformatics, 11*(1), 77-89.

Gambhir, S., Czernin, J., Schwimmer, J., Silverman, D., Coleman, R. & Phelps, M. (2001). A Tabulated Summary of the FDG PET Literature. *J Nucl Med, 42*(5), 1S-15S.

Geramifar, P., Zafarghandi, M., Ghafarian, P., Rahmim, A. & Ay, M. (2013). Respiratory-induced errors in tumour quantification and delineation in CT attenuation-corrected PET images: effects of tumour size, tumour location, and respiratory trace: a simulation study using the 4D XCAT phantom. *Mol Imaging Biol, 15*(3), 655-65.

Graham, M., Badawi, R. & Wahl, R. (2011). Variations in PET/CT methodology for oncologic imaging at U.S. academic medical centers: an imaging response assessment team survey. *J Nucl Med, 52*(2), 311-7.

Hall, N., Zhang, J., Reid, R., Hurley, D. & Knopp, M. (2006). Impact of FDG extravasation on SUV measurements in clinical PET/CT. Should we routinely scan the injection site? *J Nucl Med, 47*(Suppl 1), 115P.

Hangiandreou, N. (2003). Physics Tutorial for Residents: Topics in US: B-mode US: Basic Concepts and New Technology – Hangiandreou. *Riadographics, 23*(4), 1019–1033.

Harrison, R. (2010). Monte Carlo Simulation Of Emission Tomography And Other Medical Imaging Techniques. *AIP Conf Prod, 5*(1204), 162-132.

Harrison, R. (2017). *SimSET webpage*. Retrieved from University of Washington: (http://depts. washington. edu/~ simset/html/simset_main. html)

Harrison, R., Kaplan, M., Vannoy, S. & Lewellen, T. (1999). Positron range and coincidence non-collinearity in SimSET. *Nuclear Science Symposium, Conference Record. IEEE, 3*(1).

Hebert, T. & Lealhy, R. (1989). A generalized EM algorithm for 3-D Bayesian reconstruction from Poisson data using Gibbs priors. *IEEE Trans Med Ima, 8*(2), 194-202.

Herholz, K., Salmon, E., Perani, D., Baron, J., Holthoff, V., Frölich, L., . . . Heiss, W. (2002). Discrimination between Alzheimer dementia and controls by automated analysis of multicenter FDG PET. *Neuroimage, 17*(1), 302-316.

Herman, G. (2009). *Fundamentals of computerized tomography: Image reconstruction from projection* (2nd edition ed.). Springer.

Hess, S., Blomberg, B., Rakheja, R., Friedman, K., Kwee, T., Høilund-Carlsen, P., & Alivi, A. (2014). A brief overview of novel approaches to FDG PET imaging and quantification. *Clin Transl Imaging, 2*(3), 187-198.

Hess, S., Blomberg, B., Zhu, H., Høilund-Carlsen, P. & Alavi, A. (2014). The pivotal role of FDG-PET/CT in modern medicine. *Acad Radiol, 21*(2), 232–249.

Hillner, B., Siegel, B., Hanna, L., Shields, A., Duan, F., Gareen, I. & Coleman, R. (2012). Impact of 18F-FDG PET used after initial treatment of cancer: comparison of the National Oncologic PET Registry 2006 and 2009 cohorts. *J Nucl Med, 53*(5), 831-7.

Hillner, B., Siegel, B., Liu, D., Shields, A., Gareen, I., Hanna, L. & Coleman, R. (2008). Impact of positron emission tomography/computed tomography and positron emission tomography (PET) alone on expected management of patients with cancer: initial results from the National Oncologic PET Registry. *J Clin Oncol, 26*(13), 2155-61.

Hoekstra, C., Hoekstra, O., Stroobants, S., Vansteenkiste, J., Nuyts, J., Smit, E. & Lammertsma, A. (2002). Methods to monitor response to chemotherapy in non-small cell lung cancer with 18F-FDG PET. *J Nucl Med, 43*(10), 1304-9.

Hoh, C., Seltzer, M., Franklin, J., deKernion, J., Phelps, M. & Belldegrun, A. (1998). Positron emission tomography in urological oncology. *J Urol, 159*(2), 347-356.

Hudson, H. & Larkin, R. (1994). Accelerated image reconstruction using ordered subsets of projection data. *IEEE Trans Med Ima, 13*(4), 601–609.

Humm, J. L., Rosenfield, A. & Del Guerra, A. (2003). From PET detectors to PET scanners. *Eur J Nucl Med Mol I, 30*(11), 1574-97.

Hutton, B. (2011). Recent advances in iterative reconstruction for clinical SPECT/PET and CT. *Acta Oncol, 50*(6), 851-58.

Inoue, T., Kim, E., Wong, F., Yang, D., Bassa , P., Wong, W. &Podoloff, D. (1996). Comparison of fluorine-18-fluorodeoxyglucose and carbon-11-methionine PET in detection of malignant tumours. *J Nucl Med, 37*(9), 1472-6.

International Atomic Energy Agency. (2009). *IAEA Human Health Series N1: Quality Assurance for PET and PET/CT systems.* Vienna: IAEA Publishing.

Jackson, R., Schlarman, T., Hubble, W. & Osman, M. (2006). Prevalence and Patterns of Physiologic Muscle Uptake Detected with Whole-Body 18F-FDG PET. *J Nucl Med Technol, 34*(4), 29-33.

Jakoby , B., Bercier , Y., Conti, M., Casey, M., Bendriem, B. & Townsend , D. (2011). Physical and clinical performance of the mCT time-of-flight PET/CT scanner. *Phys Med Biol, 56*(8), 2375–2389.

Jan, S., Benoit, D., Becheva, E., Carlier, T., Cassol, F., Descourt, P. & Buvat, I. (2011). GATE V6: a major enhancement of the GATE simulation platform enabling modelling of CT and radiotherapy. *Phys Med Biol, 56*(4), 881-901.

Jaskowiak, C., Bianco, J., Perlman, S. & Fine, J. (2005). Influence of reconstruction iterations on 18F-FDG PET/CT standardized uptake values. *J Nucl Med, 46*(3), 424-8.

Jaszczak, R. (2006). The early years of single photon emission computed tomography (SPECT): an anthology of selected reminiscences. *Phys Med Biol, 51*(13), R99–R115.

Jones, T. & Rabiner, E. (2012). The development, past achievements, and future directions of brain PET. *J Cereb Blood Flow Metab, 32*(7), 1426-54.

Kadrmas, D., Casey, M., Conti, M., Jakoby, B., Lois, C. & Townsend, D. (2009). Impact of Time-of-Flight on PET Tumour Detection. *J Nucl Med, 50*(8), 1315-23.

Kaira, K., Oriuchi, N., Shimizu, K., Tominaga, H., Yanagitani, N., Sunaga, N. & Endo, K. (2009). 18F-FMT Uptake Seen Within Primary Cancer on PET Helps Predict Outcome of Non–Small Cell Lung Cancer. *J Nucl Med, 50*(11), 1770–1776.

Kassem, H., El Shiekh, F., Wafaie, A., Abdelfattah, S., Farghaly, H. & Afifi, L. (2013). Presurgical evaluation of refractory temporal lobe epilepsy: Comparison of MR imaging, PET and ictal SPECT in localization of the epileptogenic substrate. *Egy J Radiol Nucl Med, 44*(3), 641–649.

Kelloff, G., Hoffman, J., Johnson, B., Scher, H., Siegel, B., Cheng, E. & Sullivan, D. (2005). Progress and promise of FDG-PET imaging for cancer patient management and oncologic drug development. *Clin Cancer Res, 11*(8), 2785-808.

Kim, Y., Lee, D., Lee, S., Chung, C., Chung, J. & Lee, M. (2002). (18)F-FDG PET in localization of frontal lobe epilepsy: comparison of visual and SPM analysis. *J Nucl Med, 43*(9), 1167-74.

Kinahan, P. & Fletcher, J. (2010). PET/CT Standardized Uptake Values (SUVs) in Clinical Practice and Assessing Response to Therapy. *Semin Ultrasound CT MR, 31*(6), 496-505.

Kinahan, P., Hasegawa, B. & Beyer, T. (2003). Xray-based attenuation correction for positron emission tomography/computed tomography scanners. *Semin Nucl Med, 33*(3), 166-79.

Kiyohara, S., Nagamachi, S., Wakamatsu, H., Nishii, R., Fujita, S. & Futami, S. (2010). Usefulness of metabolic volume and total lesion glycolysis for predicting therapeutic response in cancer therapy by 18 F-FDG PET/CT. *Kaku Igaku, 47*(4), 453–461.

Kuhl, D. & Edwards, R. (1963). Image separation radioisotope scanning. *Radiology, 80*, 653–62.

Kumar, S., Rajshekher, G. & Prabhakar, S. (2005). Positron emission tomography in neurological diseases. *Neurol India, 53*(2), 149-155.

Lambin, P., Rios-Velazquez, E., Leijenaar, R., Carvalho, S., van Stiphout, R., Granton, P. & Aerts, H. (2012). Radiomics: extracting more information from medical images using advanced feature analysis. *Eur J Cancer, 48*(4), 441-446.

Lecoq, P. (2016). Development of new scintillators for medical applications. *Nucl Instrum Meth A, 809*, 130–139.

Lee, K., Hristov, D., Casey, M. & Rajaram, R. (2013). MO-D-141-02: Evaluation of Optimal Gating Respiratory Motion Management Technique On PET Quantification. *Med Phys, 40*(6), 399.

Lee, N., Nehmeh, S., Schoder, H., Fury, M., Chan, K., Ling, C. & Humm, J. (2009). Prospective trial incorporatin pre/mid-treatment 18F-misonidazole positron emission tomography for head-an-neck cancer patients udergoing concurrent chemoradiotherapy. *Int J Radiat Oncol Biol Phys, 75*(1), 101-108.

Lee, S., Lee, D., Yeo, J., Kim, Y., Jang, M., Kim, S. & Chung, C. (2002). FDG-PET Images Quantified by Probabilistic Atlas of Brain and Surgical Prognosis of Temporal Lobe Epilepsy. *Epilepsia, 43*(9), 1032-1038.

Levin, C. (2008). New Imaging Technologies to Enhance the Molecular Sensitivity of Positron Emission Tomography. *Proceedings of the IEEE, 96*(3), 439 - 467.

Levin, C., Dahlbom, M. & Hoffman, E. (1995). A Monte Carlo correction for the effect of Compton scattering in 3-D PET brain imaging. *IEEE Trans Nucl Sci, 42*(4), 1181-85.

Lewitt, R., Muehllehner, G. & Karp, J. (1994). Three-dimensional reconstruction for PET by multi-slice rebinning and axial image filtering. *Phys Med Biol, 39*(3), 321-39.

Lin, C., Itti, H., Haioun, C., Petegnief, Y., Luciani, A., Dupuis, J. & Meignan, M. (2007). Early 18F-FDG PET for prediction of prognosis in patients with diffuse large B-cell lymphoma: SUV-based assessment versus visual analysis. *J Nucl Med, 48*(10), 1626-32.

Lindholm, H., Brolin, F., Jonsson, C. & Jacobsson, H. (2013). The relation between the blood glucose level and the FDG uptake of tissues at normal PET examinations. *EJNMMI Res, 3*(50).

Lindholm, H., Johansson, O., Jonsson, C. & Jacobsson, H. (2012). The distribution of FDG at PET examinations constitutes a relative mechanism: significant effects at activity quantification in patients with a high muscular uptake. *Eur J Nucl Med Mol Imaging, 39*, 1685-1690.

Lodge, M., Chaudhry, M. & Wahl, R. (2012). oise Considerations for PET Quantification Using Maximum and Peak Standardized Uptake Value. *J Nucl Med, 53*(7), 1041–1047.

Lois, C., Jakoby, B., Long, M., Hubner, K., Barker, D., Casey, M. & Townsend, D. (2009). An Assessment of the Impact of Incorporating Time-of-Flight Information into Clinical PET/CT Imaging . *J Nucl Med, 50*(8), 1315-23.

Lu, F. & Yuan, Z. (2015). PET/SPECT molecular imaging in clinical neuroscience: recent advances in the investigation of CNS diseases. *Quant Imaging Med Surg, 5*(3), 433-447.

Lusic, H., & Grinstaff, M. (2013). X-Ray Computed Tomography Contrast Agents. *Chem Rev, 113*(3).

Manbachi, A. & Cobbold, R. (2011). Development and Application of Piezoelectric Materials for Ultrasound Generation and Detection. *Ultrasound, 19*(4), 187-194.

Mankoff, D. (2007). A definition of molecular imaging. *J Nucl Med, 48*(6), 18-21.

Martí-Climent, J., Prieto, E., Domínguez-Prado, I., García-Velloso, M., Rodríguez-Fraile, M., Arbizu, J. & Richter, J. (2013). Contribution of time of flight and point spread function modeling to the performance characteristics of the PET/CT Biograph mCT scanner. *Rev Esp Med Nucl Mol Ima, 32*(1).

Mease, R., Foss, C. & Pomper, M. (2013). PET imaging in prostate cancer: focus on prostate-specific membrane antigen. *Curr Top Med Chem, 13*(8), 951-62.

Minn, H., Leskinen-Kallio, S. & Lindholm, P. (1993). [18F]fluorodeoxyglucose uptake in tumours: kinetic vs. steady-state methods with reference to plasma insulin. *J Comput Assist Tomogr, 17*(1), 115-123.

Miyashita, K., Takahashi, N., Oka, T., Asakawa, S., Lee, J., Shizukuishi, K. & Inoue, T. (2007). SUV correction for injection errors in FDG-PET examination. *Annals of Nuclear Medicine, 21*(10), 607-613.

Moses, W. (2011). Fundamental Limits of Spatial Resolution in PET. *Nucl Instrum Methods Phys Res A, Supp1*(648), S236–S240.

Muellehner, G. (1971). A tomographic scintillation camera. *Phys Med Biol*(16), 87–96.

National Electrical Manufacturers Association. (2007). *NEMA Standards Publication NU 2–2007, Performance measurements of positron emission tomographs.* Rosslyn, VA.

Nichols, T., Qi, J., Asma, E. & Leahy, R. (2002). Spatiotemporal Reconstruction of List-Mode PET Data. *IEEE Trans Mmed Ima, 21*(4).

Ollinger, J. & Johns, G. (1993). Model-based scatter correction for fully 3D PET. *IEEE Medical Imaging Conf. Record, 2*, 1264–68.

Osman, M., Muzaffar, R., Altinyay, M., & Teymouri , C. (2011). FDG Dose Extravasations in PET/CT: Frequency and Impact on SUV Measurements. *Front Oncol*, 1:41.

Paans, A., Rosenqvist, G., Holte, S., Eriksson, L., Dahlbom, M. & Bohm, C. (1989). Scatter fraction: measurement and correction. *Eur J Nucl Med Mol Ima*.

Papadimitroulas, P., Loudos, G., Le Maitre, A., Hatt, M., Tixier, F. & Efthimiou, N. (2012). Investigation of realistic PET simulations incorporating tumour patient's specificity using anthropomorphic models: creation of an oncology database. *Med Phys, 40*(11).

Phelps, M., Hoffman, E., Mullani, N. & Ter-Pogossian, M. (1975). Application of annihilation coincidence detection to transaxial reconstruction tomography. *J Nucl Med, 16*(3), 210–24.

Polycarpou, P., Marsden, P. & Tsoumpas, C. (2011). A comparative investigation of scatter correction in 3D PET . *J Phys Conf Ser, 317*(1).

Popota, F., Aguiar, P., España, S., Lois, C., Udias, J., Ros, J. &Gispert, J. (2015). 'Monte Carlo simulations versus experimental measurements in a small animal PET system. A comparison in the NEMA NU 4-2008 framework. *Phys Med Biol, 60*(1), 151-162.

Porcello, L., Zimmer, E., Shin, M., Leuzy, A., Pascoal, T., Benedet, A. & Rosa-Neto, P. (2016). Imaging Alzheimer's disease pathophysiology with PET. *Dement Neurophycol, 10*(2).

Portnow, L., Vaillancourt, D. & Okun, M. (2013). The history of cerebral PET scanning. *Neurology, 81*(14).

Quader, M., Sawmiller, C. & Sumpio, B. (2000). Radio Contrast Agents: History and Evolution.*Textbook of Angiology* (Vol. Section 7, 775-783). US. Springer

Raeside, D. (1976). Monte Carlo principles and applications. *Phys Med Biol, 21*, 181-197.

Rahim, M., Kim, S., So, H., Kim, H., Cheon, G., Lee, E. & Lee, D. (2014). Recent Trends in PET Image Interpretations Using Volumetric and Texture-based Quantification Methods in Nuclear Oncology. *Nucl Med Mol Ima, 48*(1), 1-15.

Rogers, D. (2006). Fifty years of Monte Carlo simulations for medical physics. *Phys Med Biol, 51*, 287-301.

Rousseau, C., Devillers, A., Sagan, C., Ferrer, L., Bridgi, B., Campion, L. & Campone, M. (2006). Monitoring of early response to neoadjuvant chemotherapy in stage II and III breast cancer by [18F]fluorodeoxyglucose positron emission tomography. *J Clin Oncol, 24*(34), 5366-72.

Rozsa, C. *Measuring Radiation: An Introductory Discussion.* Saint-Gobain Ceramics & Plastics, Inc.

Saha, G. (2010). *Basics of PET Imaging: Physics, Chemistry, and Regulations* (Third Edition ed.). Springer International Publishing.

Salem, R., Lewandowski, R., Atassi, B., Gordon, S., Gates, V., Barakat O, & Thurston, K. (2005). Treatment of Unresectable Hepatocellular Carcinoma with Use of 90Y Microspheres (TheraSphere): Safety, Tumour Response, and Survival. *J Vasc Interv Radiol, 16*(12), 1627–1639.

Sattarivand, M. & Caldwell, C. (2010). Comparison of Two Fixed-Size ROI Methods for Tumour Response Assessment Using FDG-PET. *Med. Phys*(37).

Scatliff , J. & Morris, P. (2014). From Röntgen to Magnetic Resonance Imaging: The History of Medical Imaging . *N C Med J, 75*(2), 111-113.

Schwartz, J., Humm, J., Gonen, M., Kalaigian, H., Schoder, H. & Larson, S. (2011). Repeatability of SUV measurements in serial PET. *Med Phys, 38*(5), 2629-38.

Seagars, W., Sturgeon, G., Mendonca, S., Grimes, J. & Tsui, B. (2010). 4D XCAT phantom for multimodality imaging research. *Med Phys, 37*(9), 4902-15.

Sharma, S. (2014). Imaging and intervention in prostate cancer: Current perspectives and future trends. *Indian J Radiol Imaging, 24*(2), 139-148.

Sher, A., Lacoeuille, F., Fosse, P., Verveuren, L., Cahouet-Vannier, A., Dabli, D., & Couturier, O. (2016). For avid glucose tumours, the SUV peak is the most reliable parameter for [18F]FDG-PET/CT quantification, regardless of acquisition time. *EJNMMI Research, 6*(1).

Shin, H., Jewells, V., Sheikh, A., An, H., Hadar, E., Ngo, L. & Lin, W. (2015). Hybrid PET/MR May Improve Diagnostic Yield of Epileptic Lesions. *Neurology, 84*(14), P6.

Silva-Rodríguez, J., Cortés, J., Pardo-Montero, J., Pérez-Fentes, D., Herranz, M., Ruibal, A. & Aguiar, P. (2015). In vivo quantification of renal function in mice using clinical gamma cameras . *Phys Med, 31*(3), 242-247.

Silverman, D., Small, G., Chang, C., Lu, C., Kung de Aburto, M. & Cheng, W. (2001). Positron emission tomography in evaluation of dementia: Regional brain metabolism and long-term outcome. *JAMA, 288*, 2120-7.

Sokoloff, L. (1977). Relation between physiological function and energy metabolism in the central nervous system. *J Neurochem, 29*, 13–26.

Soussan, M., Orlhac, F., Boubaya, M., Zelek, L., Ziol, M., Eder, V.,& Buvat, I. (2014). Relationship between tumour heterogeneity measured on FDG-PET/CT and pathological prognostic factors in invasive breast cancer. *PLoS One, 9*(4).

Spanoudaki, V. C. & Levin, C. S. (2010). Photo-Detectors for Time of Flight Positron Emission Tomography (ToF-PET). *Sensors, 10*(11), 10484–10505.

Spencer, S. (1994). The relative contributions of MRI, SPECT, and PET imaging in epilepsy. *Epilepsia, 35* (Suppl 6), 72-89.

Steiner, R. (2011). Why Should We Be Interested in Cardiac PET/CT Imaging? *RSNA Radiographics, 31*(5).

Sun, X., Niu, G., Chan, N., Shen, B. & Chen, X. (2011). Tumour hypoxia imaging. *Mol Imaging Biol, 13*(3), 399-410.

Szablewski, L. (2013). Expression of glucose transporters in cancers. *Reviews on Cancer, 1835*(2), 164-169.

Tan, L. & Ong, K. (2004). Semi-Quantitative Measurements of Normal Organs With Variable Metabolic Activity on FDG PET Imaging. *Ann Acad Med Singapore, 33*(2), 183-5.

Teymurazyan, A., Riauka, T., Jans, H. & Robinson, D. (2013). Properties of Noise in Positron Emission Tomography Images Reconstructed with Filtered-Backprojection and Row-Action Maximum Likelihood Algorithm. *J Digit Imaging, 26*, 447–456.

Teymurazyan, A., Riauka, T., Jans, H., & Robinson, D. (Jun de 2013). Properties of Noise in Positron Emission Tomography Images Reconstructed with Filtered-Backprojection and Row-Action Maximum Likelihood Algorithm. *J Digit Imaging, 26*(3), 447–456.

Thielemans, K., Tsoumpas, C., Mustafovic, S., Biesel, T., Aguiar, P., Dikaios, N. & Jacobson, M. (2012). STIR: software for tomographic image reconstruction release 2. *Phys Med Biol, 57*(4), 867-83.

Tong, S., Alession, A. & Kinahan, P. (2010). Image reconstruction for PET/CT scanners: past achievements and future challenges . *Imaging Med, 2*(5), 529-45.

Troost, E., Bussink, J., Hoffmann, A., Boerman, O., Oyen, W. & Kaanders , J. (2010). 18F-FLT PET/CT for early response monitoring and dose escalation in oropharyngeal tumours. *J Nucl Med*(51), 866-874.

Turkington, T. G. (2001). Introduction to PET Instrumentation. *J Nucl Med Technol, 29*, 4-11.

Vallabhajosula, S. (2009). *Molecular Imaging: Radiopharmaceuticals for PET and SPECT.* Berlin. Springer.

van der Veldt, A., Smit, E. F., & Lammertsma, A. (2013). Positron emission tomography as a method for measuring drug delivery to tumours in vivo: the example of [11C]docetaxel. *Front Oncol, 3*(208), 1-7.

Van Paesschen, W., Dupont, P., Sunaert, S., Goffin, K. & Van Laere, K. (Apr de 2007). The use of SPECT and PET in routine clinical practice in epilepsy. *Curr Opin Neurol, 20*(2), 194-202.

van Westreenen, H., Cobben, D., Jager, P., van Dullemen, H., Wesseling, J., Elsinga, P., & Plukker, J. (2005). Comparison of 18F-FLT PET and 18F-FDG PET in Esophageal Cancer. *J Nucl Med, 46*, 400 – 404.

Vicente, E., Herraiz, J., España, S., Herranz, E., Desco, M., Vaquero, J. & Udías, J. (2013). Improved dead-time correction for PET scanners: application to small-animal PET. *Phys Med Biol, 58*(7), 2059-72.

Villeneuve, R., Risso, R., Garnier, N., Paulmier, B. & Serrano, B. (2013). Impact of Partial Volume Effect On PET Image: Quantification Aspect. *Med. Phys*(40).

Visser, E., Boerman, O. & Oyen, W. (2010). From Silly Useless Value to Smart Uptake Value. *J Nucl Med, 51*(2), 173-175.

Visvikis, D., Hatt, M., Tixier , F., & Cheze Le Rest, C. (2012). The age of reason for FDG PET image-derived indices. *Eur J Nucl Med Mol Imaging*, 39(11):1670-2.

Wagner, H. (Apr de 2007). PET Is Alive and Well. *J Nucl Med, 48*(4), 495.

Wahl, R., Jacene, H., Kasamon, Y., & Lodge, M. (2009). From RECIST to PERCIST: Evolving considerations for PET response criteria in solid tumours. . *J Nucl Med, 50*(Suppl 1), 122S-150S.

Watson, C., Newport, D. & Casey, M. (1996). A single scatter simulation technique for scatter correction in 3D PET. En P. G. Amans (Ed.), *Three-dimensional Image Reconstruction in Radiology and Nuclear Medicine*, 255–68.

Weber, W. (2005). PET for response assessment in oncology: radiotherapy and chemotherapy. *Br J Radiol*, 42:0007-1285.

Weber, W. (2010). Monitoring tumour response to therapy with 18F-FLT PET. *J Nucl Med*(51), 1841-844.

Weber, W., Petersen, V., Schmidt , B., Tyndale-Hines, L., Link, T., Peschel, C. & Schwaiger, M. (2003). Positron emission tomography in non-small-cell lung cancer: prediction of response to chemotherapy by quantitative assessment of glucose use. *J Clin Oncol, 21*(14), 2651-7.

Werling, A., Bublitz, O., Doll, J., Adam, L., & Brix, G. (2002). Fast implementation of the single scatter simulation algorithm and its use in iterative image reconstruction of PET data. *Phys Med Biol, 47*, 2947-2960.

Willowson, K., Bailey, E. & Bailey, D. (2012). A retrospective evaluation of radiation. *Australas Phys Eng Sci Med, 35*, 49–53.

Won, H., Chang, K., Cheong, J., Kim, H., Lee, D., Han, M. & Chung, C. (1999). Comparison of MR Imaging with PET and IctalSPECT in 118 Patients with Intractable Epilepsy. *AJNR, 20*, 593-599.

Xu, X., Chao, T., & Bozkurt, A. (2000). VIP-Man: an image-based whole-body adult male model constructed from color photographs of the Visible Human Project for multi-particle Monte Carlo calculations. *Health Phys, 78*(5), 476-86.

Yanagawa, M., Tatsumi, M., Miyata, H., Morii, E., Tomiyama, N. & Watabe, T. (2012). Evaluation of response to neoadjuvant chemotherapy for esophageal cancer: PET response criteria in solid tumours versus response evaluation criteria in solid tumours. *J Nucl Med, 53*, 872-80.

Yeung, H., Grewal, R., Gonen, M., Schoder, H. & Larson, S. (2003). Patterns of 18F-FDG uptake in adipose tissue and muscle: a potential source of false-positives for PET. *J Nucl Med, 44*(4), 1789–1796.

Zaidi, H. (1999). Relevance of accurate Monte Carlo modeling in nuclear medical imaging. *Med Phys Biol, 26*(4), 574-608.

Zaidi, H., & Xu, X. (2007). Computational Anthropomorphic Models of the Human Anatomy: The Path to Realistic Monte Carlo Modeling in Radiological Sciences. *Annu Rev Biomed Eng, 9*, 471-500.

Zanzonico, P. (2008). Routine Quality Control of Clinical Nuclear Medicine Instrumentation: A Brief Review. *J Nucl Med*, *49*(7), 1114-31.

Zubal, I., Harrell, C., Smith, E., Rattner, Z., Gindi, G. & Hoffer, P. (1994). Computerized three-dimensional segmented human anatomy. *Med Phys*, *21*(2), 299-302.

USC
UNIVERSIDADE
DE SANTIAGO
DE COMPOSTELA